Biomediated synthesis of Nano Metal Oxides and Nanocomposite Metal Oxides for Photocatalytic and Antimicrobial Applications

By

Dr. Bedasa Abdisa

Mr. Eneyew Tilahun

Dr. Fedlu Kedir

A Final Research Report Submitted to Adama Science and Technology University

Adama, Ethiopia
March, 2023

Biomediated synthesis of Nano Metal Oxides and Nanocomposite Metal Oxides for Photocatalytic and Antimicrobial Applications

Abstract

Now days, water contamination caused by various sources have drawn a series attention. In addition to this, antimicrobial caused diseases have become series issue worldwide, especially for developing countries. The focus of the present study was biogenic synthesis of Co_3O_4 NPs, TiO_2/rGO, and ZnO/CuO NCs within various volume ratios in the presence of peel extract of ST, CS, and MA, respectively. It was observed that Co_3O_4 NPs were stable above 450℃, and were spherical in shape, and had the average crystalline size of, 13.5-19.45 nm, and band gap energy of 3.25- 3.37 eV for the 1:2, 1:1 and 2:1volume ratios, respectively. SEM-EDS, TEM, HRTEM and SAED confirm that the NPs were spherical in shape and crystalline. Thermal analysis of green synthesized TiO_2 based NPs confirmed that the pristine NPs were found to be stable above 500℃ having average crystalline size in the range of 7-27 nm and 13-22 nm for the CS and MA, respectively. The average crystalline size of CS and MA peel extract templated synthesized TiO_2/rGO NCs were found to be in the range of 7-15and 11-12nm, respectively. The band gap energy was calculated to be in the range of 3.17-3.29 eV and 3.10-3.38 eV for the CS and MA mediated synthesized TiO_2 NPs, respectively. While E_g of CS and MA peel extract templated formed TiO_2/rGO NCs were found in the range of 2.85-3.11 eV and 3.07-3.11 eV, respectively. SEM analysis proved that TiO_2 NPs and TiO_2/rGO NCs were spherical in shape. TEM, HRTEM, and SAED confirmed that the NPs and NCs nanocatalysts were spherical and crystalline. The average crystalline size of ZnO NPs were found to be within 24.9-28.2 nm for the 1:1, 1:2, and 1:3, respectively and 17.0 nm for CuO NPs. The average crystalline sizes of ZnO/CuO NCs were found within the range of 22.6-22.9 nm for 10%, 15%, 20% and 25%, respectively. SEM and TEM analysis confirmed that ZnO NPs, CuO NPs, and ZnO/CuO NCs were spherical shape. E_g of ZnO NPs were 3.24-.24 eV for the 1:1, 1:2, and 1:3, respectively. E_g of CuO NPs were estimated to be 1.7 eV and that of ZnO/CuO NCs decreased from 3.24 to 3.05eV. 94.28%, 94.25%, and 90% of MB degradation were achieved in the presence of TiO_2/rGO-1.5c, TiO_2/rGO-1.5m, and ZnO/CuO (20%) catalyst, respectively. ZnO/CuO (20%) NCs and Co_3O_4 (1:2) NPs showed 22 and 27 mm ZOI, respectively. ZnO/CuO (20%) and Co_3O_4 (1:2 and 1:1) NPs showed 0.40 and 0.00 MGI against *Alternaria Solani*, respectively.

Keywords: Metal oxide nanoparticles, nanocomposites, peel extract, biosynthesis, photocatalysis and antimicrobial.

Acknowledgments

All investigators of the project emphatically acknowledge Adama Science and Technology University (ASTU) for support this project through ASTU's 14 cycle research grant. The investigators also extend their thanks to department of applied chemistry and department of materials science and engineering at ASTU for providing facilities such as TGA/DTA, XRD, UV-DRS and photoreactor. Department of chemistry at Bahir Dar University is also thanked by for allowing FT-IR analysis. Moreover, the investigators thank the department of applied biology, ASTU, for testing the antibacterial activity of the synthesized NPs and NCs. The investigators also extend their hearty thanks to the Ethiopian agricultural research center, Awash Melkasa Brach, for their willingness for carrying out the antifungal activity tests. In addition to this, the authors highly acknowledge Dr. C. R. Ravikumar, Research Centre, Department of Science, East-West Institute of Technology, Bangalore 560091, India, for SEM- EDS, TEM, HRTEM and SAED characterizations.

Table of Content

Contents **Page**

List of Figures

List of Tables

List of Symbols and Acronyms

DTA	Differential thermal analyzer
E_g	Band gap energy
FTIR	Fourier transformation infrared spectroscopy
FWHM	Full width at half maximum
JCPDS	Joint committee on powder diffraction standards
K	Scherrer's constant
MA	*Musa acuminata*
NCs	Nanocomposites
rGO	Reduced graphene oxide
SAED	Surface area electron diffraction
HRTEM	High resolution transmission electron microscopy
TEM	Transmission electron microscopy
CS	*Citrus sinensis*
SEM	Scanning electron microscope
ST	*Solanum tuberosum*
θ	Diffraction angle
TGA	Thermal gravimetric analysis
UV-Vis	Ultraviolet spectrophotometer spectroscopy
XRD	X- ray diffraction
λ_{max}	Wavelength at maximum absorbance
B	Full width at half maximum intensity

1. Introduction

The natural environment has been exposed to various natural and artificial hazardous problems due to overpopulation growth, advancements in urbanization, accumulation of agricultural fruit and vegetable wastes and industrial wastes including organic dyes, pesticides, inorganic contaminants and detergents, heavy and toxic metal ions, the decomposition of toxic and poisonous gases and chemical species produced from various chemical industries. Among these, the discharge of various types and nature of dye effluents from various chemical industries and sources such as dye stuffs, textiles, paint and varnishes, inks, plastics, pulp and paper, food, rubber and cosmetics to the environment is a prime cause of concern nowadays worldwide. When those pollutants and dyes are discarded into the water bodies without adequate treatment, they could results in changing the color of water bodies, promoting significant changes in the hydrological cycle; thus could lead to severe diseases and even to the death of human beings. Thus, the degradation and removal of those organic dyes from water bodies is of great environmental and industrial importance. A number of miscellaneous methods such as ion exchange, reverse osmosis, membrane filtration, adsorption processes, chlorination, chemical precipitation and electrochemical methods, sedimentation-flocculation and coagulation as well molecular sieving have been widely explored for water treatment containing wastes but those protocols cannot completely degrade the organic pollutants and also results in the formation of secondary pollutants (Fathima *et al*. 2008; Soni *et al*. 2021).

Recent studies have shown that advanced oxidation process (AOPs) using heterogeneous green mediated synthesized catalyst in the presence of visible light irradiation are the best alternative techniques for the decontamination of wastewater as compared to conventional methods due to low-cost and high stability, nontoxicity, absence of resistance to mass transfer and secondary pollution, operation under ambient conditions, high surface area to volume ratio, energy efficient, environmentally safe and more importantly the potential for decomposing the recalcitrant organic pollutants at short reaction time into less and zero harmful forms. One of the AOPs is heterogeneous photocatalysis using semiconducting metal oxides nanoparticles especially prepared via green methods. In this process, the electron-hole pairs degrade the dye molecules present within the water into less or zero harmful components(Fan and Fang 2020; Luque-Morales *et al*. 2021).

Currently, various semiconductor-based nanomaterials have attracted a significant interest for the purification and treatment of wastewater via the method of AOP (photocatalysis) technique. Among these, nano sized metal oxide photocatalysts such as TiO_2, CuO, Co_3O_4, ZnO, ZnS, CdS, Fe_2O_3, MgO, Mn_2O_3,

ZrO_2, V_2O_5, Nb_2O_5, WO_3, and many others have been investigated and used in the process of wastewater decontamination (Sivachidambaram et al., 2017a). Particularly, wastewater decontamination using high surface area semiconductor NCs photocatalysts prepared via numerous techniques has shown improved potential. Previously, it has been reported that TiO_2 and ZnO NPs has been abundantly used and selected as the most reliable candidate as an environmentally clean and pristine photocatalyst due to its desired chemical properties, favorable optical effects, chemically balanced and photochemical stability, dielectric properties, biological and chemical inertness, high redox potential and good photocatalytic efficiency and non-toxicity. In order to improve and enhance the photocatalytic activity of TiO_2 and ZnO NPs, several approaches have been revised such as metallic and non-metallic doping, conductive polymer doping, dye sensitization and formation of composite by using various synthesis methods. Among these adapted techniques of preventing the electron-hole recombination rate, TiO_2-based composite nano-photocatalysts are the most reliable and cost-effective candidates. Previously, TiO_2 based NCs materials such as TiO_2/ZnO, g/TiO_2, $Bi_4Ti_3O_{12}$/$Bi_2Ti_2O_7$ and Au/TiO_2 was synthesized via various chemical synthetic protocols for photocatalytic applications (Prajapati & Mondal, 2021). Various physico-chemical synthesis protocols for ZnO and TiO_2-based NCs including the green approach were also reported. Among these techniques, the green synthesis approach is ecofriendly, inexpensive, and easily manageable as it involves the use of green alternative starting materials (extract of plants, bacteria, algae, and fungi) as a template and green solvents such as ethanol and distilled water, and non-toxic and less toxic precursors/salts. Moreover, using of peel extract as a capping and reducing agent for the synthesis of various types of metal oxide NPs and NCs could be the most preferable technique; since this way provides more advantages such as in one way the environment is cleaned while using the peels which pollutes the environment once discarded to the environment as a waste and in the other side, those peels could be accessed from the environment with zero cost (Nainani and Thakur 2016; Saranya *et al*. 2018).

In addition to water pollution, nowadays, one of the global health concerns is the increasing of antimicrobial resistance caused by many microorganisms against drugs, because some pathogens which were curable in past now are becoming untreatable such as Methicillin-resistant *staphylococcus Aureus*. To address this battle and to overcome frightening situation of microbial resistance to antibiotics, using metal oxide NPs synthesized via easily achievable techniques as antimicrobial agent are becoming the best alternative options worldwide. Cobalt oxide and ZnO NPs are one of the inorganic nanomaterials which can be used for such antimicrobial activities because of its interesting various physico-chemical properties. A rapid increment in the development of new antimicrobial inorganic and organic materials has been observed as consequence of the spread of antibiotic resistant infection disease, which has become a major issue in the current health care. It has been reported that, synthesis of various types of

NPs and NCs via various chemical and green methods for the desired applications were intensified (Kiflom Gebremedhn *et al*. 2019). Currently, the biomediated synthesis protocols of NPs and NCs using various types of green capping and reducing agents such as various parts of green plants, waste of fruits and vegetables were reported. However, synthesis of various types of NPs and NCs using peel waste extract of vegetables and fruits as capping and reducing agent were not exploited. Hence, instead of using toxic and expensive chemicals, using green plants as a capping and reducing agent for the synthesis of various types of NCs and NPs for the desired applications is highly recommended (Sivachidambaram *et al*. 2017). Therefore, the present work focuses and intensifies on the synthesis of TiO_2, ZnO and CuO NPs followed by synthesis of TiO_2/rGO and CuO NCs within various volume ratios, characterization using TGA/DTA, XRD, SEM-EDS, TEM, HRTEM, SAED, UV-DRs and FTIR and to investigate the photocatalytic degradation of methylene blue dye under visible light irradiation and to carry out test of their antibacterial and antifungal activities on some selected microbes.

1.2. Statements of the Problem

Previously, several studies and reports have been focused on investigating the photocatalytic activity of chemically synthesized and in some extent green mediated obtained single TiO_2, ZnO and Co_3O_4 NPs for the remediation of polluted water caused by various sources and as well as cost effective nano-drugs. Moreover, earlier reports show that TiO_2/rGO, ZnO/CuO NCs and Co_3O_4 NPs were synthesized by various chemical synthesis protocols for the remediation and recovery of wastewater contaminated by numerous sources and their application on drug resistance microbes such as bacteria and fungi. However, to the knowledge of we the researchers, still now there is no any scientific report on the green synthesis of TiO_2/rGO and ZnO/CuO NCs and Co_3O_4 NPs in the presence of peel extract of CS, MA, and ST as cost effective capping and reducing agent for the efficient photocatalytic degradation of methylene blue dye under visible light irradiation and to investigate the antimicrobial activity. Furthermore, no previous comparative works were presented on the effect of CS, MA, and ST peel waste extracts on the green alternative synthesis of TiO_2/rGO NCs and their effect on the degradation of MB dye.

1.3. Objectives

1.3.1. General objective

Biomediated synthesis of some selected nano-based metal oxides and NCs metal oxides using environmentally available agricultural fruit and vegetable waste materials for photocatalytic and antimicrobial applications.

1.3.2. Specific objectives

The specific objectives of this study were:

- ✓ Preparation of extracts from agricultural fruit waste materials of banana (*Musa acuminate*), Orange (*Citrus sinensis*), and potato (*Solanum tuberosum*) peel.
- ✓ Biomediated synthesis of Co_3O_4, TiO_2, ZnO, CuO NPs, TiO_2/rGO and ZnO/CuO NCs.
- ✓ Characterization of synthesized NPs and NCs using TGA/DTA, XRD, UV-DRs, SEM, EDS, TEM, HRTEM, SAED and FTIR techniques.
- ✓ Evalutation of the photocatalytic activity of the synthesized TiO_2/rGO and ZnO/CuO NCs towards MB dye degradation.
- ✓ Evaluation of antifungal and antibacterial activity of Co_3O_4 NPs and ZnO/CuO NCs towards *Fusarium oxysporum* and *Alternaria solani and K. Pneumoniae, E.Coli, S. Typhi, B. Subtilis and S.Aureus strains*, respectively.

1.4. Significance of the Study

Biomediated synthesis of NPs and NCs involves the use of both different parts of green plants and waste materials. However, using green plants is not recommended and is not an economic way, since it may lead for the existence of hostile environment. Instead, using different fruit waste material extracts can avoid many adverse effects associated with environmental pollution. Therefore, the project provides an insight as waste materials that can pollute the environment can be recycled and used as capping and reducing agent in the synthesis of nanomaterials; in one way the environment is cleaned and in other way they can be used to synthesize NPs without any cost (too green method). The project was also help and creates an opportunities for chemistry masters/undergraduate students of ASTU. The work also provides an insight how different biosynthesized nanomaterials obtained using fruit waste extracts and precursor salts can be used as antimicrobial drug for different types of fungi and bacteria strains that can affect human beings and leads for series health problems and even for death. Moreover, textile and chemical industries can be benefited and share experience from this project, as they can treat waste water released from their factories using such easily synthesized nano catalysts. In addition, the project also provides an insight to pharmaceutical laboratories, as they can synthesize environmentally friendly nano range biocide drugs, instead of using commercially synthesized drugs as antimicrobial agent.

1.5. Scope of the Study

This study was encompasses on the collection of agricultural fruit and vegetable wastes followed by surface cleaning and separation of the peel. Biogenic synthesis of CuO, TiO_2, ZnO, Co_3O_4 NPs and TiO_2/rGO and ZnO/CuO NCs in the presence of peel waste extract of CS, MA, and ST as both capping and reducing agent. Then it was followed by characterization using TGA/DTA, XRD, SEM, EDS, TEM, HRTEM, SAED, UV-DRs and FTIR. Those biogenic synthesized NPs and NCs were investigated as cost effective green catalyst and green nano-drug and applied on some selected drug resistance bacteria and fungi.

2. Literature Review

2.1. Nanomaterials

New technologies often create new challenges to science in addition to their benefits, raise concerns about health and various environmental problems. Nanotechnology is becoming a new area of increasing research and industrial interest since the 1980. Nanotechnology is dealing with the production of materials in a nanometer scale level, normally from 1 to 100 nm. The development of nanotechnology has resulted in a growing public debate on the toxicity and environmental impact of direct and indirect exposures to (NPs). The word “nano” is originated from a Greek word whose meaning is extremely small or dwarf particles. NPs are cluster of atoms having at least one dimension in the size range of 1 - 100 nm (Pan *et al*., 2021).

Nano structured materials have attracted the attention of researchers because of their variety of anticipated features in the technology. Owing to their unique optical, magnetic, catalytic, and electrical properties, NPs have potential applications in various fields. The physicochemical properties of NPs are different as compared to those of their bulk counterparts owing to the fact that surface area to volume ratio increases as the size decreases. Various semiconductor oxide NPs play an important role in various applications such as self- cleaning, gas sensors, optics, Photoelectrochemical devices, solar cell applications, photocatalysis, cosmetic industry, antimicrobial activity and medicinal applications. The integration of nanotechnology into larger systems has provided breakthrough solutions to many current environmental, medical, and industrial problems, including smart materials, nano-manufacturing, electronics, drug delivery, energy and water, biotechnology, information technology, and national security. This is due to the fact that metal oxide semiconductor nanomaterials are inexpensive, non-toxic; possess high surface area to volume ratio, exhibiting tunable properties which can be modified by size reduction, doping, sensitizers, composite form, and affording facility for multi electron transfer process and capable of extended use without substantial loss. Figure 1 shows general application of NPs in different areas (Tilahun Bekele *et al*. 2021; Aldalbahi *et al*. 2020).

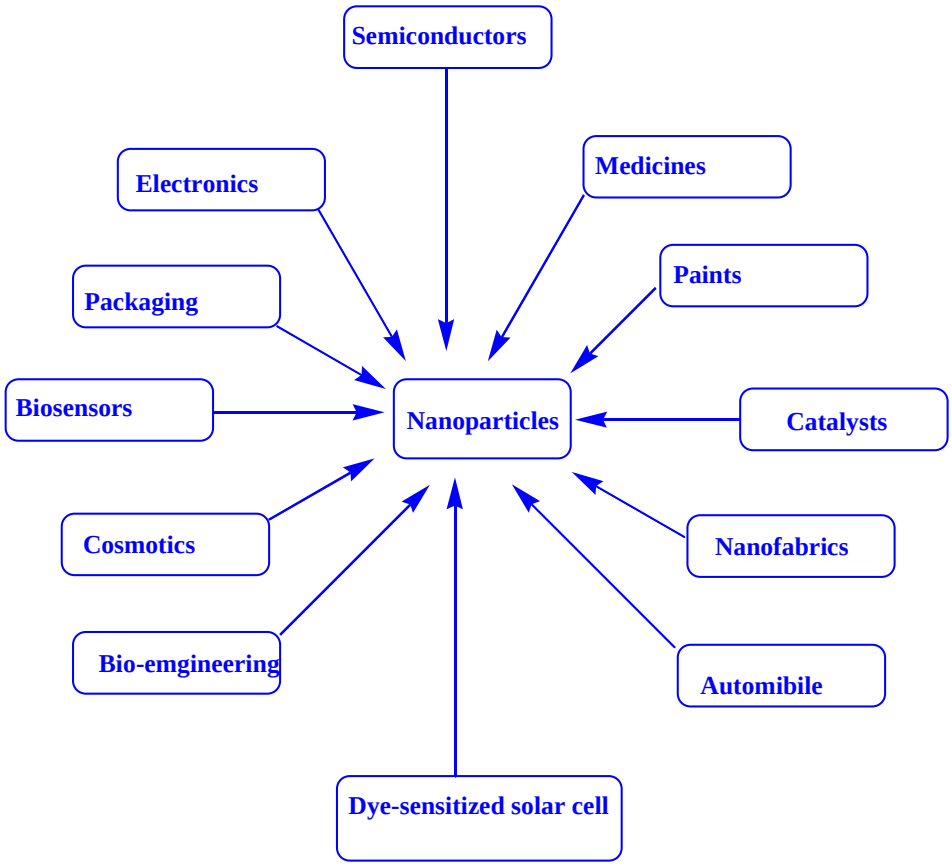

Figure 1: Applications of NPs in various areas.

2.2. Synthesis Methods of Nanomaterials

Generally, nanomaterials can be fabricated through two main approaches, i.e., “top - down” and “bottom - up” approaches. Top-down approach involves the reduction of large materials in its bulk form in to nano scales by applying mechanical force, large particles nano particles. Using this method is not safe because it creates particles with wide size distribution and the produced NPs can be impure. Bottom - up approach involves the joining of atoms by atoms to form NPs. According to research reports, various types of NPs and NCs could be fabricated *via* various physico-chemical techniques such as chemical vapour deposition, micro emulsion, chemical precipitation, hydrothermal, solvothermal, sol-gel, electrochemical and green methods. Among those mentioned protocols, green synthesis of NPs/NCs is getting increased attention because of its simplicity, fastness, ecofriendly and nontoxicity, involves the use of green solvents such as distilled water and ethanol and economical approach. It involves three important steps during the synthesis process such as solvent medium selection, environmental benign reducing and capping agent selection, and non-toxic substances for NPs stability selection. Figure 2 summarizes synthesis protocols of NPs/NCs (Bekele *et al*. 2021; Ajayan and Hebsur 2021).

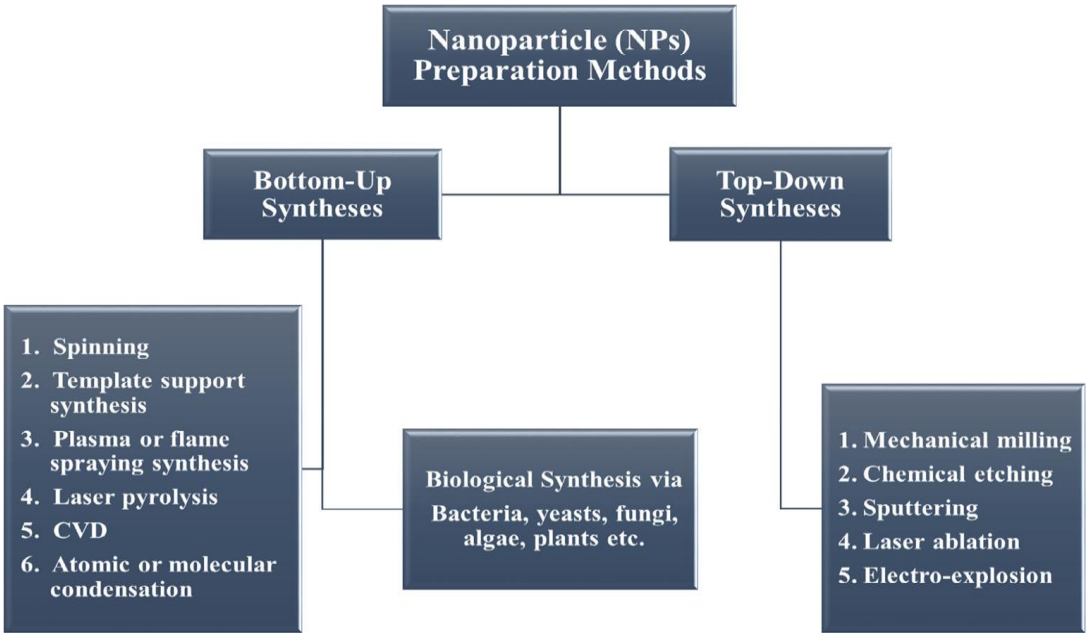

Figure 2: Synthesis methods of NPs.

Biosynthesis of NPs is a kind of bottom up approach where the main reaction occurring is reduction/oxidation. The microbial enzyme or the plant phytochemicals with antioxidant or reducing properties are usually responsible for the preparation of metal and metal oxide NPs. Basically, green chemistry and biological processes have led to develop an environment-friendly process for the synthesis of nanomaterials. A vast array of biological resources available in nature including living plants, plant products and plant extracts, algae, fungi, yeast, bacteria and viruses could all be employed for synthesis of various nanomaterials. Biological methods are considered and regarded as safe, cost effective, biocompatible, non-toxic sustainable and environment friendly processes. Furthermore, most bioprocesses occur under normal air, pressure, and temperature; resulting in vast energy savings, high-yield, and low cost (Adino *et al.*, 2021).

2.3. Biosynthesis of NPs and NCs

Biosynthesis of NPs and NCs using extract of green plant parts (steam, root, leaf, flower, peel and stem) and numerous types of microorganism such as bacteria, fungi, algae and even virus has a number of advantages over conventional methods. The need for biosynthesis of NPs rose as the physical and chemical processes were too costy, involves the use of toxic reagents and chemicals. So, in the search for cheaper pathways for the biosynthesis of NPs and NCs, scientists used microorganisms and plant extracts. Due to the diversity of plants, NPs synthesis from plant extract has known an interesting subject across the world as different plant species are being rapidly investigated and used in NPs synthesis. Currently, it has been

reported that, instead of using green alternative plant parts for the synthesis of various NPS and NCs for the desired applications, using another too green alternative capping and stabilizing agent is highly recommended (Mittal et al., 2013). Since, in one way the environment is cleaned and on the other side, it can be used to synthesize NPS and NCs with zero cost. In general, the biogenic method of synthesis process involves three important steps, (1) solvent medium (2) environmental benign reducing agent selection and (3) selection of non-toxic capping agent in nanomaterials synthesis. Researchers reported that the rate of synthesis of NPs is very high when they use plant extracts instead of microorganisms for biosynthesis of metal NPs, which is a more rapid and reproducible process. The nature of extract used highly affects and alters the kind of NPs to be synthesized in a highly critical manner with the source of extract being used is the most vital factor affecting the morphology, size, and optical behavior of synthesized NPs (Bekele *et al*. 2020; Phiwdang *et al*. 2013).

2.3.1. Biosynthesis of ZnO/CuO NCs

The current attempt in nanotechnology is fabrication of nanomaterials with green procedures, unique characteristics, and high efficiency to be used in various fields (Azeez et al., 2018). The incorporation of metals to an oxide matrix can result in potential materials having chemical/physical properties leading to enhanced performance in various applications. In oxide matrix system having composite materials with matching band potentials, the metal could behave as isolated entity or possess modified property due to interactions between metal and oxygen, which considerably improves the performance of a material and charge separation efficiency. Among metal oxides, zinc oxide (ZnO), an intriguing n-type, direct band gap semiconductor, has drawn attention owing to its appealing properties of green characteristics, excellent stability, single-step synthesis route and low price ZnO NPs is given much attention for biological activity. Previously, it has been reported on the biological activity and applicability of ZnO, MgO and CaO NPs for quantitative assessment against *Escherichia coli* and *Staphylococcus aureus*. ZnO NPs inhibit the bacterial growth by damaging cell membrane and damaged wall shows strong antibacterial activity on spectrum of bacteria (Sawai 2003; (Truong *et al*. 2022; Fagier 2021).

(Rajith Kumar *et al*., 2020) synthesized ZnO/CuO NCs in the presence of *Calotropis gigantea* leaf extract as capping and reducing agent. The XRD analysis confirmed that the average crystallite size of ZnO-CuO NCs was found to be 35 nm having irregular shape as it was supported from the SEM analysis. Moreover, the synthesized NCs were confirmed for the degradation of MB dye with the aid of visible annular type photoreactor under UV light irradiation and the analysis depicts that the synthesized NCs showed degradation efficiency is found to be 97.93% at 105 min. Furthermore, (Mohammadi-Aloucheh *et a*l., 2018) and his co-workers reported on the green synthesis of ZnO/CuO NCs in the presence of *Mentha*

longifolia leaf extract as a green alternative template. From the XRD analysis, within the ZnO/CuO NCs, other than the peaks of hexagonal crystalline phase of ZnO, the reflection peaks of CuO with low intensity were observed, according to its low weight percentages. Additionally, ZnO/CuO NCs, prepared in the presence of the leaf extract, mean particle sizes were decreased, which were in accordance with the results of the XRD analysis. The green synthesized NCs showed antibacterial activity of ZnO/CuO NCs against *E. coli* was higher than that observed for *S. aureus*.

2.3.2. Biosynthesis of TiO_2/rGO NCs

Previously, it has been reported that TiO_2 NPs has been abundantly used and selected as the most reliable candidate as an environmentally clean and pristine photocatalyst due to its desired chemical properties, favorable optical effects, chemically balanced and photochemical stability, dielectric properties, biological and chemical inertness, high redox potential, and good photocatalytic efficiency and nontoxicity. Even though TiO_2 NPs is a material of choice as effective photocatalyst candidate for the purification of water contains pollutants, several limitations such as fast recombination of photo excited electron-hole pairs, wide band gap energy (≈3.2 eV), and agglomeration have been reported. This intern implies that single TiO_2 nanocatalyst could tend to aggregate, agglomerate, narrow spectral band, and show high photo-generated charge recombination rate and these results in shrinking surface area and inferior photocatalytic performance and so lower degradation efficiency. In order to improve and enhance the photocatalytic activity of TiO_2 NPs, several approaches have been revised such as metallic and nonmetallic doping, conductive polymer doping, dye sensitization, and formation of composite by using various synthesis methods. Among these adapted techniques of preventing the electron-hole recombination rate, TiO_2-based composite nanophotocatalysts such as TiO_2/rGO NCs are the most reliable and cost-effective candidates (Yu *et al.*, 2020).

(Kong *et al*., 2016) reported on the synthesis of TiO_2/rGO NCs with enhanced photoelectrochemical performance. The XRD analysis depicts that after hydrothermal treatment of the as-prepared GO nano-sheet a very broad diffraction peak was observed, which means that the GO has been transformed to rGO with significantly less functionalities. UV-Vis diffuse reflectance spectra have been measured to investigate optical absorption of TiO_2/rGO NCs. The absorption edges of the TiO_2/rGO NCs show a slight red shift to longer wavelength indicated by the tangents of each curve, probably due to the formation of Ti-O-C bond between the interface of TiO_2 and rGO, which leads to the band gap of the NCs to become narrow. When the rGO mass ratio in the NCs increases from 0.5 wt% to 1.5 wt%, the improvement of the photocatalytic activity is remarkable due to large surface area and electronic conductivity of rGO, resulting is that the photogenerated electrons transport to the surface of the NCs more easily, thus inhibiting the recombination

between photoinduced electrons and holes. Furthermore, (Wang *et al*., 2013) synthesized TiO_2/rGO NCs for the degradation of phenol aqueous. It has been found that the adsorption of TiO_2-rGO NCs was greatly improved with increasing amount of rGO in the TiO_2-rGO. Since, the photocatalytic decomposition of organic substances takes place on the surface of the prepared photocatalyst, the enrichment of organic substances close to the photocatalyst is an important contributing factor for achieving higher photocatalytic performance. In general in the science of NCs synthesis, especially in the presence of extracts of plants, various volume ratios of extract with the TiO_2/rGO NCs should be done, till highly optimized and best performing NCs will be obtained.

2.3.3. Biosynthesis of Co_3O_4 NPs

Reports showed that synthesis of Co_3O_4 NPs has been reported using various methods such as thermal decomposition, template method, hydrothermal method, microwave-assisted, and chemical spray pyrolysis (Bekele et al., 2022). These methods are usually consume more energy, are capital intensive, and use toxic chemicals in the preparation process. As an alternative to these traditional methods, green synthesis is considered to be a safe, economic, and ecological method for the preparation of NPs. Such green methods used raw materials like microscopic organism especially a bacterium or fungus, polymeric substance occurring in living organism-alginate and bioactive molecule contained in plants. Previously, Co_3O_4 NPs have been synthesized by green synthesis method using plants such as *Calotropis gigantea*, *Moringa oleifera*, *Aspalathus linearis*, *Terminalia chebula*, *Sageretia thea*, *Calotropis procera*, *Manihot esculenta Crantz, Euphorbia heteropyhlla L*., *Phytolacca dodecandra* and many others. Previously, (Adino *et al*., 2021) and his co-authors reports on the green synthesis of Co_3O_4 NPs in the presence of leaf extract of *Phytolacca dodecandra* for antibacterial activity. The report showed that average crystalline size of biologically synthesized Co_3O_4 NPs were found to be 10.79 nm with high diffraction peak broadening having spherical in shape as was confirmed by the SEM analysis. And the antibacterial potential of the green synthesized nano-drug was found to be very effective towards *E.coli*. Furthermore, (Dewi *et al*., 2019) synthesized Co_3O_4 NPs in the presence of *Euphorbia heterophylla* L. leaves extract as a green template. The photocatalytic activity of Co_3O_4 NPs was performed for the degradation of methylene blue was about 63.105% under visible light irradiation for 3 hours. In addition, Co_3O_4 NPs were synthesized using *Camellia sinensi* (L.) Kuntze and *Apium graveolens* extract, which is a green method of NPs synthesis that does not introduce harmful substances into the environment and ensures cost effectiveness. The average particle size was calculated to be in the range of 21-55 nm and it showed inhibited the growth of *S. aureus*, *P. aerugino* (Urabe & Aziz, 2019).

2.4. Applications of NPs and NCs

2.4.1. Photocatalytic Applications of TiO_2/rGO and ZnO/CuO NCs

The intensification of human activities associated with economic development has caused the increase of waste generation and the pollution of various parts of the natural ecosystem, particularly the numerous types of water bodies, which is the pillar resource for the existence of every living thing. It has been reported that the textile industries, leather and dye industries, pesticide factories, cosmetic, detergent and chemical industries for instance involves the use of highly reactive dyes, such as methylene blue and methyl orange, which are harmful to the natural environment due to their high carcinogenic and mutagenic nature and as well their less degradation nature by conventional techniques (Zelekew *et al*. 2021; Nasrollahzadeh *et al*. 2017). When those pollutants and dyes are discarded into the water bodies without adequate treatment, they could results in changing the color of water bodies, promoting significant changes in the hydrological cycle; thus could lead to severe diseases such as cancer and even to the death of human beings. Thus, the degradation and removal of those organic dyes from water bodies is of great environmental and industrial importance. A number of miscellaneous methods such as ion exchange, reverse osmosis, membrane filtration, adsorption processes, chlorination, chemical precipitation and electrochemical methods, sedimentation-flocculation and coagulation as well molecular sieving have been widely explored for water treatment containing wastes but those protocols cannot completely degrade the organic pollutants and also results in the formation of secondary pollutants (Rambabu *et al*. 2021; Jokar *et al*. 2019). Recent studies have shown that advanced oxidation process (AOPs) using heterogeneous green mediated synthesized catalysis in the presence of visible light irradiation are the best alternative techniques for the decontamination of wastewater as compared to conventional methods due to low-cost and high stability, nontoxicity, absence of resistance to mass transfer and secondary pollution, operation under ambient conditions, high surface area to volume ratio, energy efficient, environmentally safe and more importantly the potential for decomposing the recalcitrant organic pollutants at short reaction time into less and zero harmful forms (Huang et al. 2021;Yin *et al*. 2020).

Currently, various semiconductor-based nanomaterials have attracted a significant interest for the purification and treatment of wastewater (Thatikayala & Min, 2021). Among these, nanosized metal oxide photocatalysts such as TiO_2, CuO, Co_3O_4, ZnO, ZnS, CdS, Fe_2O_3, MgO, Mn_2O_3, ZrO_2, V_2O_5, Nb_2O_5, and WO_3 have been investigated and used in the process of wastewater decontamination. Particularly, wastewater decontamination using high surface area semiconductor NCs photocatalysts prepared via numerous techniques has shown improved potential. Previously, it has been reported that ZnO and TiO_2 NPs has been abundantly used and selected as reliable candidate and an environmentally clean and pristine

photocatalyst due to their desired chemical properties, favorable optical effects, chemically balanced and photochemical stability, dielectric properties, biological and chemical inertness, high redox potential, and good photocatalytic efficiency and nontoxicity. Even though ZnO and TiO_2 NPs are a material of choice as effective photocatalyst candidate for the purification of water contains pollutants, several limitations such as fast recombination of photo excited electron-hole pairs, wide band gap energy, and agglomeration have been reported. This intern implies that single ZnO and TiO_2 nanocatalysts could tend to aggregate, agglomerate, narrow spectral band, and show high photo-generated charge recombination rate and these results in shrinking surface area and inferior photocatalytic performance and so lower degradation efficiency (Shimi *et al*. 2022; Pal *et a*l. 2018).

Now today, in order to enhance the photocatalytic degradation performance of those single metal oxide NPs, various advanced improvement techniques are carried out such as metallic and non-metallic doping, conductive polymer doping, dye sensitization, and formation of composite by using various synthesis methods. Previously, several methods have been explored and used for metal oxide NCs synthesis for the desired applications such as hydrothermal, electrochemistry, wet chemical, microwave method, coprecipitation, sol-gel, precipitation, wet impregnation and thermal decomposition (Pavan Kumar et al., 2015). However, these classical methods used to synthesize metal oxide NCs and NPs involves the use of hazardous and expensive capping and reducing agent chemicals, which could result in negative effect for the ecology of the natural ecosystem. As a result, an alternative green synthesis of NCs has received special attention of the researchers, specifically via green protocols, due to their availability, cost effectiveness, involves the use of too green solvents and reagents such as ethanol and distilled water and environmental friendless. Furthermore, the green synthesis method could be performed using various parts of green plants such as roots, stems, flowers, fruits, peels, and their combinations, which is available with minimal cost. Moreover, using of peel extract as a capping and reducing agent for the synthesis of various types of MONPs and NCs could be the most preferable technique; since this way provides more advantages such as in one way the environment is cleaned while using the peels which pollutes the environment once discarded to the environment as a waste and in the other side, those peels could be accessed from the environment with zero cost (Muniandy *et al*. 2017; Sabir *et al*. 2020; Chen *et al.* 2020).

(Lv *et al*., 2021) and his co-authors synthesized CuO loaded ZnO NCs for the degradation of MB under visible light irradiation. The analysis proves that CuO loaded ZnO NCs showed enhanced result as compared to the relative single oxide NPs. This might be due to the increased surface area of the NCs, which allows for the adsorption of more MB dye on the surface of the NCs in the presence of visible light. Similarly, (Shinde *et al*., 2022) synthesized ZnO/CuO NCs for crystal violet dye degradation. The UV-Vis

absorption study clearly showed that the concentration of CV dye in the solution continuously decreases as the contact of the CV dye with the catalyst increases from 0 to 120 min. The decrease concentration is attributed to the efficient photodegradation of CV dye using ZnO/CuO NCs photocatalyst. Furthermore, (Prajapati & Mondal, 2021) report on the green synthesis of CuO-ZnO-C NCs using marigold (Tagetes spp.) flower extract for the degradation of Congo red dye. The result showed that at low pH of the dye solution, the surface of the NCs formed more positively charged due to the protonation up to pHPZC of NCs, which was an excellent binding condition between positively charged NCs surface and anionic dye molecules. On the other hand, increasing the pH of dye solution, the surface of both NPs formed negatively charged surface due to OH groups, which reduces the adsorption capacity of the NCs due to the same charge density between NCs and dye molecules.

2.4.2. Antimicrobial Applications of ZnO/CuO NCs and Co_3O_4 NPs

Microbial infectious diseases are serious health problem that has drawn the public attention in worldwide human health threat, which extends to economic and social complications. Since the discovery of Penicillin in 1928, huge improvements in global health and life expectancy have been observed. However, due to the excessive use of antibiotics, antimicrobial resistance has emerged as one of the greatest threat to human health worldwide. Due to development of drug resistance in pathogenic bacteria and fungi, the commonly treated illnesses yesterday are becoming lethal today. Hence, new strategies and approaches are highly demanded to take the major health care challenge posed by rapidly spreading antibiotic resistant bacteria and fungi (Bloom & Cadarette, 2019).

Report supports that in recent years, the frequency of fungal infections and fungal contamination in daily life has rapidly grown due to the serious threats of environmental pollution and climate change (Singh et al., 2018). The progression of fungal infections and contamination not only increases the chances of human illness, but is also one of the leading causes of economic loss during the harvest and storage of agricultural products (Seventer *et al*., 2020). Many varieties of harmful fungi such as *Pathogenic fungi*, *Magnaporthe oryzae*, *Penicillium*, and *Aspergillus Niger* can cause disease in agronomic, horticulture, ornamental, and forest plants. *Magnaporthe oryzae* is a fungus that causes blast in rice and can also infect many other cereal crops such as barley, oats, and rye grass. *Neoscytalidium dimidiatum* is another fungus that causes disease in many host plants. Today, many new and highly effective antifungal materials have been investigated to replace longstanding and traditional and less effective antifungal agents. In recent years, several types of nanomaterials such as single oxides, NCs, and others have been synthesized by various methods and demonstrated to be resistant to fungi, along with their superior physical and chemical properties (Phiwdang *et al.*, 2013).

(Uyen *et al.*, 2020), reports on the synthesis of CuO-ZnO NCs as effective antifungal drug against *Magnaporthe Oryzae, Penicillium, Aspergillus and Neoscytalidium Dimidiatum*. The analysis proved that, as the concentration of the drug is increased, the inhibition level also improved. Of the four types of fungi, *Aspergillus* and *Penicillium* were found to be completely inhibited with a concentration of 5 mg/mL of CuO-ZnO NCs. The remaining two kinds of fungi, the minimum inhibitory concentration were 10 mg/mL. CuO-ZnO NCs showed enhanced inhibition towards *Penicillium* and *Aspergillus* than that of *Magnaporthe* and *Neoscytalidium*. This might be due to the distinct growth morphology and the constitutive tolerant of each fungus. The resistance of bacteria and fungi to the available antibiotics and drugs is at an alarming rate. Therefore, there is a need for strong antifungal agents that can destroy fungi that are resistant to the drugs available. Recently, Co_3O_4 NPs have attracted considerable attention because they are more economical than the noble MNPs and show different properties. Co_3O_4 NPs have been explored as a therapeutic agent for the treatment of diseases, such as microbial infection, which make them attractive for biomedical applications. Co_3O_4 NPs are nontoxic in the body at lower levels, have strong activities against bacteria and fungi at lower concentrations, and have fewer side effects than antibiotics. Various reports on the antifungal activity of green-synthesized Co_3O_4 NPs were intensively conducted, and the result showed as the green synthesized NPs have strong antifungal activities against *Candida krusei*, *Candida guilliermondii*, *Candida glabrata*, and *Candida albicans*. Similarly, Co_3O_4 NPs synthesized using flower extract of *H. Rosa-sinensis* and showed enhanced antifungal activity against *Aspergillus flavus* and *A. Niger* (Ertaş *et al.*, 2015).

In addition to fungal caused diseases spread worldwide, bacteria infectious diseases are also fatal to the world community, which needs serious attention. It has been reported that, ulcerative skin infections arising from the colonization and development of Gram-positive bacteria, Gram-negative bacteria, and multidrug-resistant bacteria are significant health-care problems that seriously affect human skin (Govindasamy et al., 2021). A prospective quantitative study reported that the prevalence rates of skin pressure ulcers (PUs) are 15.5% in Kuala Lumpur, Malaysia, 33% in Palestine, and 16% in Bandung, Indonesia. Skin infection has been found in 60 (74.0%) of the collected samples from PUs of hospitalized patients, and these PUs primarily comprise *Enterobacteriaceae* strains (49.0%), such as *Escherichia coli* (*E. coli*), *Klebsiella pneumoniae* (*K. pneumoniae*), *Enterobacter* spp., and *Proteus* spp.; followed by *Staphylococcus aureus* (*S. aureus*) (28.0%) and nonfermenting GNB (23.0%), mostly *Pseudomonas aeruginosa* (*P. aeruginosa*), *Acinetobacter* spp., and methicillin-resistant *S. aureus* (MRSA). (Mohammadi-Aloucheh *et al.*, 2018) reports on the green synthesis of ZnO and ZnO/CuO NCs s in *Mentha Longifolia* leaf extract as antibacterial agent towards *Escherichia coli* (Gram-negative), and *Staphylococcus aureus* (Gram-positive). XRD analysis confirms as the synthesized ZnO/CuO NCs within various compositions, their peaks were corresponding to hexagonal

crystalline phase having spherical morphology as can be checked by the SEM-TEM analysis. The formed NCs were found to be very effective to the target bacteria.

(Thatikayala & Min, 2021) reports on the antibacterial activity of Ginkgo leave extract-assisted synthesis of ZnO/CuO NCs. The XRD result confirms that the change in lattice parameters of the green ZnO/CuO NCs compared with the standard values of pure ZnO and CuO due to the ion doing and grain refinement results in intra-granular coupling intimate contact between both the phases of ZnO and CuO and advances the effectiveness for the formation of heterojunction. The TEM images of ZnO/CuO NCs appear nearly spherical with a particle diameter of 22 to 26 nm. Each ZnO has formed a heterojunction with CuO and has a thickness of 11 to 15 nm of particle size. The antibacterial activities of ginkgo leaf extract, synthesized ZnO, CuO, and ZnO/CuO NCs were examined by agar well diffusion method toward gram-positive (*S. aureus*) and gram-negative (*E.coli*) bacteria at 50, 100, 150, and 200 μL). The report proved that the antibacterial activity of the green synthesized NPs and NCs potential increase with an increase in concentration. Moreover, the ZnO/CuO NCs exhibited higher antibacterial activity than ZnO and CuO due to synergistic bactericidal effect between ZnO and CuO, respectively.

Furthermore, many reports were carried out on the green synthesis of Co_3O_4 NPs to investigate its antibacterial activity (Ren et al., 2009). In addition to its suitable physico-chemical properties, Co_3O_4 NPs is an antiferromagnetic material and mainly has biomedical. Cobalt contains vitamin B12, which is more essential for human health. In its spinel structure, all the bivalent ions (Co^{2+}) occupied in the tetrahedral sites, and trivalent ions (Co^{3+}) occupied the octahedral sites and O^{2-} ions are present in 32(e) sites in a cubic close-packed structure. (Kombaiah *et al*., 2018) reports on the green fabrication of Co_3O_4 NPs using *Vitis vinifera* extract and investigates its potential antibacterial activity towards Gram-negative (*Pseudomonas aeruginosa*, and *Escherichia coli*) and Gram-positive (*Staphylococcus aureus* and *Bacillus subtilis*) bacterial pathogens. The enhanced zone of inhibition was observed against *S. aureus*, this indicates that the bacteria have not developed resistance towards the prepared samples and this intern proved the biocidal activity of the green nano-drug. Moreover, nanorods are considered as efficient in causing abrasive action on the cell wall which may lead to the membrane damage. The enhanced bioactivities of the nanorods are contributed due to the improved surface area. Additionally, (Urabe & Aziz, 2019) reports on the biosynthesis of Co_3O_4 NPs using extract of *Camellia sinensis* (L.) Kuntze and *Apium graveolens* L. and deal their antibacterial activity. Co_3O_4 NPs with *Apium graveolens* and Co_3O_4 NPs with *Camellia sinensis* leave extract templated showed zone of inhibition against *S. aureus* and *P. aerugino* as 22, 25, 27 and 29, respectively. The enhanced antibacterial activity of the synthesized Co_3O_4 nano-drugs synthesized via the

presence of two plant extract might be due to their high surface area to volume ratio and as well due to the production of ROS, which results enhance the killing of those bacterial cells.

3. Methodology

3. 1. Chemicals and Reagents

The necessary chemicals, solvents, and reagents used in this work were titanium tetra butoxide ($Ti(OC_4H_9)_4$ 97%, Sigma-Aldrich), sulfuric acid (H_2SO_4 98%, Sigma-Aldrich), phosphoric acid (H_3PO_4 ,65%, Sigma-Aldrich), hydrochloric acid (HCl 36-38%, Sigma-Aldrich), hydrogen peroxide (H_2O_2 30%, Sigma-Aldrich), potassium permanganate ($KMnO_4$, Alpha), Barium chloride ($BaCl_2$, Alpha), methylene blue ($C_{16}H_{18}ClN_3S$, 99%, LOBA Chemia), ethanol (C_2H_5OH 97%, Silva, Ethiopia), graphite powder (diameter 6 mm, 99.995% trace metals basis, Sigma-Aldrich), zinc (II) acetate dehydrate [$Zn(CH_3\ COO)_2{\cdot}2H_2O$] (99% pure), copper (II) nitrate trihydrate [$Cu(NO_3)_2.3H_2O$] (99% pure), sodium hydroxide (NaOH 97% pure) and ethanol (sigma Aldrich, 97% pure), acetone (Sigma-Aldrich), dimethyl sulfoxide (DEMSO, Sigma-Aldrich), and Müller-Hinton agar (Sigma-Aldrich) and Cobalt nitrate hexahydrate (98%, Sigma Aldrich). All those chemicals and reagents area of analytical grades and were used without conducting further purification process.

3.2. Apparatuses and Instruments

The laboratory apparatus and equipments used for this work were beakers, conical flasks, funnel, volumetric flasks, borosilicate glass, scissors, mortar and pestle, PDA plates, Whatman filter paper number-2, crucible dish, cuvette, spatula, analytical balance, hot plate with Magnetic Stirrer, drying oven and muffle furnace. Different instruments were also used such as thermo gravimetric analysis (TGA/DTA, DTG-60H Shimadzu Co., South Korea), FTIR (T/IR-6600 type A, JASCO Company, Japan), XRD (XRD-7000, Shimadzu Co., South Korea), UV-DRS (OPTIMA UV-Vis spectrometer SP-3000 Plus, SHIMADZU Corporation, Japan). The scanning electron microscopy with energy-dispersive X-ray spectroscopy (SEM-EDX-EVO 18 model with low vacuum facility and ALTO 1000 Cryo attachment) and transmission electron microscope with high-resolution (JEOL JEM 2100 HRTEM) were used for understanding morphological and structural features of the peel mediated synthesized NPs and NCs. Furthermore, photocatalytic degradation studies of MB dye using ZnO and TiO_2 nanocatalyst and TiO_2/rGO and ZnO/CuO NCs catalyst were carried out in 125mL of Pyrex flask type reactor under 150W halogen lamp irradiation. Degradation analysis was followed and recorded using double beam UV-visible spectrophotometer(SM-1600 spectrometer MAALAB, India).

3. 3. Fruit Peel Waste Collection and Extraction

3.3.1. Collection and Extraction of *Musa Acuminata* Peel

MA peel was obtained from local fruit market located in Adama city, East Showa Zone, Oromia Regional state, Ethiopia. The collected peels were surface cleaned and washed several times with distilled water as presented in Figure3 to avoid any surface contaminants. Then after, the peels were allowed to dry under shadow and ground into a moderately fine powder using micro plant grinding machine. Afterwards, 30 g of the fine peel powder was taken and dissolved within 300 mL of distilled water and stirred for an hour at 50℃. Finally, the boiled suspension were allowed room temperature cooling and filtered using Whitman filter paper and stored in a refrigerator at 4℃ for further use (Ertaş *et al*., 2015). Peel waste extract of CS and ST were conducted following the same procedure.

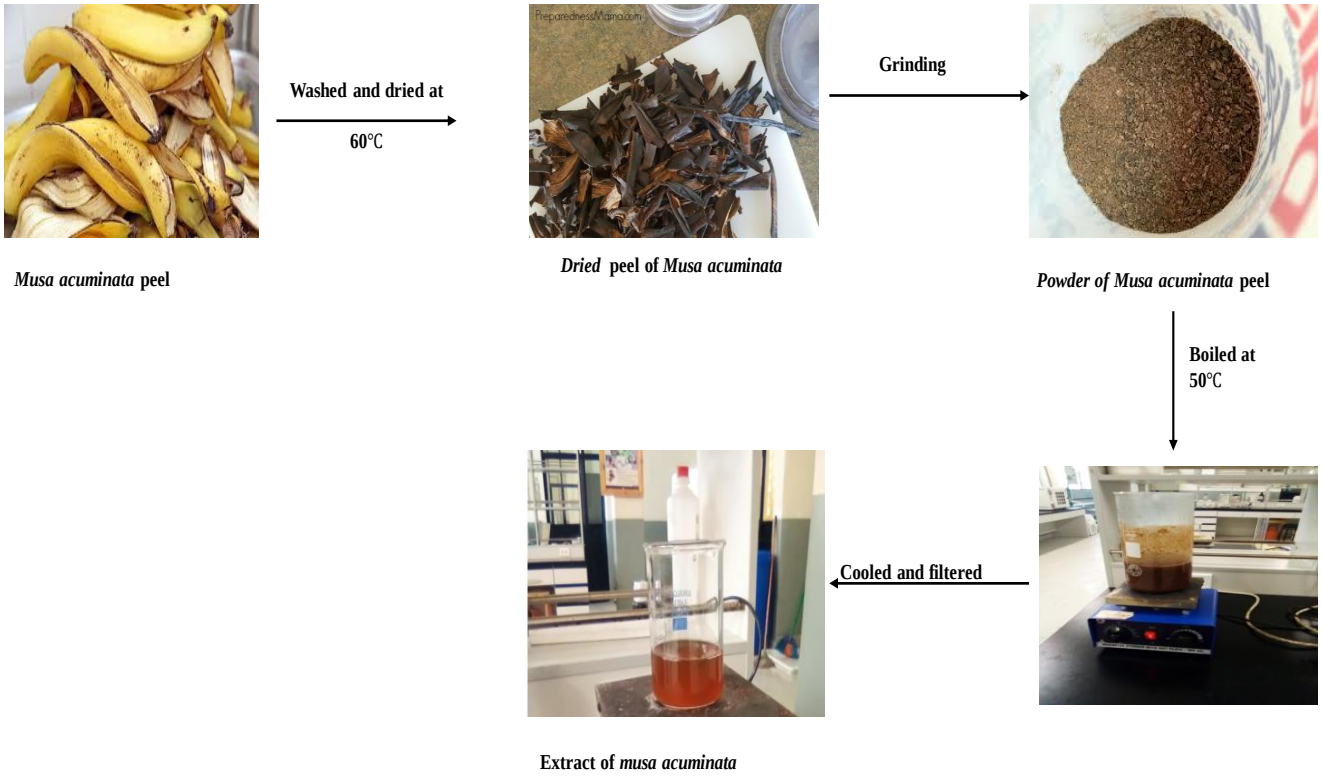

Figure 3: Schematic representations of MA fruit peel extract.

3.4. Biogenic Synthesis of TiO_2/rGO, ZnO/CuO, and Co_3O_4 Nanomaterials

3.4.1. Biogenic Synthesis of TiO_2/rGO NCs using SC and MA Peel Extract

Fresh and healthy fruits of CS (sweet orange) and *Musa acuminata* (banana) were collected from the local market of Adama City, Oromia Region, Ethiopia. The collected samples were washed several times using

distilled water to remove surface dust particles. Then, the peel parts were taken using knife and allowed shadow drying. The peels were then grinded and packed in a glass bottle followed by covering with aluminum foil to avoid photodegradation. The extraction was carried out by taking 15 g of fine peel powder of each peel and then added into 500 mL conical flask separately followed by adding 250 mL of distilled water. Each of the mixtures of water and peel powder present in the separated conical flask was then boiled at a constant temperature of 70℃ for 45 minutes while string using a magnetic stirrer at 1000 rpm and cooled to room temperature and filtered using watchman filter paper (Mobeen Amanulla & Sundaram, 2019). Finally, the filtrates were stored at 4℃ in a refrigerator for the synthesis of TiO_2 NPs and TiO_2/rGO NCs.

TiO_2 NPs were synthesized via sol-gel method using titanium tetra-butoxide as a precursor in the presence of CS and MA as capping and reducing agent in three different volume ratios (1:2, 1:1, and 2:1). In typical reaction, 0.25 M of 40, 50, and 60 mL of $C_{16}H_{36}O_4$ titanium precursor solutions were added into three different Erlenmeyer flasks followed by stirring for about 30 minutes to maintain homogeneity. Then, in each erlenmeyer flask containing the precursor solution, 60, 50, and 40 mL of CS peel extract were added drop by drop, respectively and labeled as 1:2 (TiO_2-0.5c), 1:1 (TiO_2-1c), and 2:1 (TiO_2-2c). The reaction mixtures were stirred for about 5 hours using magnetic stirrer at room temperature. Then afterward, 17 mL of 1 M NaOH solution was added drop wise to facilitate precipitation and was stirred for about 30 minutes in order to maintain the homogeneity of the solution and the formed suspensions were kept at 4℃ in a refrigerator for overnight for further use. The three different volume ratio suspensions were then centrifuged three times at 4000 rpm followed by washing three times using distilled water and absolute ethanol followed by collecting using crucible ceramic dish and then oven dry (Umekar *et al*., 2020). The thermal stability of the dried samples was tested by taking the 1:1 ratio from each of the peel waste mediated synthesized TiO_2 samples. Based on the thermal stability result, the three ratios of CS peel extract mediated synthesized TiO_2 NPs were calcined at 500℃ for about 4 hours. The same protocol was followed for the MA peel extract mediated synthesis of TiO_2 NPs and labeled as 1:2 (TiO_2-0.5m), 1:1 (TiO_2-1m), and 2:1 (TiO_2-2m). Figure 4 shows the schematic synthetic procedure of TiO_2 NPs in the presence of CS peel waste extract.

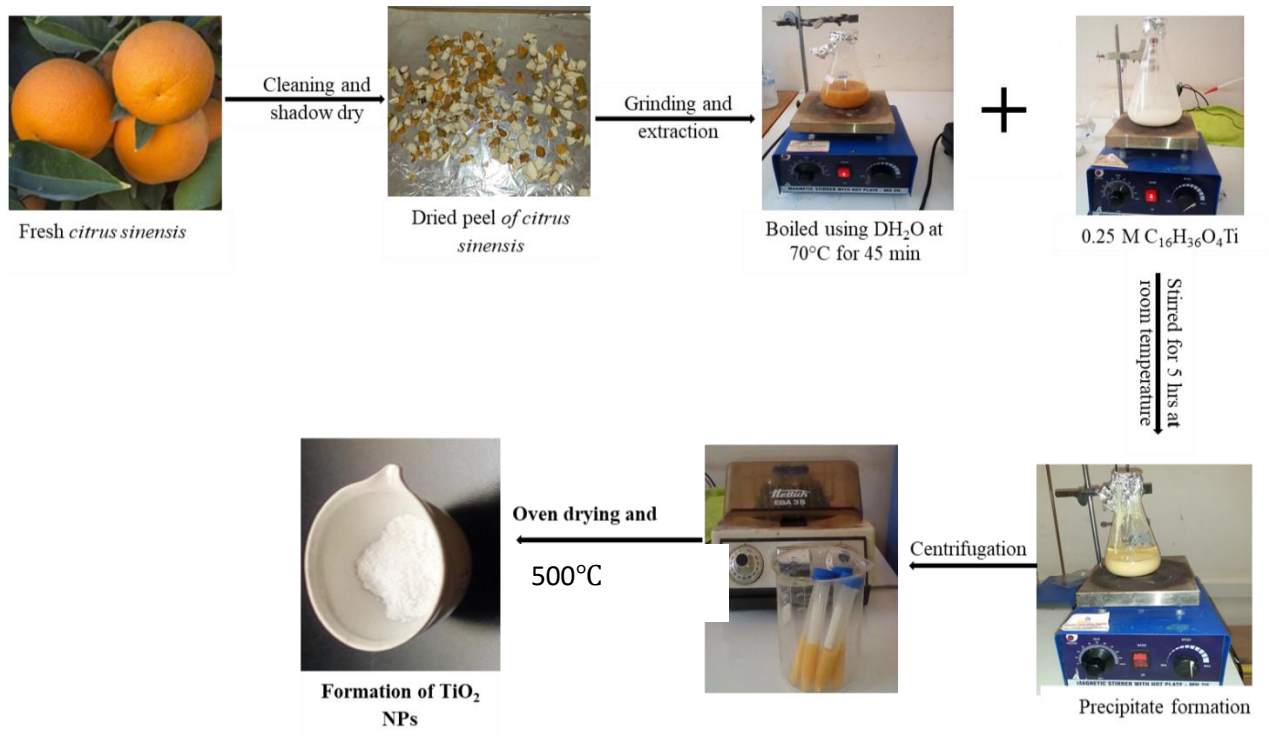

Figure 4: Schematic green synthesis procedure of TiO_2 (1:1) NPs in the presenc of CS peel extract.

Synthesis of GO was carried out following the modified Tour Method (Habte et al., 2019). The synthesis procedure involved oxidation of graphite using strong oxidizing agent ($KMnO_4$) in the presence of H_3PO_4 to prevent further possible oxidation. Then after, 0.5 g of graphite powder was exfoliated using 90 mL of H_2SO_4 followed by addition of 50 mL CS peel waste extract in the presence of H_3PO_4 at 0^oC in ice bath followed by gradual and stepwise addition of 4.5 g $KMnO_4$. Then, the components were stirred for about 8 hours while heating at 50℃ using a temperature-controlled water bath. As the reaction time was extended and increased, the mixture turned out to paste. The reaction was then terminated by the addition of 250 mL of distilled water followed by addition of 10 mL H_2O_2 (30%) solution to reduce residual $KMnO_4$ to soluble manganese sulfate ($MnSO_4$) in an acidic medium. The formed suspension was then filtered to remove the metal sulfate and a graphite oxide filter cake was produced. The cake was then again washed using 5% of HCl until the sulfate ions are completely removed, which was confirmed using $BaCl_2$ solution. The formed graphite oxide was washed three times at each centrifugation process at 1000 rpm for 30 minutes. The collected graphite oxide was added to 100 mL of distilled water and stirred followed by heating at 60℃ for 8 hours in water bath. The brown colored GO solution was dried at 60℃ for 6 hours in oven drier. Figure 5 displays the resulting schematic synthesis protocol of GO in the presence of peel waste extract of CS as a green alternative template.

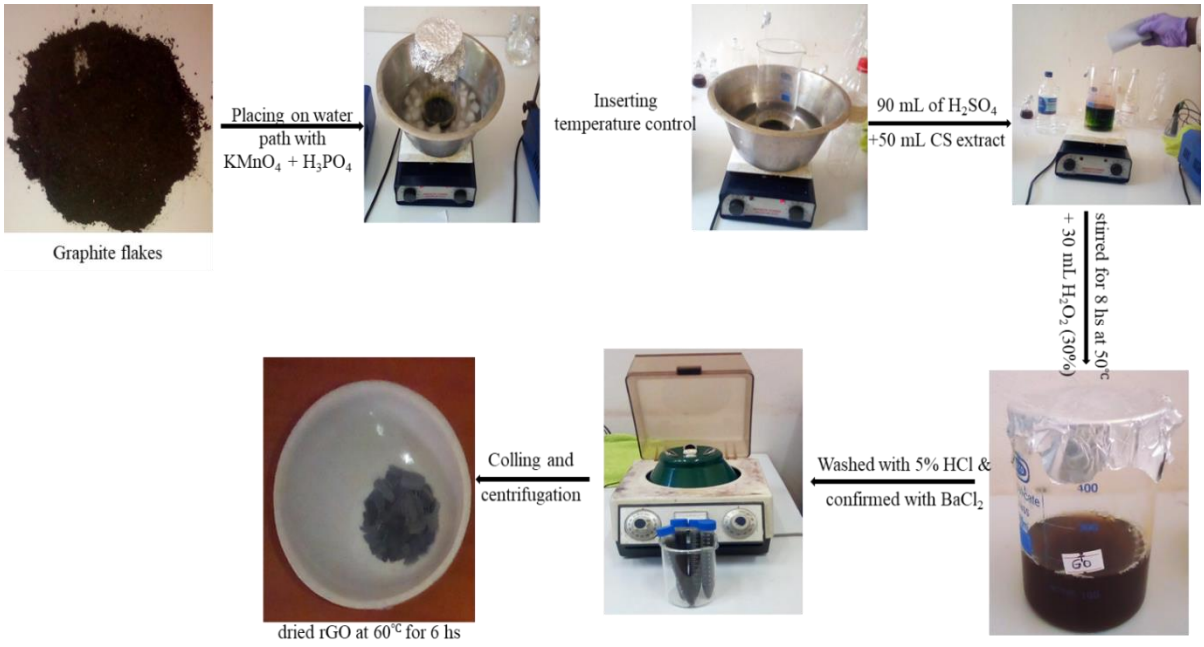

Figure 5: Diagrammatic synthesis procedure of rGO using CS peels extract.

The TiO_2/rGO NCs were prepared using synthesized GO and TiO_2 via precipitation method in the presence of peel waste extract of CS and MA as both reducing and stabilizing agent. In a typical procedure, GO suspension was prepared by dispersing dried 30, 60 and 90 mg powders in 100 mL of distilled water by the process of sonication. Subsequently, 60 mg of TiO_2 and 50 mL of CS extract were added into the GO slurry and stirred for about 8 h at room temperature. Then, the solution turned to gray from brown colors indicating the reduction of GO to reduced graphene oxide (rGO). The gray residue of the formed rGO/TiO_2-0.5c, rGO/TiO_2-1c, and rGO/TiO_2-1.5c NCs were then centrifuged for a minimum of 30 minutes followed by washing three times using distilled water and absolute ethanol sequentially at each step of centrifugation to remove impurities. The obtained NCs were then kept in vacuumed oven at 100℃ for about 24 hours for further analysis (Štengl *et al.*, 2013). The same procedure was followed for the MA peel extract mediated synthesis and labeled as TiO_2/rGO-0.5m,TiO_2/rGO-1m and TiO_2/rGO-1.5m NCs.

3.4.2. Biogenic Synthesis of ZnO/CuO NCs using MA Peel Extract

The synthesis of ZnO NPs via green sol gel method was carried out by dissolving 4.04 g of zinc (II) acetate dihydrate [Zn $(CH_3COO)_2{\cdot}2H_2O$] within 66 mL distilled water to prepare 0.27M precursor salt of concentration followed by drop wise addition of this solution into 33 mL of aqueous extract of MA peel under continues stirring up on placing it on a magnetic stirrer at room temperature. After 2:30 hrs stirring, 1 M aqueous solution of NaOH was added drop wisely into the suspension under stirring to adjust the pH to 12. Then, the suspension was stirred for additional 1:30 hrs to maintain the homogenous distribution of the

added base. The formed suspension mixture was kept for about 24 hrs within a refrigerator. Then after, the formed gel was centrifuged three times followed by washing with distilled water and ethanol at each consecutive step. Then, the formed ZnO NPs was dried in an oven at 60℃ for an hour followed by thermal stability analysis and based on the thermal analysis result it was calcined at 450℃ for about 2 hrs. The same step was repeated for 0.36 M and 0.55 M of zinc acetate while keeping the volume of the peel extract constant. For simplification, the synthesized samples were labeled as 1:1, 1:2, and 1:3 indicating 0.27 M, 0.36 M and 0.55 M of zinc acetate for the same volume (33 mL) of peel extract, respectively. The same procedure was carried out for the green synthesis of CuO NPs, which was performed by dissolving 4.56 g of $Cu(NO_3)_2.3H_2O$ in 66 mL distilled water while using the same volume of the peel extract (Multiple & Perspectives, 2022).

The ZnO/CuO NCs were synthesized by the sol gel method in the presence of 33 mL of suspension of peel of MA. In the case of the ZnO/CuO (10%) NCs synthesis, 2.29 g of zinc (II) acetate dehydrate $[Zn(CH_3COO)_2{\cdot}2H_2O]$ and 0.337g of copper (II) nitrate trihydrate $[Cu\ (NO_3)_2.3H_2O]$ were each dissolved in 40 mL of distilled water in different beaker. Then, 40 mL zinc acetate solution was added drop by drop into 33 mL of aqueous extract of the peel upon continues stirring. After 30 min continuous stirring, 40 mL copper nitrate solution was added drop by drop to the above solution. After 30 min of stirring, the pH of the solution was adjusted to be 12 after drop wise addition of an aqueous solution of 1 M NaOH. After continuous stirring for about 3 hrs, the solution was kept for about 24 hrs to form a gel and washed with distilled water and ethanol three times. Then, the gel was dried in an oven at 60℃ and calcined at 500℃ for 2 hrs to obtain the required ZnO/CuO (10%) NCs. For synthesis of ZnO/CuO NCs with (15%), 20% and (25%) proportions, the amounts of copper nitrate used were 0.53g, 0.76g, and 1.01g, respectively for the same gram (2.29) of zinc acetate precursor with same volume (33 mL) of extract. For simplification, they were labeled as ZC10, ZC15, ZC20, and ZC25, to represent ZnO/CuO (10%), ZnO/CuO (15%), ZnO/CuO (20%) and ZnO/CuO (25%), respectively. Figure 6 depicts the schematic green synthesis protocol of ZnO/CuO (20%) NCs (Yulizar *et al*., 2018).

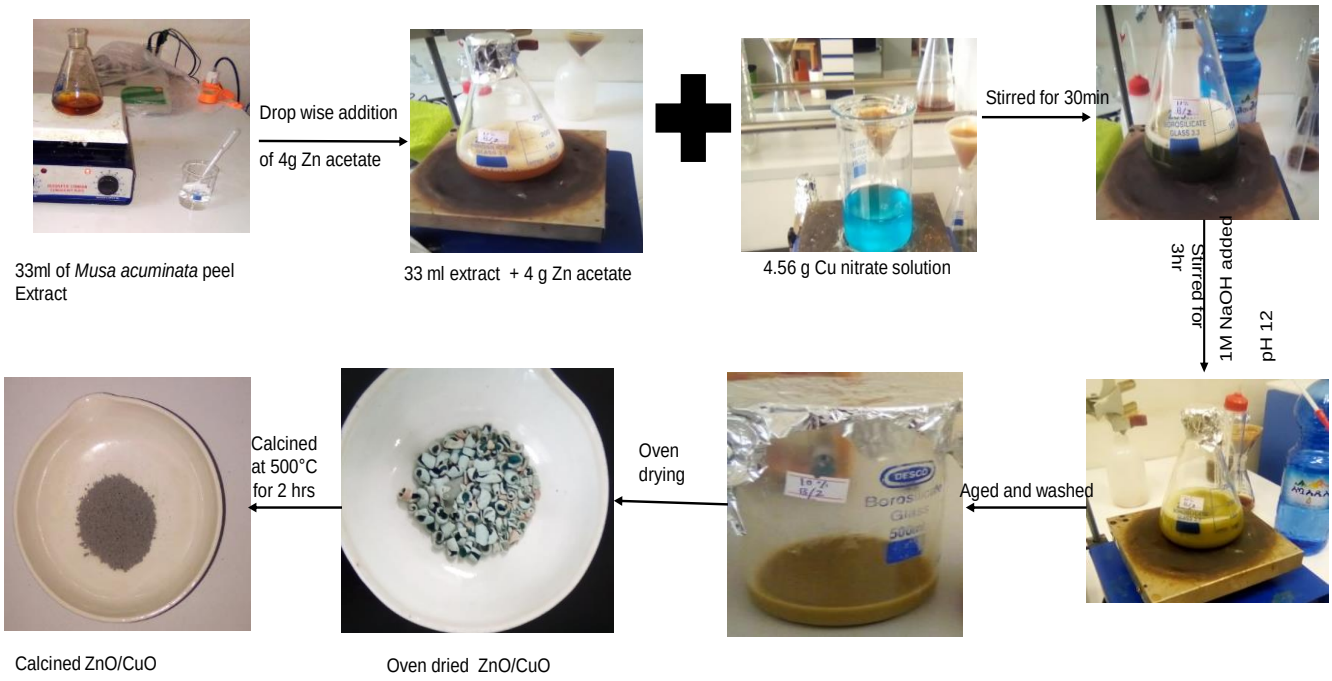

Figure 6: Schematic green synthesizes representation of ZnO/CuO (20%) NCs.

3.4.3. Biogenic Synthesis of Co_3O_4 NPs using ST Peel Extract

Co_3O_4 NPs were synthesized as described below: first 0.25 M of cobalt nitrate solution was prepared. The synthesis method was carried out within three volume ratio of extract and precursor salt as: 50 mL of 0.25M cobalt nitrate solution was mixed with 50 mL of extract (1:1), 66.7 mL of 0.25 M cobalt nitrate solution was mixed with 33.3 mL of extract (2:1), and 33.3 mL of 0.25M of cobalt nitrate solution was mixed with 66.7 mL of extract (1:2) in Erlenmeyer flask. Then the three samples were allowed to be stirred for about three and half an hour by placing on a magnetic stirrer individually. After stirring time completion, pH of the solutions was checked using a pH meter and then after, a small amount of 1 M NaOH solution was added to reach a pH of 12 as pH control and as a precipitating agent. Then after, the formed suspensions were placed within a refrigerator for overnight. The suspensions were centrifuged for about a minimum of three times followed by washing with DH_2O and absolute ethanol within each step for each sample. After that, the samples were dried using sample drying oven. The dried samples were calcined at 450℃ for three hours using furnace. The samples were grind into powder and ready for various characterization techniques followed by applications. Figure 7, depicts the schematic synthesis procedure of Co_3O_4 NPs in the presence of peel waste extract of ST as too green alternative template to control the over growth of the NPs (Magdalane *et al*., 2019).

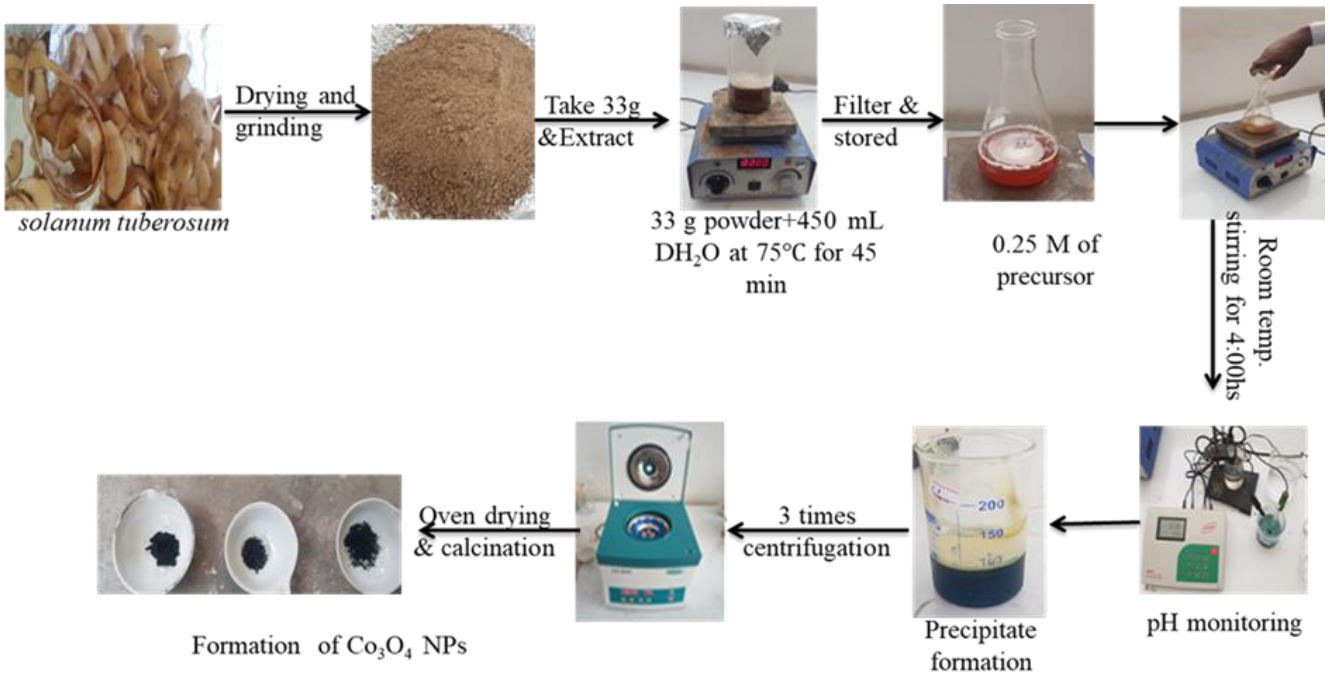

Figure 7: Diagrammatical biogenic syntheses of Co_3O_4 NPs.

3.5 Characterization Techniques

Thermal stability analysis study was done using a simultaneous TGA-DAT (DTG-60H, SHIMADZU Corporation, Japan). The crystal structure, average crystalline size, and phase stability of synthesized ZnO NPs, Co_3O_4 NPs, TiO_2 NPs, ZnO/CuO NCs and TiO_2/rGO NCs were analyzed by using XRD (XRD-7000, SHIMADZU Corporation, Japan) equipped with a Cu target for generating a Cu Kα radiation with λ = 0.15406 nm and recorded in the range from 10-80°. The morphological structure of each type of synthesized NPs and NCs were investigated using SEM (SEM-EDX-EVO 18 model with low vacuum facility and ALTO 1000 Cryo attachment). For further analysis and insights, the synthesized NPs and NCs were characterized using TEM, HRTEM, and SAED techniques (JEOL JEM 2100 HRTEM). The optical properties were studied using UV-DRS (OPTIMA UV-Vis spectrometer SP-3000 Plus, SHIMADZU Corporation, Japan). Functional group analysis was studied using FTIR (FT/IR-6600 type A, Jasco Company, Japan) characterization techniques. The Photocatalytic degradation studies of the synthesized nanocatalysts were carried out within 125 mL of Pyrex flask type reactor under 150W halogen lamp irradiation. The degradation analysis was followed and recorded using Double Beam UV-Visible spectrophotometer (SM-1600 spectrometer MAALAB, India).

3.6. Method of Photocatalysis using ZnO/CuO and TiO_2/rGO Nanocatalysts

The photocatalytic activities of the synthesized ZnO/CuO and TiO_2/rGO green nanocatalysts were evaluated by the degradation of an aqueous solution of different concentration of MB under visible light

irradiation. The reactions were carried out in a discontinuous mechanical stirring photoreactor with 400 W Osram lamps. The lamp was placed inside a quartz container with two cabins: one contained the lamp and the other makes water to pass into a recirculation channel for temperature control. Before irradiation, 35 mg of catalyst from each type were added to the stock dye solution (20 ppm of 220 mL) individually and sonicated in the dark for 30 min to maintain the adsorption-desorption equilibrium. Afterwards, the visible lamp was switched on, and the aliquots of the aqueous suspension were collected from the reactor every 15 min and then centrifuged to remove the suspended green catalyst particles. The concentrations of MB were determined using absorbance data obtained from UV-Visible spectrophotometer at around 664 nm (Cahino *et al.*, 2019). Figure 8 displays the photocatalytic degradation of MB dye in the presence of ZnO/CuO NCs green catalyst. At the end, the percentages of photocatalytic degradation efficiencies of the green fabricated nanocatalysts were calculated using equation (1).

$$\text{Degradation (\%)} = \left(\frac{A_0 - A_t}{A_0}\right) * 100 \qquad (1)$$

Where, A_0 is the initial absorbance of dye solution, and A_t is the dye solution absorbance at a certain reaction time.

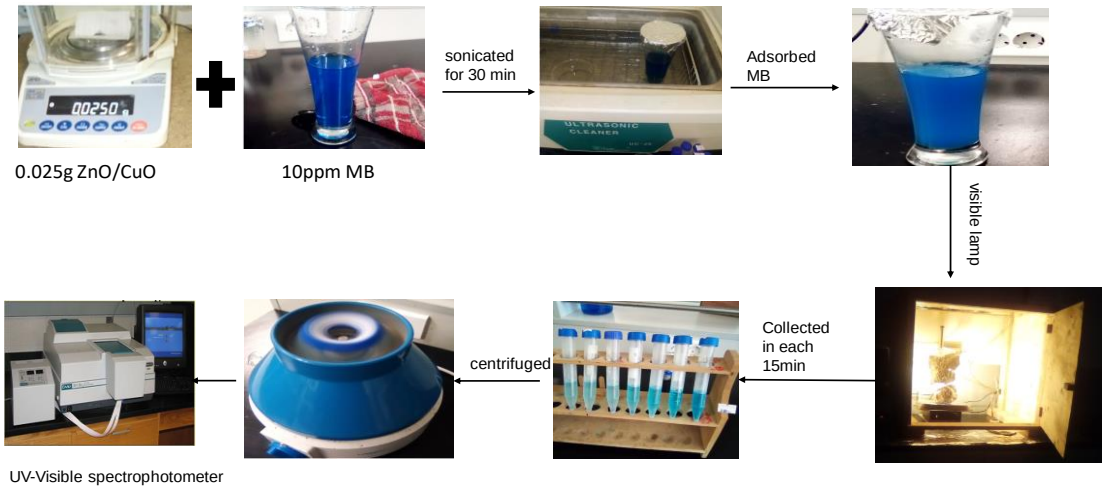

Figure 8: Photocatalytic degradation of MB in the presence of ZnO/CuO NC green catalyst.

In the same manner, the degradation study of MB using green synthesized TiO_2 and TiO_2/rGO catalysts were studied following the same protocol. Under here, the various parameters such as catalyst dosage, effect of pH and initial dye concentration, which can affect the degradation of MB dye under visible light irradiation, were studied.

3.7. Method of Antimicrobial

3.7.1. Method of Antibacteria using ZnO/CuO and Co_3O_4 Nanomaterials

The antibacterial performance of green synthesized ZnO/CuO NCs and Co_3O_4 NPs was investigated against *K. pneumoniae, E.Coli, S. Typhi, B. Subtilis and S.Aureus* strains *via* disc diffusion method. Initially 1.5 g nutrient broth agar was prepared in 100 mL distilled water and then after, it was subjected to sterilization. The prepared cultures were inoculated in nutrient broth and were kept on a rotary shaker at 35 ℃ ±2 ℃ for 24 hrs at 160 rpm. Ampicillin and DMSO were used as positive control/standard and solvent, respectively. Then, the nutrient agar was prepared within 100 mL distilled water using 6 g nutrient agar and 0.8 g agar-agar followed by well shaking till it became uniformly homogenized. The plates were then inoculated by dipping a sterile cotton wool swab into the resulting suspension followed by complete drying. Then, the plates were incubated at 37 ℃ for about 24 hrs and then were checked for the zone of inhibition (Bekele *et al*. 2020; Hafeez *et al*. 2020).

3.7.2. Method of Antifungal using ZnO/CuO and Co_3O_4 Nanomaterials

The antifungal activities of biogenic synthesized ZnO/CuO (10, 15, and 20%) NCs and Co_3O_4 (1:2, 1:1, and 2:1) NPs performed against *Fusarium oxysporum* and *Alternaria solani* fungi pathogens via food poising method using 10 mg/mL from each of the prepared nanomaterials in the presence of mock as a standard/control. The methods were used from previously developed protocol by Melkassa Plant protection team (Gabrekiristos, 2020). The pepper sample was collected from Mareko fana Dugda district and designated as 4DGK, while tomato sample was collected from Wash Melkasa research center, Ethiopia. The pathogens were cultured in potato dextrose broth at room temperature. The cultured pathogens were then placed on an orbital shaking incubator at 200 rpm. 100 µL from the prepared aliquot culture was taken into the potato dextrose agar on the PDA plate using sterile cotton swab. After that, each of the PDA plates was allowed to stand for 10 min to allow for culture absorption process. Then, 5 mm size wells were punched into the agar with help of sterile gel puncher. Aliquots of ZnO/CuO NCs and Co_3O_4 NPs and Mock as positive control were poured into wells on all plates using a micropipette. The PDA plates, which consist of each of the ZnO/CuO NCs of Co_3O_4 NPs with the corresponding fungal species was then incubated in the upside-down position at room temperature for about 10 and 18 days for *Fusarium oxysporum* and *Alternaria solani*, respectively. After incubation period, the mycelia growth of inhibition in terms of cm was measured (Jamdagni *et al*. 2018; Dananjaya *et al*. 2018).

4. Results and Discussion

4. 1. Characterization of TiO_2 and TiO_2/rGO NCs

4.1.1. TGA/DTA Analysis of TiO_2 NPs

Thermo gravimetric and differential thermal analysis was performed as a function of temperature as it can be shown in Figure 9. Figures 9a and 9b show the TGA/DTA of TiO_2 synthesized using peel extract of CS and musa acuminate of a 1:1 volume ratio, respectively. As presented in Figures 9a and 9b, weight losses were observed in three stages for the TiO_2 NPs synthesized using both peel extracts.

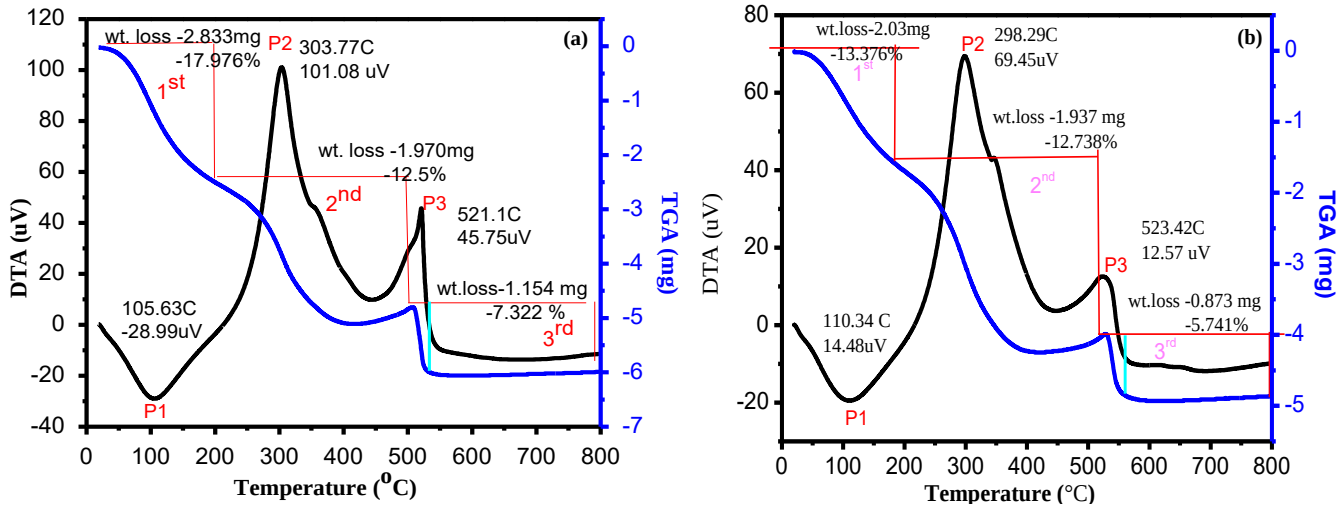

Figure 9: TGA/DTA curves of (a) CS and (b) MA mediated synthesis of TiO_2 NPs.

The first stage weight loss observed between 40-194℃ which were attributed to the removal of physically and chemically entrapped water and other moisture content from the surface of the synthesized TiO_2 NPs. The second stage weight loss observed in the range of 195-503℃ which could be attributed to the losses of organic residues and organic molecules/compounds as a result of combustion and carbonization of biomass materials from the synthesized TiO_2 NPs. Furthermore, no considerable weight loss was observed above 510℃ which proved that the synthesized TiO_2 NPs using CS (Figure 9a) and MA (Figure 9b) peel waste extract was found to be nearly pure and thermally stable and hence temperature of 450°C was selected as a calcination temperature (Bekele *et al*., 2021).

4.1.2. XRD Analysis of TiO_2/rGO NCs

Figure 10 depicts the XRD patterns of TiO_2 NPs and TiO_2/rGO NCs synthesized using various volume ratios of CS and MA. As observed from Figures 10a and 10b, TiO_2-0.5c, TiO_2-1c, TiO_2-1.5c, TiO_2-0.5m, TiO_2-1m and TiO_2-1.5m showed diffraction peaks at $2\theta \approx 25.3°$, 38.4°, 48.55°, 55.55°, 62.66°, 69.77° and

75.29° indexed to the crystalline planes of (101), (004), (200), (105), (204), (116) and (215), respectively. This corresponds to the standard pattern of the anatase crystalline phase form of TiO_2 NPs with JCPDS card number of 21-1272 with tetragonal structure. The absence of any foreign materials and secondary phases is an indication of the high purity and stability of the NPs and NCs synthesized using fruit peel waste extracts. Among the various volume ratios of TiO_2 NPs, TiO_2-0.5c and TiO_2-0.5m NPs showed less crystalline nature as compared to the other volume ratios due to the large amount of the peel extracts used which is in good agreement with previous reports. The average crystalline size of the synthesized NPs from various volume ratios were calculated using the Debye Scherer's equation (Tilahun Bekele *et al*., 2021) and were found to be 27, 12, and 7 nm for the TiO_2-0.5c, TiO_2-1c and TiO_2-2c and 22.4, 16.3 and 13.4 nm for TiO_2-0.5m, TiO_2-1m and TiO_2-2m, respectively.

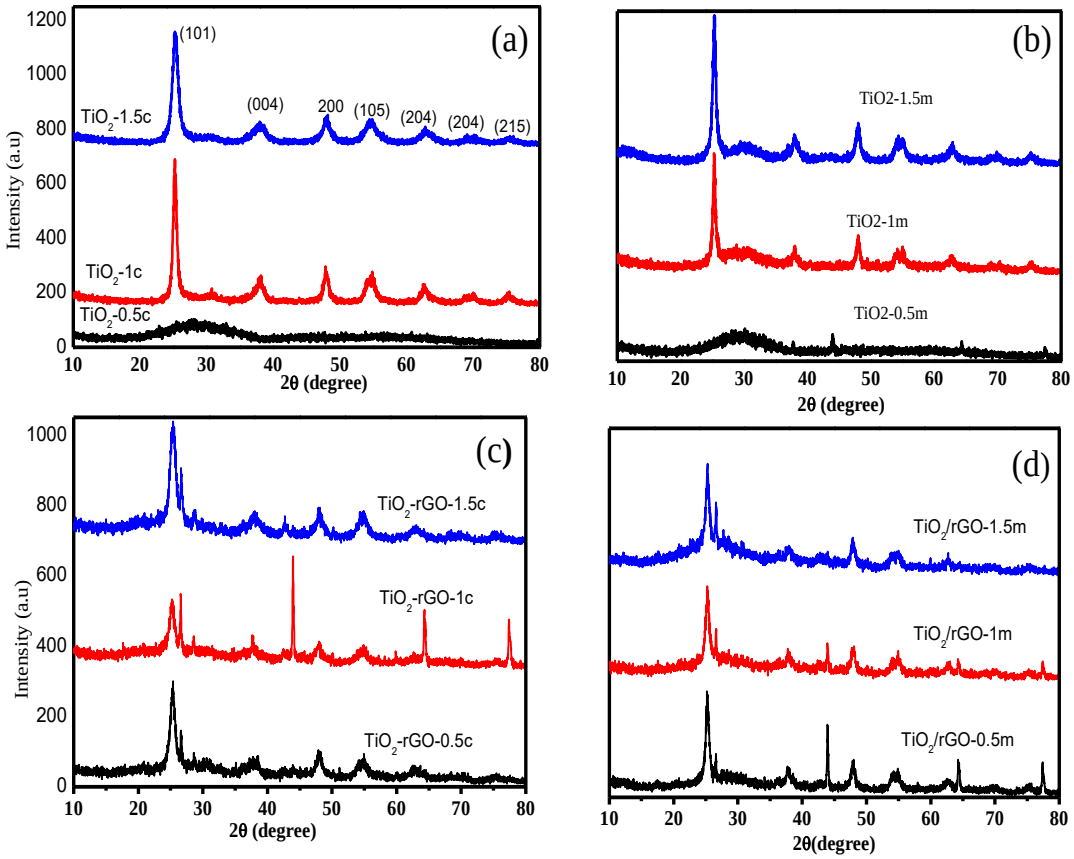

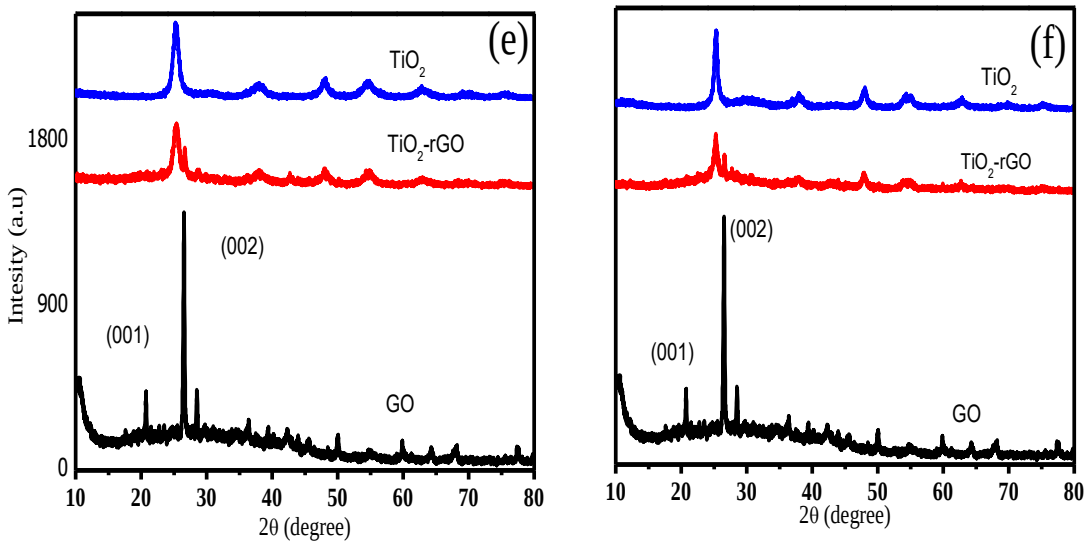

Figure 10: XRD spectra of (a) CS -TiO_2 NPs, (b) MA-TiO_2 NPs, (c) CS -TiO_2/rGO NCs, (d) MA-TiO_2/rGO NCs, (e) TiO_2 NPs, rGO-c and TiO_2/rGO- CS NCs and (f) TiO_2 NPs, rGO-m and TiO_2/rGO- MA NCs.

Figures 10c and 10d provide the XRD pattern of CS and MA peel extract synthesis of TiO_2-1c, TiO_2/rGO-1c, GO, TiO_2-1m,GO and TiO_2/rGO-1m, respectively. It was found that the synthesized TiO_2-rGO NCs possess a diffraction pattern similar to that of a single TiO_2 NPs. Due to the small quantity and low intensity of rGO, there was no separate peak for the rGO within the TiO_2-rGO NCs. Previously, similar results were reported for the TiO_2-activated carbon NCs(Xing *et al*., 2016). In addition to this, in both of the peel waste extracted mediated synthesis, the low peak intensity was due to the incomplete oxidation of graphite oxide and the cluster of bioactive constituents of the peel waste extract of CS and MA added during the synthesis process (Khannam *et al*., 2016). Figures 10e and 10f present CS and MA mediated synthesized TiO_2, TiO_2-rGO and GO. The resulted diffraction pattern of GO showed a broad and relatively strong characteristic peak at $2\theta \approx 10.1°$, which corresponding to the (001) plane and this indicates the formation of GO sheets. The calculated average crystalline size of GO mediated CS and MA was found to be 9.8 and 9.5 nm, respectively. The spacing between GO sheets was attributed due to the presence of oxygen functional groups such as hydroxyl, carboxyl and epoxide groups on the carbon backbones as supported by the previously reported work *(*Ali *et al*., 2018). In both of the peel waste extracted mediated synthesized GO sheet, an incomplete oxidation of graphite powder was exhibiting a strong and sharp diffraction peak at 26.1°, which in turn is corresponding to the (002) plane (Chong *et al*., 2015).

4.1.3. SEM-EDS Analysis of TiO_2/rGO NCs

Figures 11a and 11b clearly depict that the obtained rGO shows a wrinkled and crumpled morphology which is stacked together and form a typical multi-layer structure. This multi-layer structure of rGO is

important in providing additional rough surface for the deposition of CS and MA templated synthesized TiO_2 NPs into rGO (Farooq *et al.*, 2020). Figures 11(c-e) and 11(f-h) show the SEM images of TiO_2-0.5c, TiO_2-1c, TiO_2-2c, TiO_2-0.5m, TiO_2-1m and TiO_2-2m NPs, respectively, and the images were found to possess spherical shaped surface morphology in the presence of distinct edges having wide rough surface. In both of the peel waste extract mediated synthesized TiO_2 NPs using different volume ratios, the particle size was found to be increased with an increase in the amount of the peel waste extracts, which is in agreement with calculated average crystalline size from the XRD analysis. Furthermore, homogenized and small particle size TiO_2 NPs was obtained while using peel extract of CS due to its rich in biomolecules.

Moreover, Figures 11(i-k) and 11(l-n) show the corresponding SEM images of TiO_2/rGO-0.5c, TiO_2/rGO-1c, TiO_2/rGO-1.5c, TiO_2/rGO-0.5m, TiO_2/rGO-1m and TiO_2/rGO-1.5m NCs, respectively. As can be observed from Figures 11a and 11b, the rGO shows the wrinkled and crumpled morphology, while the CS and MA based synthesized NCs showed cross-linked TiO_2 NPs on the surface of the rGO sheet that formed the network structures within the rGO/TiO_2 NCs. It has been found that as the amount of rGO content is small, images of reduced graphene oxide-modified TiO_2 NCs does not show a clear-cut presence of rGO flakes, rather it shows the uniform distribution of TiO_2 NPs. The uniform distribution of TiO_2 NPs is due to very small amount of rGO with respect to TiO_2 NPs and intercalation of rGO inside the TiO_2 NPs matrix (Y. C. Cao *et al.*, 2015). However, as the content of rGO is increased from 30-90 mg, the size becomes clearly visible and this provides more surfaces for the deposition of green synthesized TiO_2 NPs, which intern is necessary for the photocatalytic degradation of MB dye (Amir Faiz *et a*l., 2020).

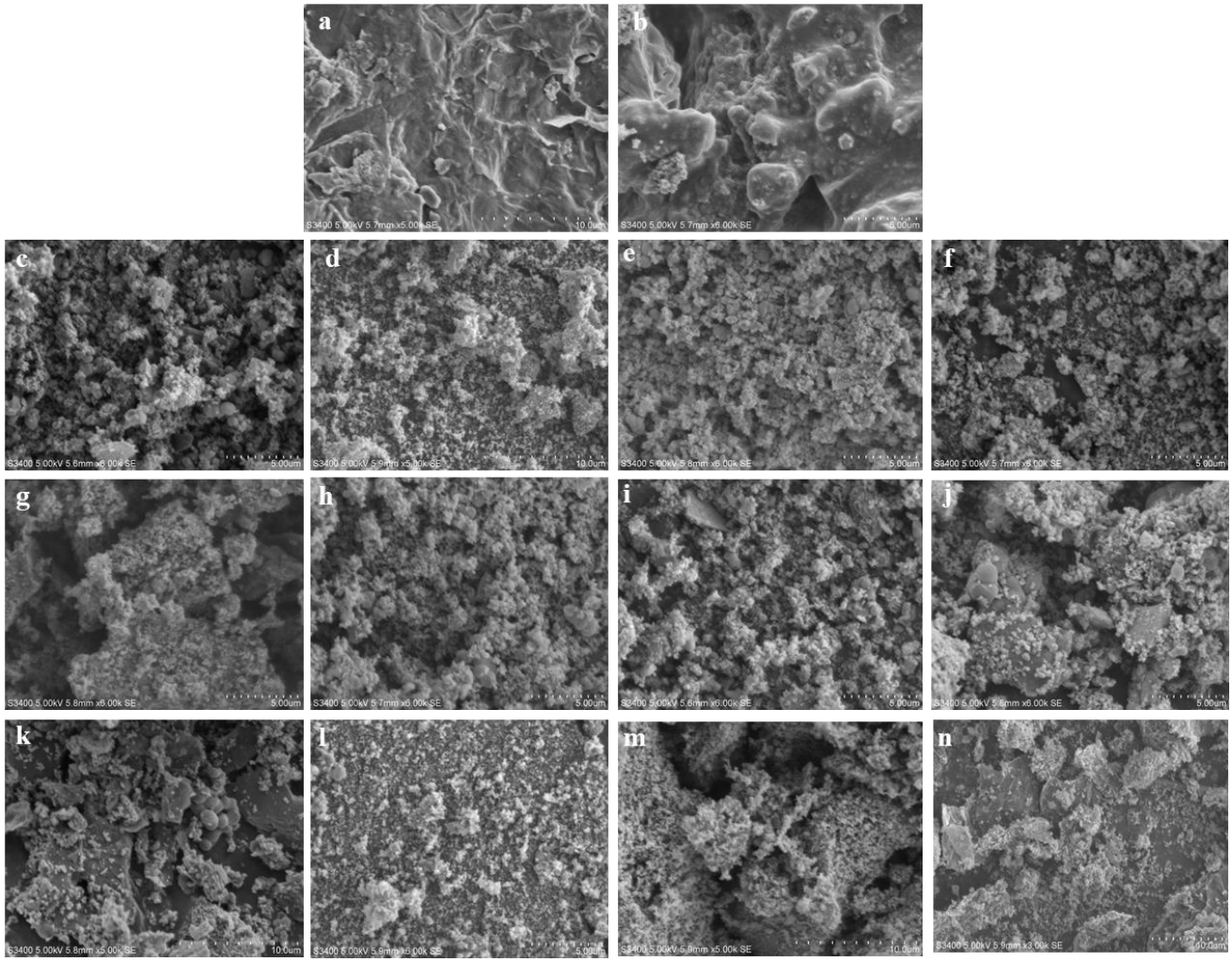

Figure 11: SEM micrograph of green synthesized rGO/ CS peel (a), rGO/ MA peel (b),TiO_2-0.5c (c), TiO_2-1c (d), TiO_2-1.5c (e), TiO_2-0.5m (f), TiO_2-1m (g),TiO_2-1.5m (h),TiO_2/rGO-0.5(i), TiO_2/rGO-1c (j), TiO_2/rGO-1.5c (k), TiO_2/rGO-0.5M (l), TiO_2/rGO-1M (m) and TiO_2/rGO-1.5M (n).

The differences in the photocatalytic performance of those various compositions of TiO_2/rGO NCs obtained in the presence of peel waste extracts of CS and MA could be attributed to the amount of rGO to TiO_2 composition ratio, in addition to the differences in the morphological structure. Moreover, Figures 12a-d depicts the corresponding EDS spectra of TiO_2/CS and TiO_2/MA NPs, TiO_2/rGO/CS and TiO_2/rGO/MA NCs, respectively. As can be presented in Figures 13a and b, the dominant and major peaks are Ti and O. The presence of minor peaks such as Na, K, Si and Ca might be attributed from fruit waste extracts. Moreover, the foreign peaks might also introduce during the preparation of samples using silica ceramic dishes for SEM-EDS characterization (Kusiak-Nejman & Morawski, 2019). Figure 12c and d presents the EDS spectra of TiO_2/rGO/CS and TiO_2/rGO/MA NCs, respectively. In both of the Figures, in addition to the presence of Ti and O, presence of C confirms the presence of reduced graphene.

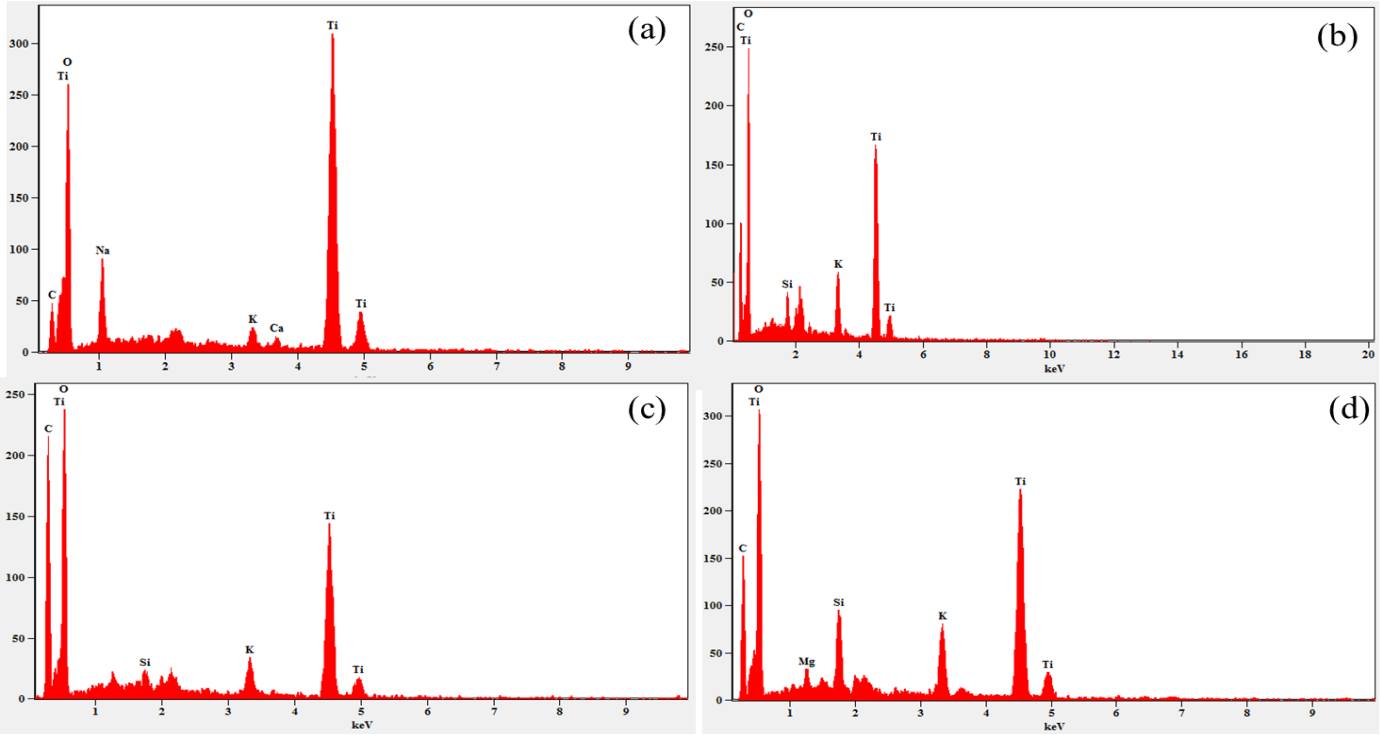

Figure 12: EDS spectra of (a) TiO_2/CS NPs, (b) TiO_2/MA NPs, (c) TiO_2/rGO/CS NCs and TiO_2/rGO/MA NCs.

4.1.4. TEM-HRTEM and SAED Analysis of TiO_2/rGO NCs

Figures 13(a-d) show TEM micrographs of CS mediated obtained TiO_2NPs (a) and TiO_2/rGO (b) and MA peel waste obtained TiO_2 NPs (c) and TiO_2/rGO NCs (d). The TEM images of these peels waste extracted mediated synthesized TiO_2 NPs using various volume ratios reveals that the NPs were found to have good crystalline nature without aggregations and agglomerations. This is in agreement with the XRD results and intern confirms the formation of pure TiO_2 NPs. The absence of aggregations and agglomerations were achieved due to the presence of bioactive capping and reducing agents from the peel waste extract of CS and MA. Furthermore, it can be observed from Figures 13c and 13d that rGO is found to be covered with the green synthesized spherical anatase TiO_2 NPs. The presented Figures also showed crumpled, hexagonal, and rhombic like large surface morphological structure due to the presence of the high surface area of the rGO sheets. It is also observed that the surface of rGO sheets was found to be packed densely with the green obtained TiO_2 NPs which showed good combination of rGO sheets and TiO_2 NPs and efficient TiO_2 NPs loading on the surface sheet of rGO (Joshi *et al*. 2020; Ramos *et al*. 2020). The corresponding HRTEM images in Figures (13e-h) clearly showed that the lattice fringes of the rGO were parallel to the edges of the anatase TiO_2 NPs. The lattice fringes also clearly indicate that the particles are nanocrystalline with an anatase phase form as it is also confirmed from the XRD data.

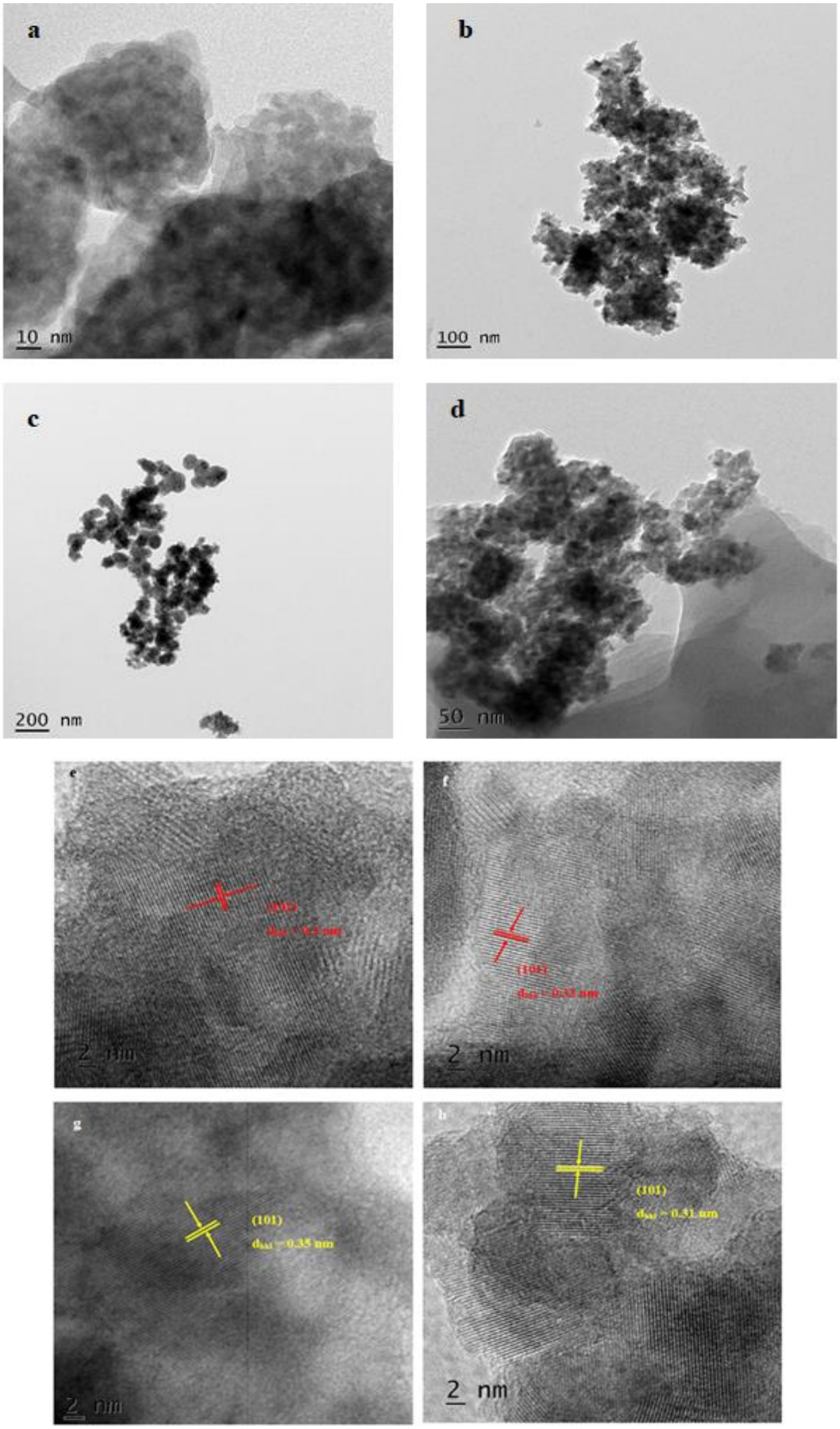
a
10 nm
b
100 nm
c
200 nm
d
50 nm
e
2 nm
f
(101)
2 nm
g
(101)
2 nm
h
(101)
2 nm

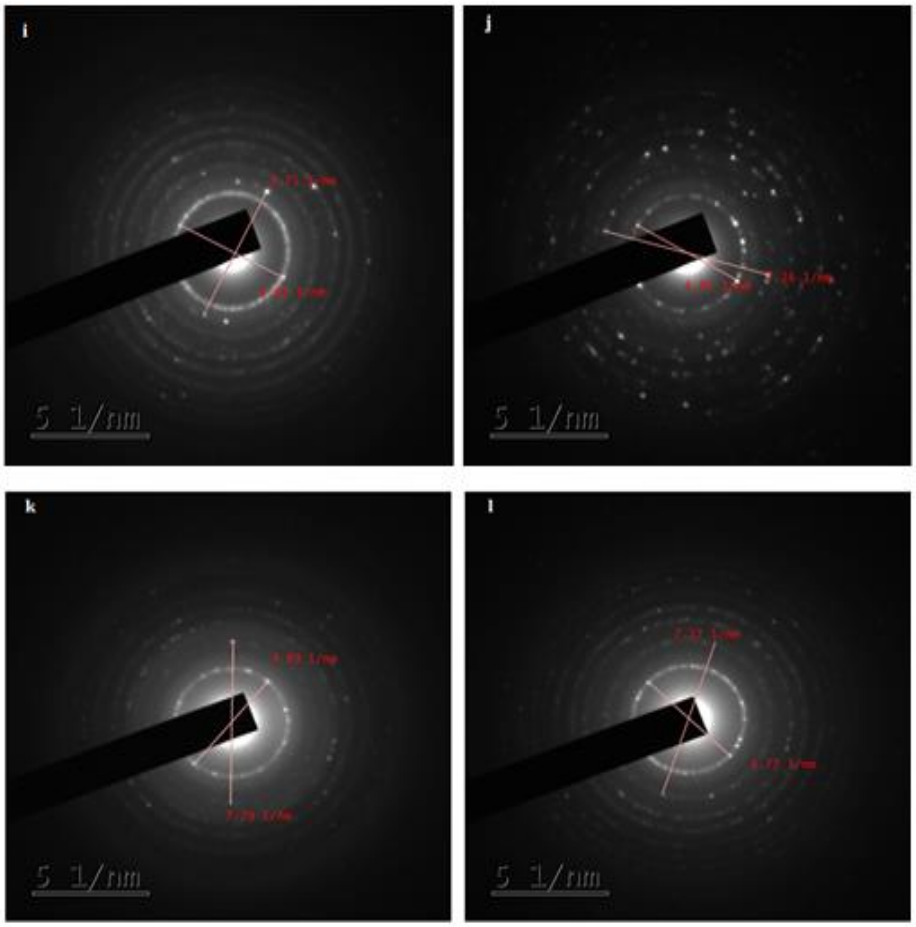

Figure 13: TEM image of TiO_2/CS NPs (a), TiO_2/rGO/CS NCs (b), TiO_2 MA NPs (c) and TiO_2/rGO/MA NCs (d). HRTEM image of TiO_2/MA (e), TiO_2/CS (f), TiO_2/rGO/ MA NCs (g), TiO_2/rGO/ CS NCs (h). SAED pattern of TiO_2/CS (i), TiO_2/MA (j), TiO_2/rGO/MA NCs (k), TiO_2/rGO/CS NCs (l).

The Figures indicated that the reduced graphene particles were well doped in the presence of the peel waste extracts with a dense layer of TiO_2 NCs having d-spacing value of 0.3, 0.33, 0.35 and 0.31 nm for the TiO_2/MA (e), TiO_2/CS (f), TiO_2/rGO/ MA NCs (g) and TiO_2/rGO/CS NCs, respectively, corresponding to the d_{101} of TiO_2 anatase structured NPs. The slight variation in the d-spacing value of TiO_2 NPs and TiO_2/rGO NCs may results from the presence of different bioactive molecules of the MA and CS. Moreover, Figures 13(i-l) presents SAED pattern of the green synthesized TiO_2 NPs and TiO_2/rGO NCs obtained in the presence of the peel waste extract of CS and MA. Figures 13(i-j) showed the SAED of TiO_2 NPs and the resulting SAED pattern proves the presence of clear ring diffraction patterns and does not indicate the presence of any dislocations in the lattice planes, which confirms that the prepared TiO_2 NPs have high crystallinity nature. The clear white circular spots around the center of SAED pattern confirm (101), (004), (200), (105), (211), (204), (220), and (215) miller indices as also supported by the XRD analysis assuring anatase lattice planes of biosynthesized TiO_2 NPs. Similarly, Figures 13k and 13l indicate

the SAED analysis of the TiO_2/rGO/MA and TiO_2/rGO/*CS* NCs, respectively, and similar pattern was observed as in the case of the single green synthesized TiO_2 NPs (Siddeeg 2020; Heo *et al*. 2019).

4.1.5. Band Gap Energy Analysis of TiO_2/rGO NCs

Figures 14 (a-f) shows the tauc plot of absorption spectra of TiO_2 NPs prepared using different volume ratios of titanium precursor salt and peel waste extract of CS (a-c) and MA (d-f). The optical band gap energy for each of the volume ratio of TiO_2 NPs was calculated using tauc plot method. The band gap energy (E_g) were found to be 3.17, 3.28, 3.29, 3.10, 3.33 and 3.38 eV for the TiO_2-0.5c, TiO_2-1c, TiO_2-2c, TiO_2-0.5m, TiO_2-1m and TiO_2-2m, respectively. This is again found to be in cloth agreement with the work reported by (AlShammari *et al*., 2020). As presented in Figure 14, it was found that increasing rGO concentrations in the composite tends to decrease energy band gap in each of the peel waste extract mediated synthesized TiO_2/rGO. In addition to this, it is noted that the presence of rGO influences light absorption properties of the composite significantly showing increase in light absorption intensity in the UV region and a red shift in the absorption edge around 400 nm as supported by the previous report. Furthermore, the TiO_2/rGO NCs show a red shift in the absorption edge compared to single TiO_2 NPs. Similar phenomenon related to the present study was also reported by (Zhang *et al*., 2010).

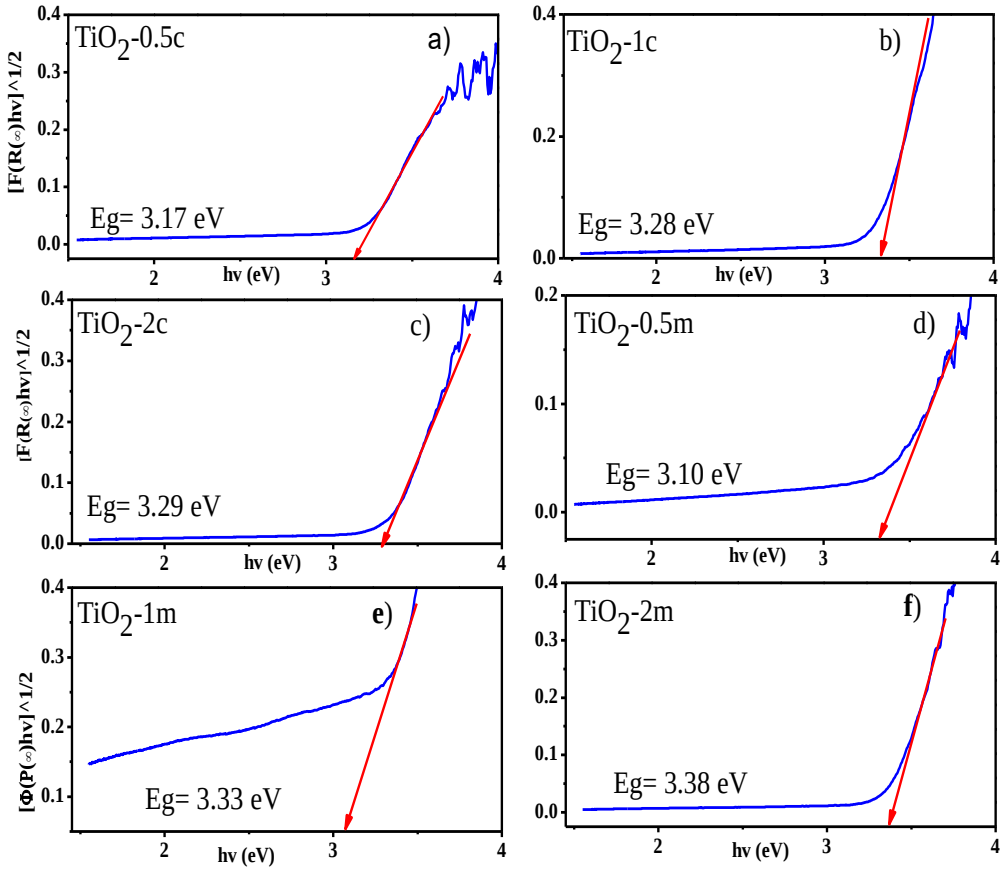

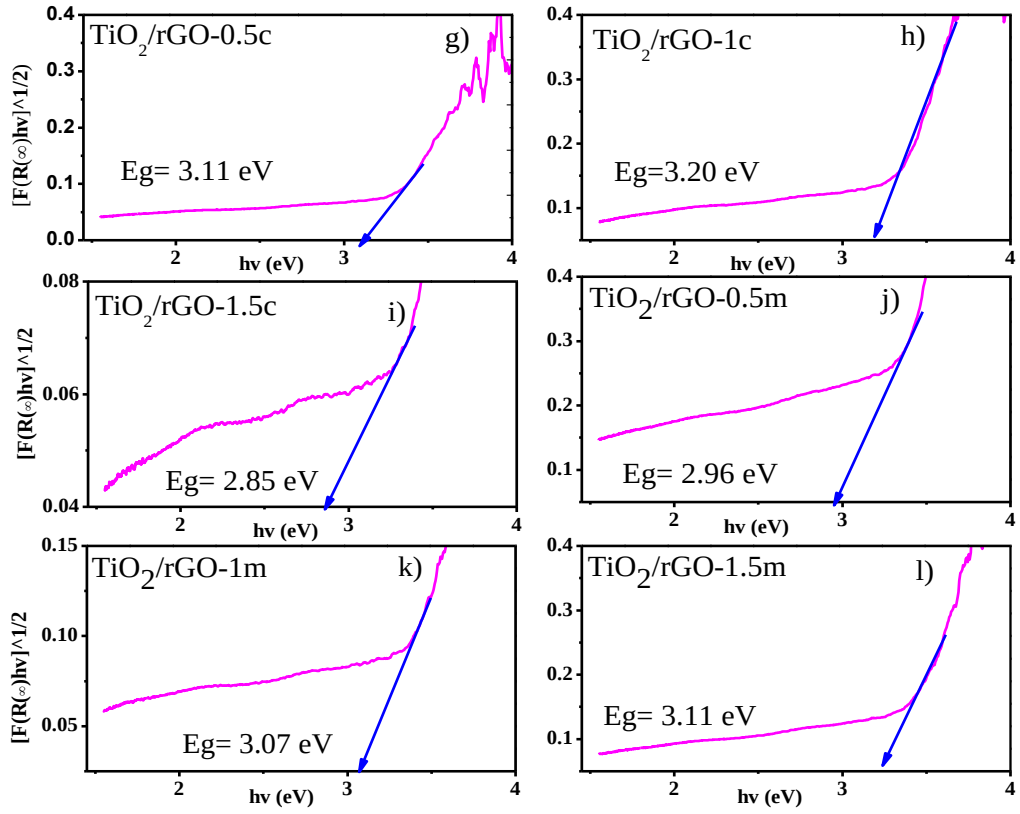

Figure 14: Tauc plots of TiO_2 NPs and TiO_2/rGO NCs obtained using CS and MA peel waste extract.

4.1.6. FTIR Analysis of TiO_2/rGO NCs

As depicted in Figure 15a, the peel extract of CS shows various absorption bands, stretching, and bending mode of vibration located at around 3447.81, 2920.53, 2327.68, 1637.89, 1449.65 and 1076.51 cm^{-1} and similarly MA peel waste powder shows various absorption peeks located at 3433.64, 2920.50, 2324.60, 1639.52, 1405.71, 1090.65 cm^{-1}. In both case of the peel waste extract, the broad band at 3447.81 and 3433.64 cm^{-1} is assigned to hydrogen bonded-OH stretching mode of vibration (Kong et al., 2016). The bands centered at around 2920.53 and 2920.50 cm^{-1} represents H-C-H, C-H bond stretching of alkanes, and -C-H groups associated by H-bond. The week band observed at 1639.52 and 1641.73 cm^{-1} is attributed to the amide group vibration, which could be a characteristic peak of both proteins and enzymes present in both of the peel extracts (AlShammari et al., 2020). Figures 15a and 15b also show stretching vibrations located at 1405.71 and 1449.65 cm^{1} for the CS and MA peel extract, respectively, which indicates the binding of proteins on the surface of TiO_2 NPs and thereby contributes to the stabilization of green TiO_2 NPs. The bands observed at around 1090.65 and 1076.55 cm^{-1} for CS and MA, respectively indicates the presence of C-O and aliphatic amines (L. Li *et al.*, 2016). Figure 15a and 15b also show the corresponding FTIR spectra of GO and rGO. GO displayed numerous typical absorption bands corresponds to oxygen

functionalities present on GO sheet. The band at 1725 cm^{-1} is credited to the C = O and the wide band around 3000-3600 cm^{-1} is ascribed to the O-H (hydroxyl) stretching vibrations of the C-OH groups due to moisture absorbed onto the surface of prepared sample. The band corresponds to 1056 cm^{-1} and 1248 cm^{-1} are credited to C-O (carboxylates) and C-O-C (epoxide) stretching modes, respectively. The sp^2 hybridized carbon (C = C) skeleton vibration peak could be seen in GO around 1633 cm^{-1} (León et al., 2017).

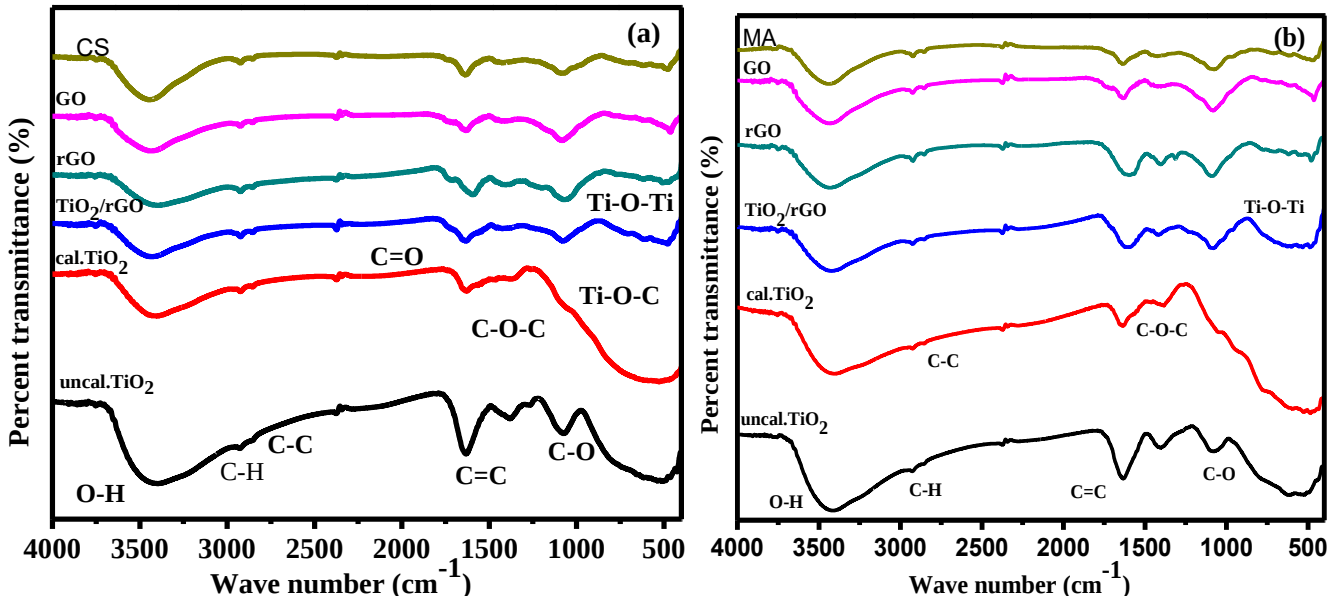

Figure 15: FTIR spectra of (a) CS, templated synthesized GO, rGO, TiO_2 and TiO_2/rGO and (b) MA, MA templated synthesized GO, rGO, TiO_2 and TiO_2/rGO NCs.

Compared to GO, rGO shows significant reduction in absorption intensities due to the presence of oxygen containing functional groups like carboxylates, epoxide, and carbonyl compounds, indicating the green reduction of GO to rGO by both CS and MA peel waste extracts (Shimi et al., 2022). As can be presented in Figure 15a and 1b, the peaks centered at 2854.33 and 2921 76 cm^{-1} in the spectrum of rGO are due to the stretching vibration of H-C-H and -C-H groups of alkanes associated by H-bond as well. FT-IR spectra of TiO_2 showed the broad band around and below 1000 cm^{-1}, which indicates replicate Ti-O-Ti linkage within TiO_2 nano pours. Furthermore, the spectra of TiO_2/rGO exhibited low intensity band frequency compared to the CS and MA stabilized GO and rGO, which is formed by the amalgamation of (Ti-O-Ti) and (Ti-O-C) linkages; owing to the chemical interaction of TiO_2 with rGO sheets. This analysis confirms that the green reduction of GO and coupling with TiO_2 NPs on the green obtained rGO sheets. In addition to this, the CS and MA templated obtained TiO_2 NPs could be susceptible to the interactions with the functional groups of rGO in the formation of TiO_2/rGO NCs (León *et al.*, 2017).

4.2. Characterization of ZnO/CuO NCs

4.2.1. TGA/DTA Analysis of ZnO and CuO NPs

The thermo gravimetric analysis and differential thermal analysis (TGA/DTA) curves of the as-prepared ZnO NPs and CuO NPs are displayed in Figure 16. The TGA/DTA analysis was performed to determine thermal stability and weight percentages of the binded peel extract over the samples. Figure 16a shows the TGA/DTA curve for the ZnO NPs sample with three main stages of weight loss. The three endothermic peaks indicated by bend Ed_1, Ed_2 and Ed_3 in the DTA curve with a first weight loss of 5.76% at 80℃ and from 140-155℃ in the TGA curve can be associated to the removal of surface accumulated water molecules and the decomposition of chemically bound groups especially ethanol containing, respectively. The second weight loss (6.4%) in the range of 175-380℃, accompanied by one endothermic and one strong exothermic peak indicated by bend Ed_4 and Ex in the DTA curve, which might be attributed to the decomposition of organic compounds of the peel extract. Furthermore, the thermal stability of ZnO NPs was achieved after third mass loss of 0.134%, in between the temperatures of 380 and 450℃. These weight losses occurred due to the decomposition of the residual precursors and removal of gases such as CO_2 in air with formation of ZnO NPs. It has been found that, above 450℃ there was no any negligible weight loss from the synthesized NPs, indicating that the surface impurities were removed and the ZnO NPs are thermally stable. The analysis shows that, 450℃ calcination temperatures would be suitable for synthesizing ZnO NPs (Bayrami *et al*., 2018).

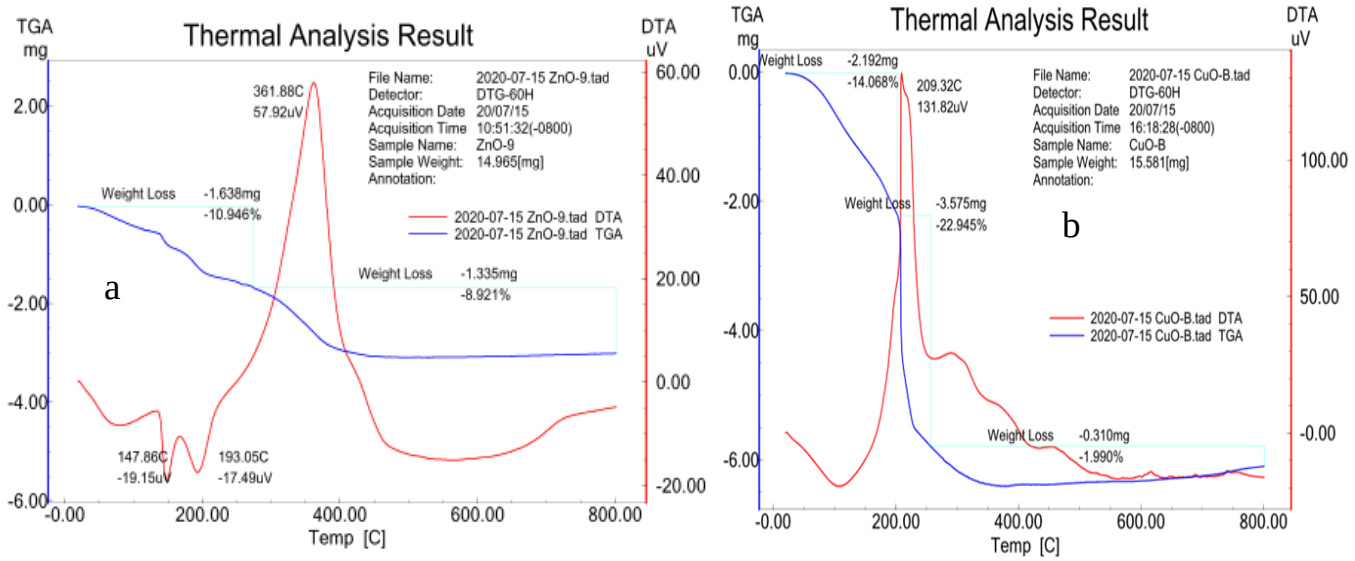

Figure 16: TGA-DTA curves of as-synthesized (a) ZnO and (b) CuO NPs synthesized in the presence of MA.

Furthermore, Figure 16b shows the TGA/DTA curve for CuO NPs. The first endothermic peak (Ed_1) between 80℃ and 100℃ in DTA curve (14% weight loss from TGA curve) could be associated with dehydration of water molecules from the prepared sample. In further heating of these samples between the temperature range of 200℃ and 350℃, the sample showed weight loss of 22.9% with strong exothermic and weak endothermic peaks (Ex and Ed2) as presented in the DTA curve. This could be associated with the decomposition of organic compounds from the peel extract attached to the surface of the CuO sample (Bayrami et al., 2018). Furthermore, thermal stability of CuO sample was obtained after mass loss of 1.9%, with weak endothermic peaks between the temperatures of 350℃ and 450℃. Moreover, this peak could ascribe to desorption and subsequent evaporation of some organic molecules belong to peel of MA. These weight losses can be attributed to the decomposition of Cu salt to form CuO NPs. In the same manner, based on the TGA/DTA analysis, 450℃ would be a satisfactory temperature for the precursor decomposition to acquire the CuO NPs, followed by synthesis of ZnO/CuO NCs in the presence of the peel extract of MA (Asemani and Anarjan 2019 ; Ananda Murthy *et al*. 2021).

4.2.2. XRD Analysis of ZnO/CuO NCs

The crystalline structure and phase purity of the synthesized ZnO NPs, CuO NPs, and ZnO/ZnO NCs were followed by characterization by XRD technique. Figure 17a depicts the XRD patterns of the green synthesized ZnO NPs within different precursor concentration and peel extract (1:1, 1:2, and 1:3). According to the XRD patterns, the synthesized ZnO NPs formed within the 1:1, 1:2, and 1:3 volume ratios showed the same pattern as standard ZnO with the same plane value. The diffraction peaks located at (100), (002), (101), (102), (110),(103), (100), (112) and (201) with its corresponding 2θ values of 31.83 ^{o}, 34.49 ^{o}, 36.32 ^{o}, 47.60 ^{o}, 56.67 ^{o}, 63.52 ^{o}, 67.60 ^{o}, 68.03 ^{o}, and 69.15^{o}, respectively which were found to be consistent with standard JCPDS of (00-036-1451) (Gawade *et al*., 2017). This indicates that the peaks are belongs to hexagonal wurtzite structure of ZnO and hence the green synthesized ZnO NPs within various volume ratio of the precursor salt and the peel waste extract were found to be highly pure. Since, no other peaks have been detected in the green synthesized sample, which proves the purity of ZnO NPs.

In addition to these, a sharp and narrow diffraction peak for each volume ratio of the green synthesized ZnO NPs were observed, which is due to the reduction of zinc ions by organic compound present in the peel extract of MA and stabilization of resultant NPs. Similar results were also reported by (Elumalai & Velmurugan, 2015), which indicates the ZnO NPs were well crystalline in structure. The calculated average crystalline size was estimated as 25, 28, and 28 nm for the 1:1, 1:2, and 1:3 ratios of ZnO NPs, respectively. It can be seen that the synthesized ZnO NPs with 0.27 M of precursor concentration has possess the smallest average crystallite size and therefore the precursor concentration 0.27 M (1:1) was

considered for further studies (for the synthesize of the ZnO/CuO NCs within various compositions in the presence of peel suspension). XRD pattern of pure ZnO (1:1) NPs, CuO NPs, and ZnO/CuO NCs are presented in Figure 17b. As discussed under Figure 17a, the XRD results of pure ZnO NPs demonstrate the hexagonal wurtzite structure. Similarly, XRD patterns of pure CuO are presented in Figure 17b. The peaks appeared at 2θ values of 32.55°, 35.57°, 38.77 °, 48.87 °, 53.50 °, 58.23 °, 61.59 °, 66.138 °, 68.02 °, 72.40 ° and 75.10 ° and well matched with the corresponding miller indices plane of (110), (002), (111), (202), (020), (202), (113), (311), (113), (311) and (004), respectively; which reveal the crystalline plane of CuO monoclinic phase with JCPDS of 0481548). In the case of ZnO/CuO NCs other than the peaks of hexagonal crystalline phase of ZnO, the reflection peaks of CuO were observed≈at 2θ values of 32.54, 35.57°, 38.7°, 48.84°, 53.48° and 58.16° which corresponds to the (110), (002), (111), (202), (020), and (202), respectively which reveal that the crystalline plane of CuO monoclinic phase (JCPDS CuO 048-1548) (Abraham *et al.*, 2018). There is no additional peak in the synthesized NCs, indicating that the composite consists of ZnO and CuO NPs without any external foreign materials and impurities.

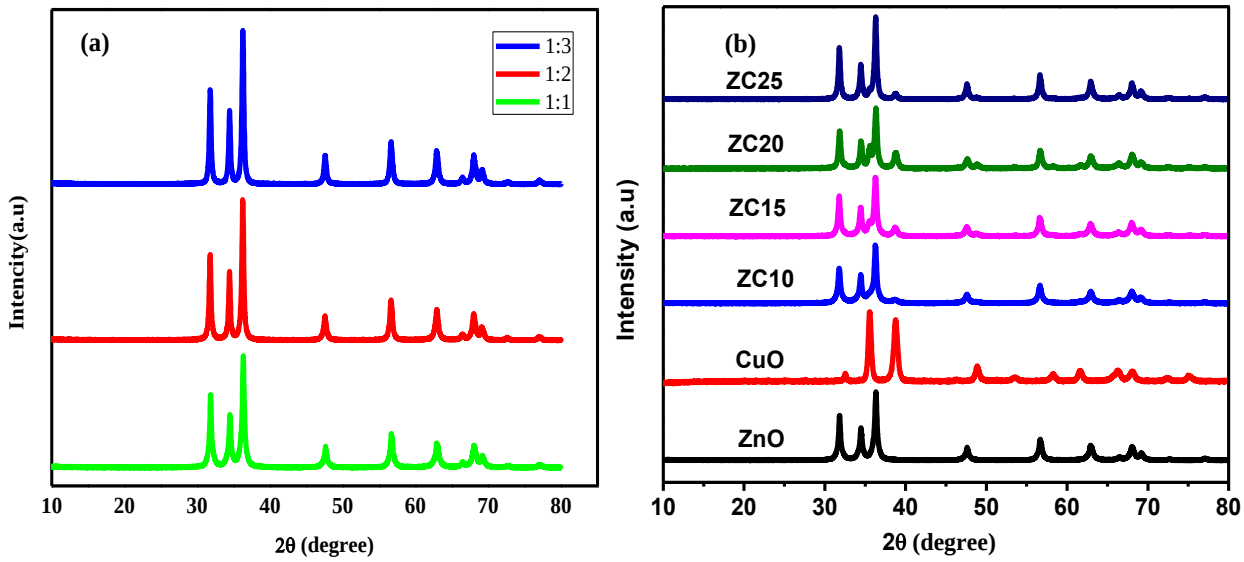

Figure 17: XRD spectra of synthesized (a) ZnO (1:1, 1:2, and1:3) NPs and (b) CuO NPs and ZnO/CuO (10%, 15%, 20% and 25%) NCs.

Furthermore, Figure 17b indicates that both ZnO and CuO NPs phases are present within the XRD graph of the NCs and the peaks do not affect each other, which confirms the formation of ZnO/CuO NCs. The ZC10, ZC15, ZC20 and ZC25 shows the XRD pattern of coupled ZnO/CuO NCs with different wt% of copper nitrate precursor. The addition of copper nitrate of 10 wt% (ZC10) showed the reflection peaks of CuO with low intensity, which is attributed to the low content of CuO in the NCs. However, with an increase in the copper content from 15% to 25%, CuO peaks within the ZnO/CuO NCs have been observed with increased intensity. Furthermore, minor shifts were observed in the 2θ values of ZnO/CuO NCs. The

shift from 31.84° to 31.76°, 34.49° to 34.41° and 36.32° to 36.23° were observed, which indicates that the typical peak of ZnO was changed within the ZnO/CuO NCs. The trivial shifts indicate that the modification of ZnO with CuO can affect the structure of ZnO (Y. Cao *et al*., 2021).

4.2.3. SEM-EDS Analysis of ZnO/CuO NCs

In order to asertain additional information about the green mediated synthesized ZnO NPs, CuO NPs, and their compoistes, morphological characterization was carried out using SEM techingue. Figures 18(a-c) represnt the SEM images of the synthesized ZnO NPs within 1:1, 1:2, 1:3, resepctively. The SEM image of the green obtained ZnO NPs showed clear crystals of spherical shape in which the particles are inclined together and polydispersed due to the presence of numerous bioactive molecules from the peel of MA that prevents the overgrowth followed by stabilization of the ZnO NPs (Tilahun et al., 2022). Among the three ratios of ZnO NPs, ZnO (1:1) NPs provides a more homogenized shape due to the well bi-association of molecules of MA peel with the Zn^{2+} cations during the synthesis process; and again, this prevents from the formation of aggregation. Moreover, even if the spherical shape is dominant in all of the ZnO NPs, road shaped structure is also observed, which fits with the previously reported work (Demissie *et al*., 2020). Figure 18 (d) displays the SEM image of the CuO NPs obtained via green synthesis in the presence of the peel extract of MA. The SEM image proves the presence of well polydispersed, spherical shaped distribution of CuO NPs with clear distribution of particles. In addition, the image shows the effect of biomolecules of the peel due to the existence of some aggregation/agglomeration. The agglomeration is actually formed due to the auto organization of small structures, which might be formed by self-assembling of CuO NPs (Ahamed *et al*. 2014; A. *et al*. 2021). The auto organization of structures and self-assembling of CuO NPs are viable as the extract of MA peel waste works as structure directing agent during the synthesis process. Figures 18 (a-h**)** represent the SEM image of the green synthesized ZnO (1:1, 1:2, and 1:3) NPs, CuO NPs, and ZnO/CuO (10%, 15%, 20% and 25%) NCs.

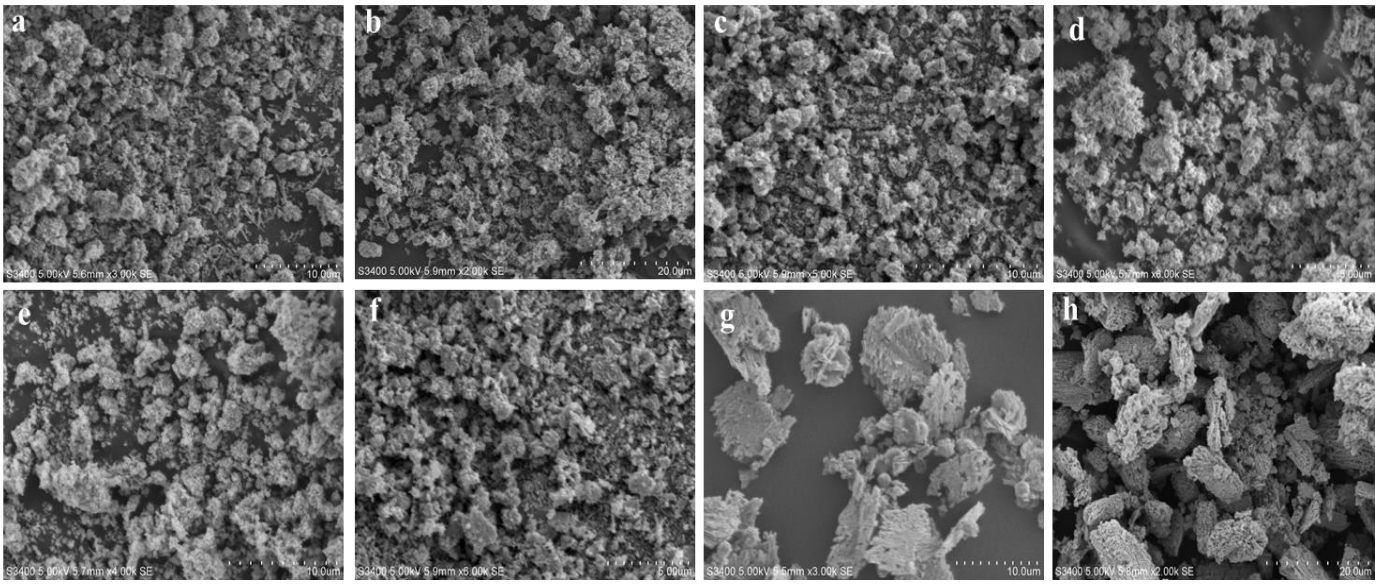

Figure 18: SEM image of ZnO NPs (1:1, 1:2, and 1:3) represented by (a, b, and c), respectively, CuO NPs (d), ZnO/CuO NCs (10%, 15%, 20% and 25%) represented by (e, f, g and h), respectively, which was synthesized in the presence of MA peel extract.

Again Figures 18 **(**e-h**)** showed the SEM image of ZnO/CuO NCs synthesized in the presence of peel extract of MA with various w/w% of CuO. Like that of the single biosynthesized ZnO and CuO NPs, the resulted NCs also possess spheroid and rice grains like morphology. Furthermore, the composites are found to be within the size range of nanometers, which are in concordance with the XRD analysis. The synthesized NCs showed low level of agglomeration because they didn't form a large cluster due to the existence of the suspension of the peel of MA extract (Ait Ahmed et al., 2019). Formation of agglomeration can usually be demonstrated by the formation of large cluster. However, it has been found that as the w/w% of CuO is increased, the particles size easily visible, which is again found to be in good agreement with the average crystalline size calculations and analysis too. It has been observed that as the w/w% of CuO is increased with the presence of the peel extract, the ZnO/CuO particles were agglomerated to form a sponge-like bunch of particles on the surface. This agglomeration could be induced by densification resulting in narrow space between particles and this could be also attributed by the narrow pores size of ZnO NPs (Ruan *et al*., 2020).

In order to ascertain further information on the biogenic synthesis of ZnO/CuO NCs, EDS analysis was carried out. Figures 19a-c represents the EDS spectra of ZnO NPs, CuO NPs, and ZnO/CuO NCs, respectively. The EDS analysis (Figure 19a) of the ZnO NPs indicates that our sample contains zinc, oxygen, and gold as essential elements. The EDX spectra displayed two robust peaks of zinc and oxygen, correspondingly typical for ZnO NPs. The high intensity of zinc and oxygen peaks shows that

the sample is completely ZnO NPs. Figure 19b displays the chemical composition result of green CuO NPs. The EDS studies of CuO NPs present three peaks in between 1 kV and 10 kV that are directly related to Cu in the tested material. The results indicate that the reaction product is composed of high purity CuO NPs which agrees with the result obtained from XRD. The EDS analysis also revealed the formation of nonstoichiometric CuO NPs with oxygen vacancy (Ruan *et al.*, 2020). Moreover, the EDS spectra of ZnO/CuO NCs are displayed in Figure 19c, which reveals that the green synthesized NCs are highly pure, without any secondary impurities. Furthermore, Figure 19c proved the presence of Zn, Cu and O which is an indication of formation of ZnO/CuO NCs.

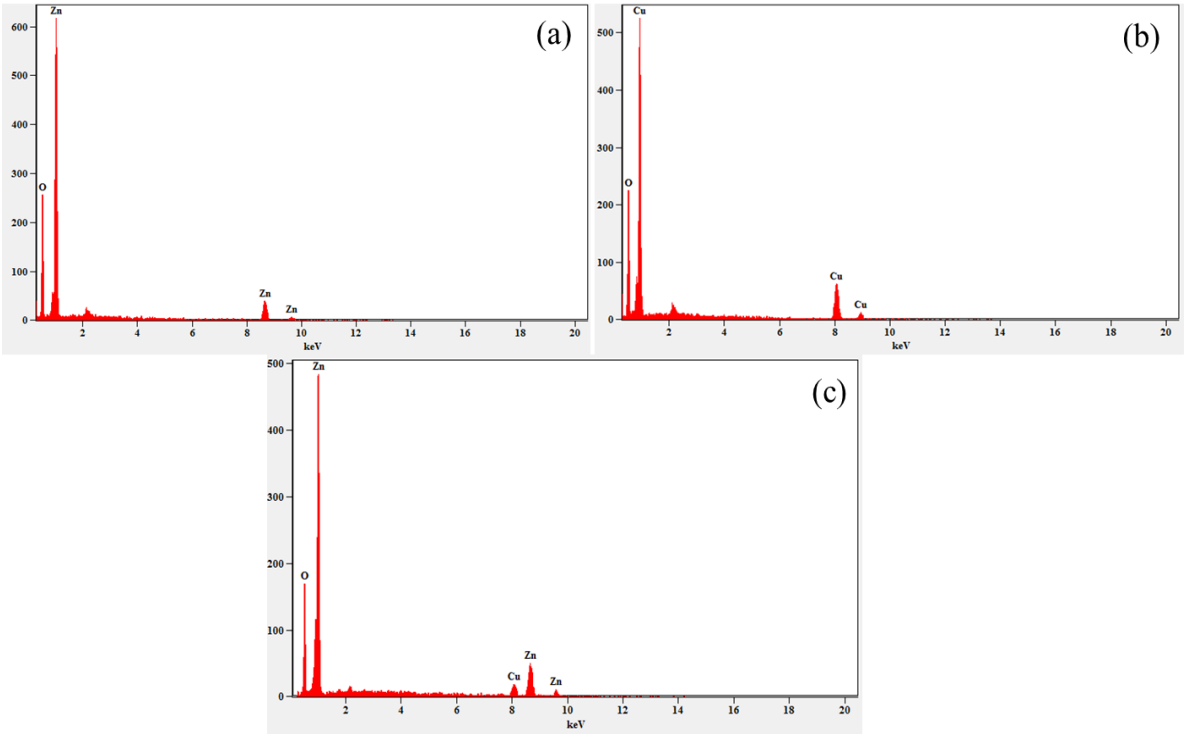

Figure 19: EDS spectra of (a) ZnO NPs, (b) CuO NPs, and (c) ZnO/CuO NCs.

4.2.4. TEM-HRTEM and SAED Analysis of ZnO/CuO NCs

Figures 20(a-c) and 21 (d-f) display TEM and HRTEM images of green synthesized ZnO (1:1) NPs, CuO NPs, and ZnO/CuO (20%) NCs, respectively. The analysis was carried out to gather and ascertain additional feature of the MA peel waste extract templated synthesized NPs and NCs such as morphology and crystallinity nature, in addition to the XRD and SEM analysis. Figure 20(a) shows the TEM micrograph of ZnO NPs synthesized within 1:1 ratio. Moreover, Figure 20(a) indicates that the synthesized ZnO NPs possess quasi-spherical shape and irregular shapes, which is also found to fit with the SEM analysis. Low level of agglomeration is observed and forms a cluster-like structure in the sample. Individual particles are also present in the images and this intern proves the role of the peel extract, which proves the formation of green ZnO NPs catalysts (Sathappan *et al.*, 2021). The particle sizes of ZnO NPs

are found to be around 20 nm, in accordance with the result of the XRD. Figure 20(b) showed the resulting TEM micrograph of green obtained CuO NPs. The Figure proves that the 20 nm resolution studies with TEM analysis revealed that the particles were found to be spherical in shape, less-agglomerated and also the particles are polydispersed. The polydispersion of the particles is a confirmation of the role of the peel extract, which also confirmed from SEM analysis (Luc *et al*., 2019).

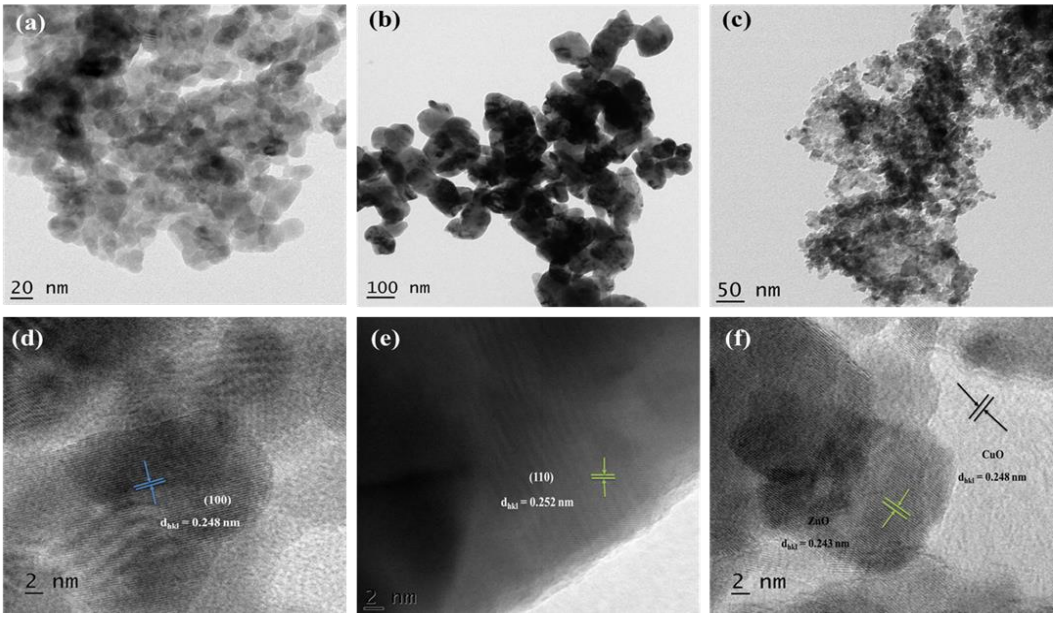

Figure 20: TEM micrograph of (a) ZnO (1:1) NPs, (b) CuO NPs, (c) ZnO/CuO (20%) NCs, (d) HRTEM image of ZnO (1:1) NPs, (e) HRTEM image of CuO NPs and (f) HRTEM image of ZnO/CuO (20%) NCs.

Furthermore, Figure 20(c) proved the resulted TEM image of ZnO/CuO (20%) NCs synthesized using suspension of peel of MA. As can be seen from the Figure 20(c), the NCs showed spherical shape with less agglomeration and polydispersed surface. Moreover, the image showed relatively homogenized surface as compared to the individual nanoxides due to the insertion of CuO into the pores size of ZnO NPs in addition to the presence of the peel extract. Figures 20(d-f) depict the HRTEM image of MA peel templated synthesized ZnO (1:1), NPs, CuO NPs, and ZnO/CuO (20%) NCs, respectively (Thatikayala & Min, 2021). Figures 20(d) and 20(f) with higher magnification present the high-resolution transmission electron microscope (HRTEM) of ZnO and CuO NPs, respectively. The particles with a fringe width of 0.248 and 0.252 nm were confirmed the formation of green nano crystalline ZnO and CuO NPs, respectively.

Moreover, Figure 21(f) showed the HRTEM image of ZnO/CuO (20%) NC with formation of clear nanocrystalline surface. The image also proves the presence of aggregation of fine particles with porous nature and reflects the presence and interactions with the extract of MA biomaterials. The HRTEM image

also shows the formation of heterojunction between ZnO and CuO with distinct lattices of (100) and (110) planes of ZnO match with the lattice spacing of 0.243 and 0.248 nm, respectively.

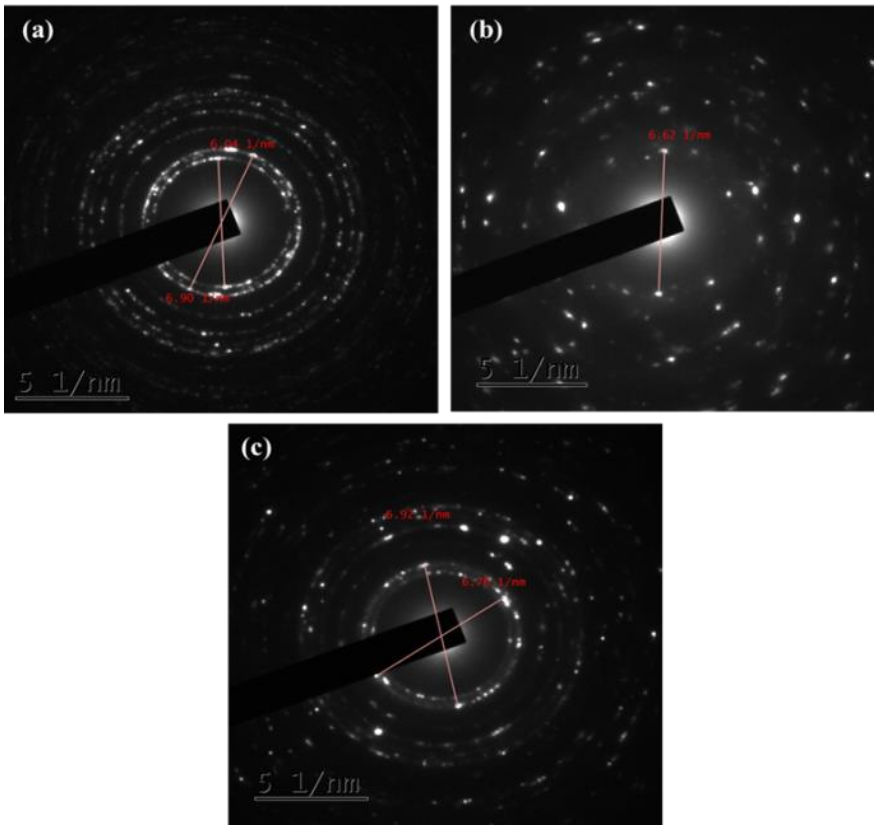

Figure 21: SAED pattern of (a) ZnO (1:1) NPs, (b) CuO NPs, and (c) ZnO/CuO (20%) NCs.

In addition to this, Figure 20(f) proves the existence of defect sites between the fringes, which is occurred due to the coupling phenomena. Hence, the HRTEM result shows the strongly anchored surfaces in the green synthesized ZnO and CuO NCs with a small lattice mismatch; and gain the result found to be well correlate with the lattice parameter values of the XRD analysis. The crystalline nature of the peel mediated synthesized ZnO (1:1) and CuO NPs and ZnO/CuO (20%) NCs also checked via surface area electron diffraction pattern (SAED) analysis, as represented in Figures 21(a-c), respectively. Moreover, the presence of white bright spots in the center of the SAED pattern within Figures 21(a-c), is an indication of the polycrystalline and nanocrystalline nature of ZnO NPs and CuO NPs as well their composites too (Ananda Murthy et al., 2021). In addition to (100) and (110) planes of hexagonal ZnO NPs and lattice planes of monoclinic CuO NPs within the XRD analysis, the same phenomenon was also observed in the SAED pattern, which again strongly confirms the formation of green ZnO/CuO (20%) NCs (Zhu *et al*., 2018). In all of the NPs and NCs, the presence of the ring like diffraction pattern is also another confirmation of nanocrystalline formation. Based on SEM, TEM, HRTEM and SAED analysis, it is possible to deduce the formation of ZnO (1:1) NPs, CuO NPs and ZnO/CuO (20%) NCs in the presence of MA peel waste extract.

Moreover, this analysis technique provides morphology, the polydispersed nature and as well the nanocrystalline phase of the biosynthesized NPs and NCs.

4.2.5. UV-DRS Analysis of ZnO/CuO NCs

UV-DRS spectra analysis technique could provide useful information about the electronic absorption properties of the NPs and NCs. The optical absorption properties of the as-prepared NPs and NCs were followed by characterization using UV-DRS and depicted in Figures 22(a-d). Here Figure 22(a) presents the absorption spectra of the green synthesized ZnO NPs synthesized in the presence of the peel extract with different concentration of zinc precursor. From the spectra, it was noticed that intensity of light absorption by ZnO NPs increases between 387 and 400 nm with increase in concentration of zinc acetate. The increase in absorption intensity could be due to the increase in the crystalline size with precursor concentration, which has close agreement with previous similar reports. The E_g determination of ZnO NPs was carried out by Tauc plot as illustrated in Figure 22 (b). The E_g of ZnO (1:1, 1:2, and 1:3) NPs and CuO NPs as well ZnO/CuO (10-25%) NCs were calculated based on the Kubelka-Munk theory. Accordingly, the E_g of ZnO NPs were found to be 3.24, 3.25 and 3.24 eV for the 1:1, 1:2, and 1:3 ratios, respectively and have close agreement with previous study reports (Singh *et al*., 2019). The E_g of all the as synthesized ZnO NPs are smaller than the E_g of the bulk ZnO (3.37 eV).The decrease in band gap of ZnO NPs synthesized with peel extract is attributed to the quantum confinement effect. In addition, the variation in band gap energy of the synthesized ZnO NPs within various volume ratios is due to the variation in the amount of extract and precursor salt. Since, as the amount of extract added into the precursor salt is increased, the optical property of the formed NPs will be decreased and so light absorption behavior also altered. Moreover, Figure 22(c) depicts the absorption spectra of the green synthesized ZnO, CuO, ZC10%, ZC1%, ZC20% and ZC 25% NPs and NCs.

As indicated in the Figure, all the green synthesized NPs of ZnO and CuO NPs exhibit strong absorption peaks around 390 nm. However, the band edges of the peaks of the NCs are extended into the visible region, indicating the insertion of CuO, which creates additional states in the band gap of ZnO, resulting in the red shift of the band edge of the NCs. The absorption intensities of ZnO/CuO composites were all obviously higher compared to pure ZnO NPs. Further observation demonstrates that the absorbance in the visible light region and UV light region increases with Cu dosage, and all the benefits that come from the synergistic effect of CuO and ZnO. It is clearly observed that the appropriate CuO adding into ZnO leads to a red shift in the optical absorption edge, which could be due to the strong interfacial coupling between ZnO and CuO NPs. This red-shift in absorption would be important for the photocatalytic degradation of MB dye (Saravanakkumar *et al*., 2018).

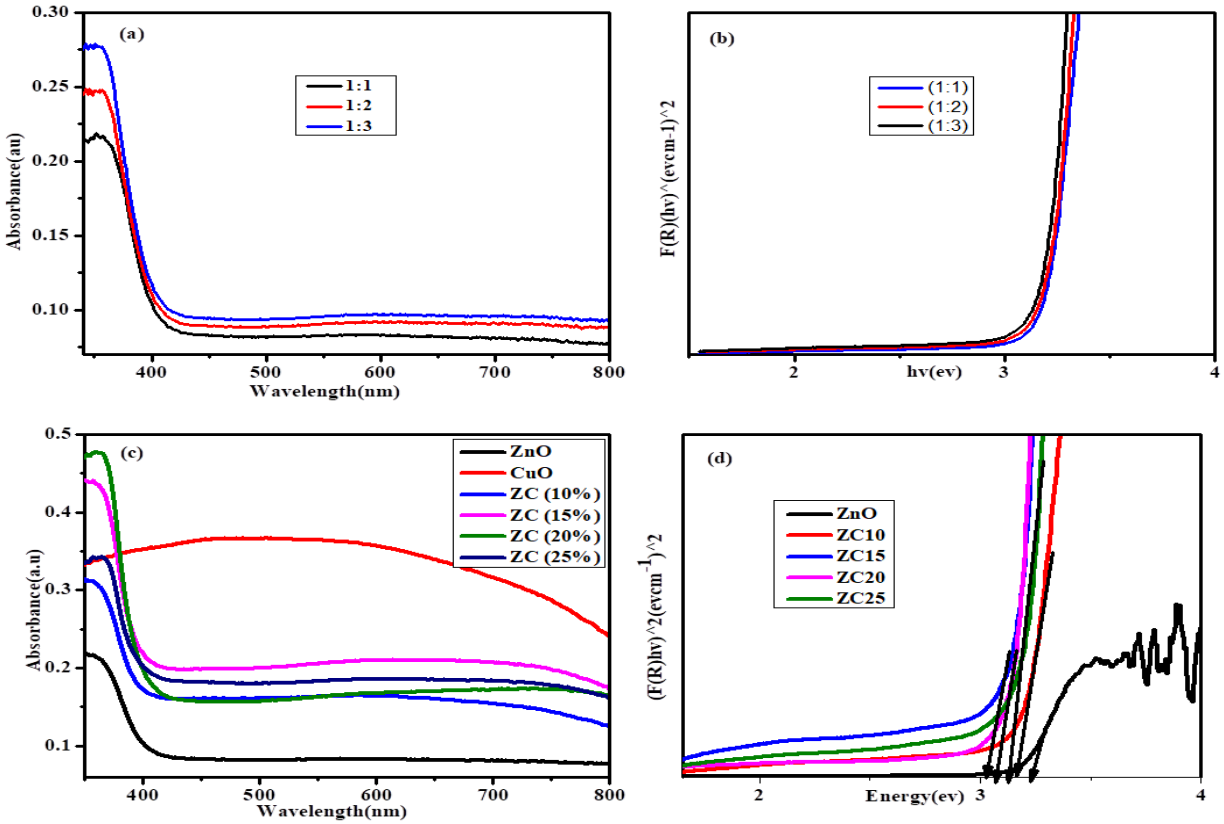

Figure 22: UV-DRS spectra of (a) ZnO NPs, (b) Tauc plot of ZnO NPs (c) UV-Vis DRS spectra of ZnO NPs, CuO NPs, and ZnO/CuO NCs and (d) Tauc plot of CuO NPs, ZnO NPs and ZnO/CuO NCs.

Figure 22 (d) illustrated the Tauc plot of CuO, ZnO, ZC10, ZC15, ZC20 and ZC25 NPs and NCs and E_g value was found to be 1.65, 3.24, 3.22, 3.21, 3.18 and 3.16 eV, respectively; which are in good agreement with the previous works. The observed band gap narrowing with the loading of CuO content was ascribed to the formation of interfacial contact among ZnO NPs and CuO NPs and due to ZnO NPs network defects as a result of incorporation of CuO (Prajapati & Mondal, 2021). The narrower band gap suggests easier excitation for an electron from the valence band to the conduction band in the oxide semiconductor. It has been found that the band gaps of green synthesized ZnO NPs are relatively high while that of ZnO/CuO NCs becomes low, which confirms that an increase in CuO ratio in the NCs results in a tangible decrease in the band gap energies. Hence, UV-DRS results confirmed that ZnO/CuO NCs can be selected as best photocatalyst in the visible light area. Furthermore, ZnO/CuO (15%), and ZnO/CuO (20%) NCs had strong absorption in visible region due to the presence of biomolecules from the leaf extract (K. Xu *et al*., 2017). Therefore, the results obtained from the UV-Vis DRS spectra were found to fit with the TGA/DTA analyses, confirming the presence of biomolecules from the peel extract, which is adsorbed over the surface of the as-prepared samples (Abebe & Murthy, 2022).

4.2.6. FTIR Analysis of ZnO/CuO NCs

In order to inspect the role of the peel extract, FTIR characterization was employed and carried out in the range of 400-4000 cm^{-1}. The FT-IR spectra of the peel extract and prepared NPs and NCs are shown in Figure 23. The FT-IR spectra of green assisted synthesized NPs and NCs showed broad absorption band in between 3400-3700 cm^{-1}, representing stretching vibration of O-H group, which confirm the presence of hydroxyl groups from the polyphenolic, alkaloids, flavonoids, alcoholic, and carboxylic compounds of extract in the synthesis of NPs and NCs (Nur et al., 2018). This intern confirms the presence of various capping and reducing bioactive molecules in the peel extract of MA. Moreover, this peal might also attribute to reversible dissociative absorption of hydrogen on Zn and O. The spectra of ZnO NPs, CuO NPs, and ZC20% NCs exhibited a band at wave numbers of 2854 and 2922 cm^{-1}, which were ascribed to the stretching vibration of C-H bond in CH_2 and CH_3 groups, respectively (Prajapati & Mondal, 2021). The weak band located at around 2280 cm^{-1} were attributed to the C-H stretching of aldehyde molecules and the band near 2343 cm^{-1}could be the absorption of atmospheric CO_2 on the metallic cation. In addition, the absorption peaks for carbonyl C=O stretching and O-H bending in alcohol were observed at1637and 1411 cm^{-1}, respectively (G.K. *et al*., 2015).

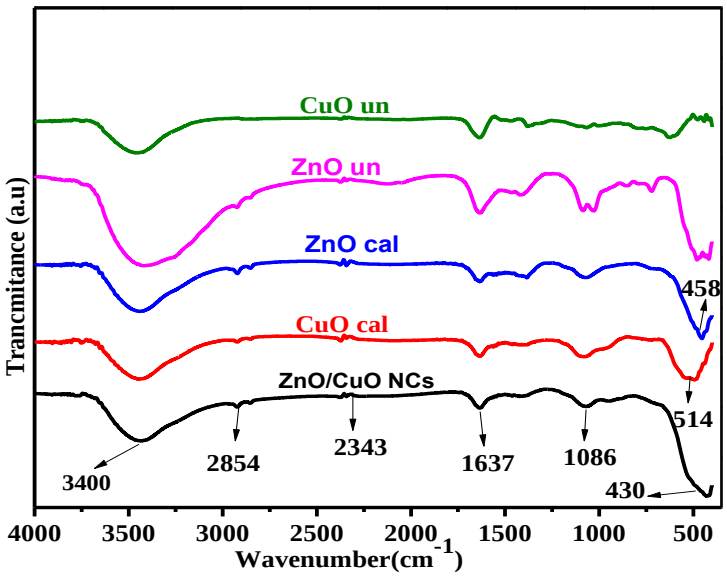

Figure 23: FTIR spectra of uncalcined and calcined ZnO and CuO NPs and ZnO/CuO (20%) NCs.

The peaks around 1086 $cm^{-1}$and 1040 cm^{-1} were due to C-O stretching in secondary alcohol and C-N stretching modes of aliphatic amines, respectively. These peaks might also relate to the anti-symmetric stretching vibration of NO_3^-, caused by the precursor groups. Furthermore, slight bands at 730-630cm^{-1}, 830 cm^{-1}, and at 960 cm^{-1} may corresponds to the C=C bending vibrations of unsaturated hydrocarbons present within the extract of the peel. Those peaks disappear in the calcined samples as they were burned

out and this implies that, after calcination the peel template NPs and NCs were formed and pure. The absorption peaks around 458 and 410 cm^{-1} in both calcined and un calcined ZnO samples are assigned to Zn-O bond similar to the previously report work that the vibration of Zn-O appeared in the range of 542-424cm^{-1}. This again intern confirms the wurtzite structure of ZnO NPs, as supported under the XRD analysis. The wavenumbers of 544-486 cm^{-1} in both calcined and uncalcined CuO samples are assigned to Cu-O stretching band that the vibrations of the Cu-O are in the range of 600-490 cm^{-1} (Asamoah et al., 2020). The peak appeared in the range of 543-430cm^{-1} for the coupled metal oxide ZnO/CuO NCs corresponds to the combined absorptions of Zn-O and Cu-O bonds. The shift of wavenumber at 458-400 cm^{-1}(Zn-O bond) was observed as the CuO is added to ZnO. The shift of wavenumber indicated that the addition of CuO may change the structure of ZnO NPs. What's important is that the FT-IR spectrum of ZnO/CuO NCs displays a low intensity peak at 1411, 1040, 730, 830 and 960 cm^{-1}, indicating the decrease of concentration of organic molecules of the peel extract after calcination process was carried out. However, some organic functional groups have not been completely removed after calcination and still their vibration bands appeared in the calcined sample. This may not implies that the green synthesized NPs and NCs are impure, instead the analysis confirms the role of the extract used during the synthesis process as green alternative template (Taghavi Fardood *et al*. 2017; Sherly *et al*. 2015).

4.3. Characterization of Co_3O_4 NPs

4.3.1. TGA/DTA Analysis of Co_3O_4 NPs

Figure 24 displays the TGA/DTA curve of *Solanum tuberosum* peel waste extract templated synthesized Co_3O_4 NPs. The processes performed during the heating were recorded by the TG and DTA curve depicted in Figure 24. Weight loss continued up to 346℃ associated with a strong exothermic peak in the DTA curve, which can be observed in the samples with organic content due to the combustion of organic molecules. Therefore, heating at 346℃ is necessary to obtain Co_3O_4 NPs from precipitates. As a result of thermal analysis, 450℃ were used as calcination temperature (Samuel *et al*., 2020).

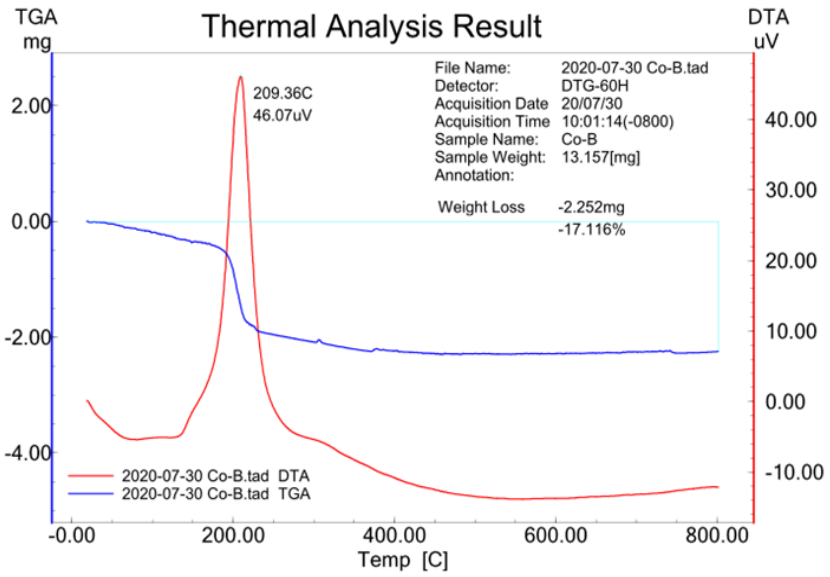

Figure 24: TGA/DTA curve of ST peel extract mediated synthesized Co_3O_4 NPs.

4.3.2. XRD Analysis of Co_3O_4 NPs

Figure 25 shows the XRD pattern of Co_3O_4 NPs synthesized within different volume ratio of precursor salt and extract. The diffraction peaks located ≈at 2θ of 19.01°; 31.37°; 36.85°; 38.5°; 44.88°; 55.71°; 59.4°; 65.26°; 74.31° and 77.5° corresponded to the miller indices (hkl) value of 111; 220; 311; 222; 400; 422; 511; 440; 533 and 622, respectively having JCPDS card number of 00-042-1467.

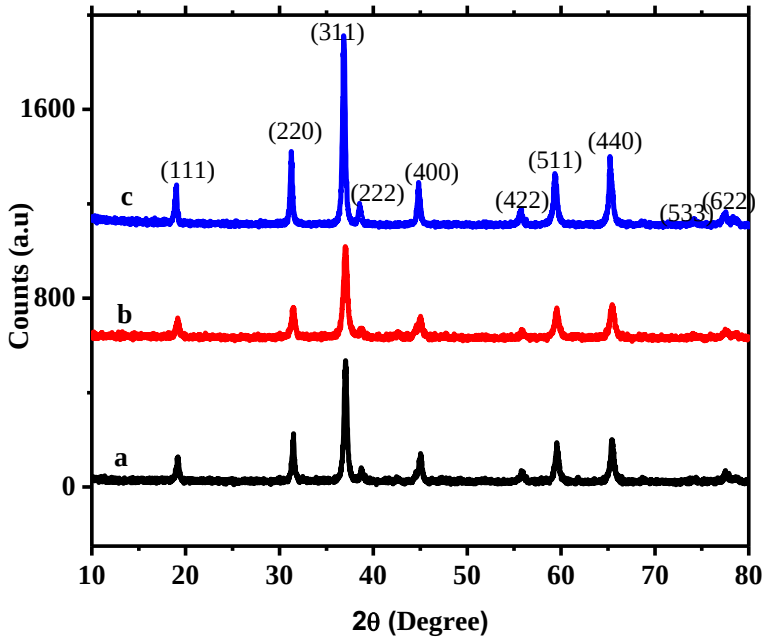

Figure 25: XRD pattern of Co_3O_4 NPs synthesized within (a) 1:2, (b) 1:1 and (c) 2:1 respectively.

This XRD result was found to be within good agreement presented in the literature. The XRD peaks are found to be very sharp indicating good crystallinity of the sample grains. The diffraction peaks of volume ratio (2:1) showed good crystalline as compared to the remaining volume ratios(Adino *et al.*, 2021). This

indicating that it has narrow diffraction peaks and has larger crystalline size as depicted in Figure 25b. The calculated average crystalline size of Co_3O_4 (1:1) was small as compared to Co_3O_4 (1:2), indicating it has lower precursor salt. The minor peaks reflect the impurities present in the synthesized NPs in the form of water soluble and water insoluble impurities that may be present on the surface of the synthesized NPs. Under the XRD spectra no additional diffraction peaks were found, indicating the formation of pure Co_3O_4 NPs. XRD results also indicated that the (311) plane was the preferred growth plane as (311) peak was the most intense (Luo *et al.*, 2019).

The obtained crystalline size of Co_3O_4 NPs was 26, 19, and 28 nm for the 1:2, 1:1, and 2:1 volume ratios, respectively. Co_3O_4 NPs biosynthesized using a volume ratio of 1:1 shows narrow diffraction peaks, indicating that it has a good crystalline structure as compared to the remaining ratio of synthesized Co_3O_4 NPs; because of high the maximum volume ratio of precursor salts (lower extracts) as compared to the amount of extract used. However, in the diffraction patterns of the Co_3O_4 synthesized using volume ratios of 2:1 and 1:2, a decrease in the intensity and a widening of the diffraction peaks are observed as compared to 1:1 samples, which is attributed to the decrease in the size of the crystals because of low concentration of precursor salts (higher ST extract) were present in the samples. The diffraction pattern of Co_3O_4 formed using 1:2 ratios are rigid and narrow diffraction peaks are observed as compared to Co_3O_4 synthesized within 1:1 volume ratio. This indicates that Co_3O_4 (1:1) has a good crystalline structure because of the existence of high amount of ST peel extract used during the synthesis process as a stabilizing and a capping agent which fits with the porosity of the Co_3O_4 precursor salt (Abass *et al*., 2021). The average crystalline size of Co_3O_4 (2:1) was found to be larger than the remaining ratios, indicating that it has narrow diffraction peaks and has good crystalline structure as depicted in Figure 25.

4.3.3. SEM-EDS Analysis of Co_3O_4 NPs

The SEM analysis result confirms that all the three ratios of Co_3O_4 NPs possess nearly spherical structural morphology. As can be depicted in Figure 26a-c, the SEM images of Co_3O_4 NPs are too crystalline. In addition, Co_3O_4 NPs are scattered over the surface without any aggregated particles, which is attributed due to the presence of extract of ST peel waste extract. Moreover, Figure 26d presents the resulting EDS spectra of Co_3O_4 NPs. It has been found that the EDS spectrum contains Co and O as a major peak and C minor peak. The presence of C within the EDS spectrum is an indication as Co_3O_4 NPs was formed via green protocol; C is obtained due to from peel waste extract of ST (Mohammadi *et al*. 2021; Okwunodulu *et al*. 2019).

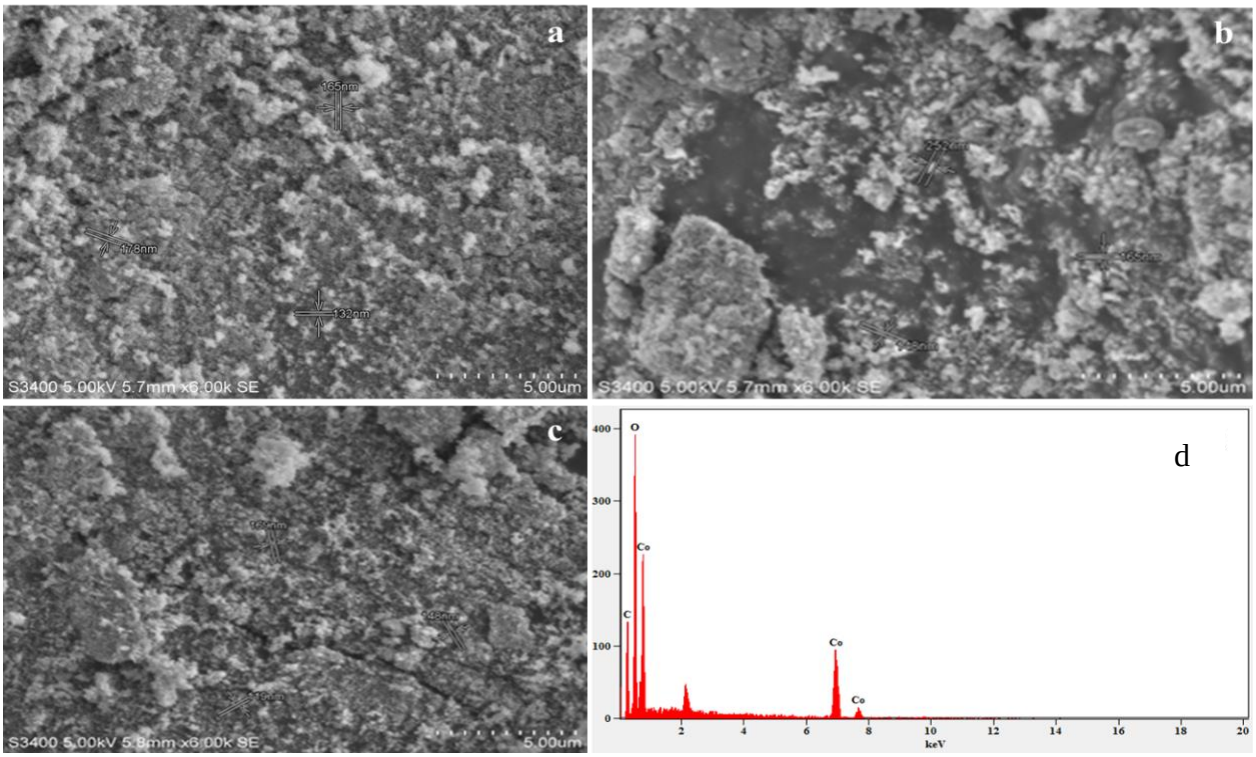

Figure 26: SEM spectra of Co_3O_4 NPs synthesized within volume ratio of (a) 1:2, (b) 1:1), (c) 2:1 and (d) EDS spectra of Co_3O_4 (1:1) NPs.

4.3.4. TEM-HRTEM and SAED Analysis of Co_3O_4 NPs

The TEM image of the biogenic synthesized Co_3O_4 (1:1) NPs at 50 magnification scale are presented in Figure 27. The morphology was found to be spherical as confirmed by SEM analysis too. Assembled spheres indicated presence of improved connectivity, dispersibility, and homogeneity between the formed particles. Moreover, the HRTEM image also confirms the poly-nanocrystalline nature of green Co_3O_4 (1:1) NPs, and it has been found to have a well-defined shape and visible grain boundaries, which can be achieved via a controlled synthesis procedure in the presence of bioactive molecules from the crude extract of ST peel waste extract (Sivachidambaram et al., 2017b). In addition to this, the crystallinity nature of the biogenic synthesized Co_3O_4 (1:1) NPs also confirmed by SAED characterization techniques. The SAED pattern (Figure 27c) with high magnification image having lattice fringes of 0.25 nm are exactly coincide with the lattice planes in XRD pattern of Co_3O_4 NPs (Bekele et al., 2022).

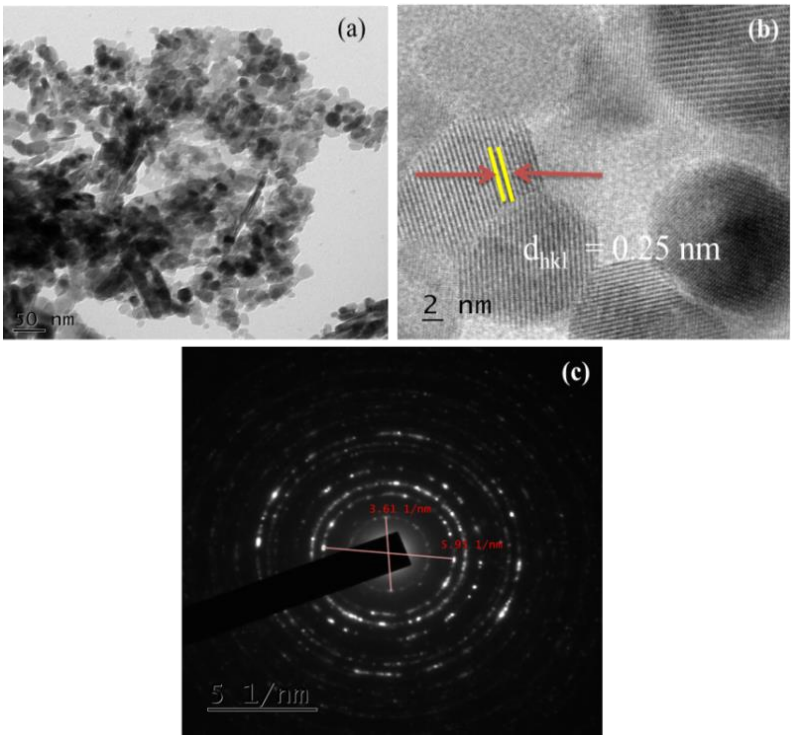

Figure 27: (a) TEM, (b) HRTEM, and (c) SAED pattern of Co_3O_4 NPs.

4.3.5. UV-DRS Analysis of Co_3O_4 NPs

The band gap energy of synthesized NPs was estimated by using ultra violet visible diffuse reflectance spectroscopy (UV-DRS). The band gap is the minimum energy needed for an electron to be excited from the top of the valence band to the bottom the conduction band. Once that minimum energy is reached then the sample can start absorbing light and electrons are excited from the valence band to the conduction band. The bandgap energy was determined based on the numerical derivative of the optical absorption coefficient using Tauc's plot method and presented in Figure 28. The bandgap energy of Co_3O_4 NPs was found to be 3.25, 3.33, and 3.37 eV for the 1:1, 1:2, and 2:1 volume ratios of Co precursor salt and potato peel extract, respectively.

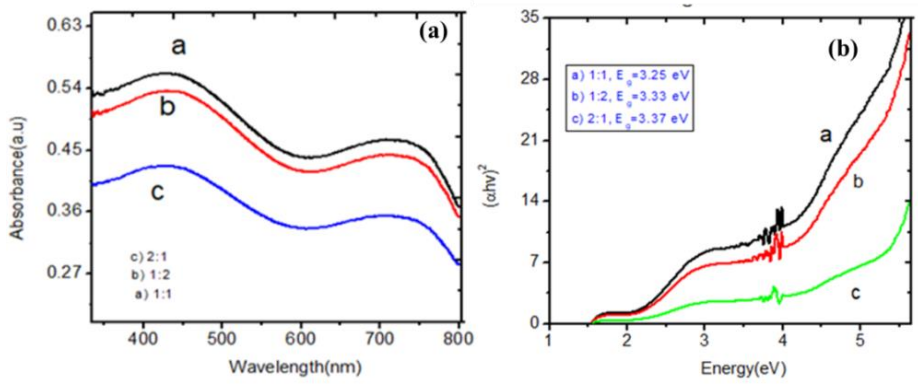

Figure 28: (a) UV-DRS spectra and (b) Tauc plot of Co_3O_4 NPs.

The variation in the E_g for the different kinds of biosynthesized Co_3O_4 NPs is due to the variation in volume ratio between Co precursor salt and the peel extract that leads the biosynthesized Co_3O_4 NPs to absorb at different regions of UV-Vis light. Broadening of the spectrum indicates the polydispersed nature of the biosynthesized NPs and the blue shift of the absorption curve results in the reduction of the bandgap energy. If the size of the particle is very small light interacts with the samples instead of absorption as a result parts of the light scattered and reflected. UV-Vis spectroscopy result showed that the typical peaks of Co_3O_4 NPs were detected in the range of maximum wavelength between 427-741 nm and these peaks indicated the transfer processes of Co (II) and Co (III) with oxygen, respectively (Igwe & Ekebo, 2018).

4.3.6. FTIR Analysis of Co_3O_4 NPs

Figure 29 shows the FTIR spectra of calcined and uncalcined Co_3O_4 NPs and peel extract of ST and were recorded in the range of 4000-400 cm^{-1}. FTIR spectrophotometer was used to analyze the functional group of ST mediated synthesized Co_3O_4 NPs.

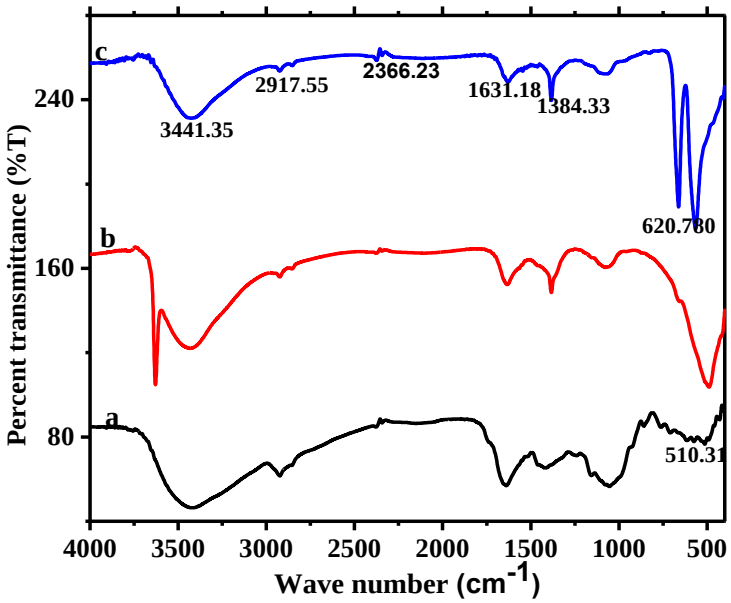

Figure 29: FTIR spectra of (a) ST peel, (b) uncalcined Co_3O_4 NPs, and (c) calcined Co_3O_4 NPs.

The wavelength of 4000-400 cm^{-1} was used for the analysis of functional groups of Co_3O_4 NPs, as can be depicted in Figure 29. The -OH functional groups could be observed at the frequency of 3500-3000 cm^{-1}. The C=O functional group could be observed at the wavenumber of 1840.11$cm^{-1}$for extract of ST peel powder and 1780.45 cm^{-1} for the calcined and uncalcined Co_3O_4 NPs. The wavenumber of 2917.55 cm^{-1} are the C-H and C-O vibrations of an aromatic aldehyde. While the absorption peak observed at 1631.18 cm^{-1} corresponds to C = O peak, which indicates the ketone functional group and also the ammine functional group. The broad peak observed in the range of 1384.33-720.780 cm^{-1} corresponds to C-C

stretching of the aromatic groups obtained from the peel extract of ST as well as the saturated primary alcohol containing the C-O bond (Mohammadi *et al*., 2021).

4.4. Photocatalytic Degradation Activity of NCs on Methylene Blue Dye

4.4.1. Photocatalytic Degradation of MBD by TiO_2/rGO NCs

Figures 30a and e show the changes in the MB absorption spectra during photocatalytic degradation with TiO_2-2c (a) and TiO_2-2m (e) nano-photocatalyst at different solar irradiation times varying from 0 to 60 min. As it can be observed from the Figures, the degradation of MB using TiO_2 only nano-photocatalyst is very low indicating low photocatalytic activity of TiO_2 only NPs. From the result presented, only 62% and 58.5% of the dye was adsorbed in the presence of TiO_2-2c and TiO_2-2m nano-photocatalysts, respectively. The low photocatalyst adsorbed efficiency of TiO_2 only NPs could be attributed to the high electron-hole recombination rate (Zelekew *et al*., 2021).

Figure 30 also depicts photocatalyst degradation of MB of CS peel extract mediated synthesized TiO_2/rGO (b-d) and MA mediated synthesized TiO_2/rGO (f-h) nano-photocatalysts using different volume ratios. Among the various TiO_2/rGO NCs photocatalysts, TiO_2/rGO-1.5c and TiO_2/rGO-1.5m showed the highest degradation efficiency of 94.28% and 94.25%, respectively, after 60 min irradiation. Moreover, the result showed that the visible light photocatalytic degradation of MB is dependent on the concentration of rGO composited with TiO_2 nano-photocatalyst. As supported by the previous report, high surface area of the NCs photocatalysts promotes increased dye adsorption on its surface. Furthermore, the improved in photocatalytic performance of TiO_2/rGO nano photocatalysts might also be due to the decrease in the electron-hole recombination rate since rGO in TiO_2/rGO NCs can act as an electron acceptor (X. Li *et al*., 2013).

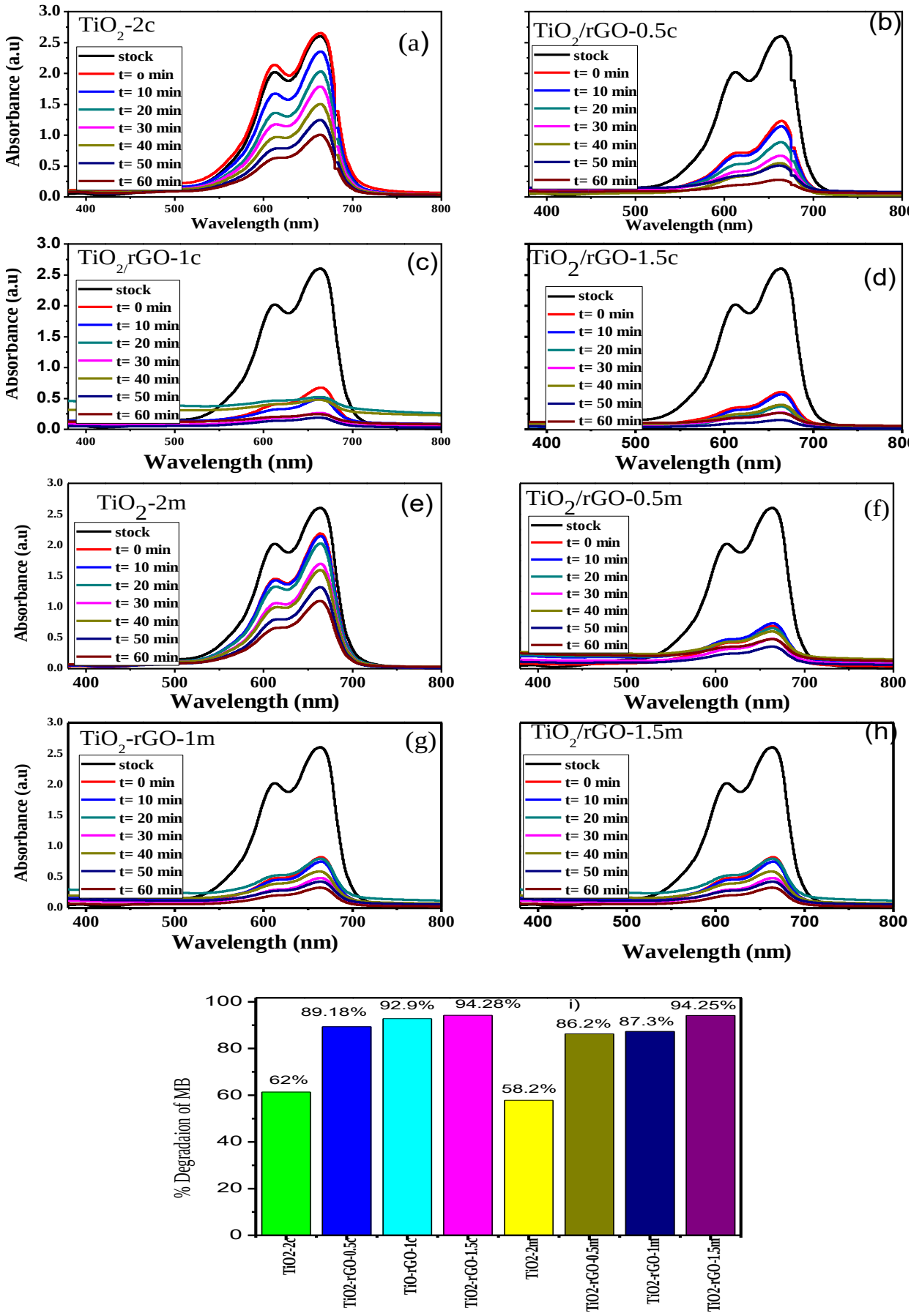
TiO2-2c
(a)
TiO2/rGO-0.5c
(b)
TiO2/rGO-1c
(c)
TiO2/rGO-1.5c
(d)
TiO2-2m
(e)
TiO2/rGO-0.5m
(f)
TiO2-rGO-1m
(g)
TiO2/rGO-1.5m
(h)
stock
t= 0 min
t= 10 min
t= 20 min
t= 30 min
t= 40 min
t= 50 min
t= 60 min
Absorbance (a.u)
Wavelength (nm)
i)
% Degradaion of MB
62%
89.18%
92.9%
94.28%
58.2%
86.2%
87.3%
94.25%
TiO2-2c
TiO2-rGO-0.5c
TiO-rGO-1c
TiO2-rGO-1.5c
TiO2-2m
TiO2-rGO-0.5m
TiO2-rGO-1m
TiO2-rGO-1.5m

Figure 30: Visible lights Photocatalytic degradation of CS and MA templated synthesized TiO_2 NPs and TiO_2/rGO NCs.

Reaction kinetics study models for the photocatalytic degradation of MB dye using both TiO_2 nanocatalysts and TiO_2/rGO composite nanocatalysts were tested by using first and second order pseudo kinetic models. As it can be observed from Figure 31a, the photocatalytic degradation of MB fit pseudo first order model with the correlation constant of R^2 = 0.95 min^{-1} for the TiO_2-2c and R^2 = 0.953 for the TiO_2-m nano-photocatalysts.

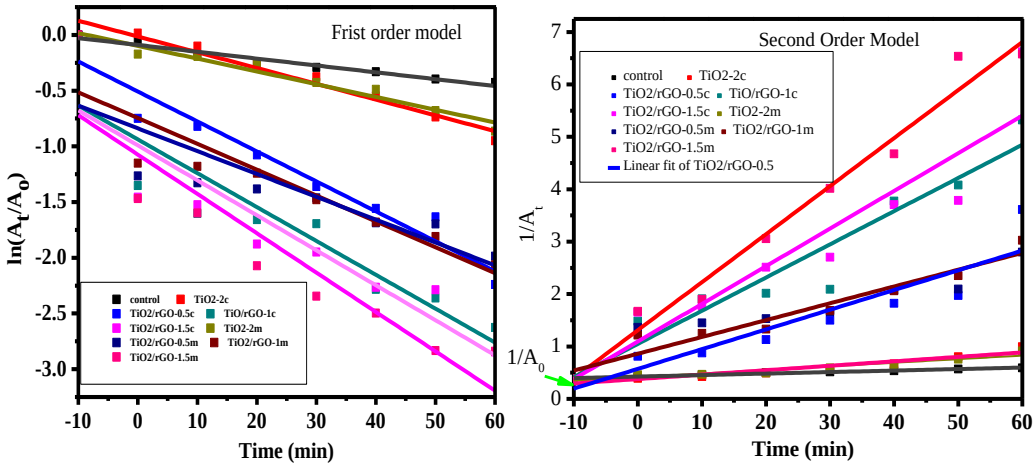

Figure 31: Pseudo first (a) and pseudo second (b) order kinetic models for Photocatalytic degradation of MB dye using CS and MA templated synthesized TiO_2 NPs and TiO_2/rGO NCs.

Table 1 represents the corresponding calculated parameters for first order and second order kinetic data model of MB dye degraded by green formed TiO_2 nanocatalyst and TiO_2/rGO NCs under visible light irradiation.

Table 1: The calculated pseudo first and second order kinetic data.

First order ($\ln(A_t/A_i)$= -kt) data				Second order ($1/A_t$= kt + $1/A_o$) data			
Catalyst	Intercept	slope	R^2	Catalyst	Intercept	slope	R^2
Control	-0.098	-0.006	0.955	Control	0.42581	0.00287	0.9802
TiO_2-2c	-0.01	-0.014	0.95	TiO_2-2c	0.37816	0.00846	0.88616
TiO_2/rGO-0.5c	-0.051	-0.024	0.83	TiO_2/rGO-0.5c	1.09519	0.07185	0.85933
TiO_2/rGO-1c	-0.94	-0.03	0.8	TiO_2/rGO-1c	1.04936	0.06333	0.85933
TiO_2/rGO-1.5c	-1.07	-0.036	0.828	TiO_2/rGO-1.5c	1.09519	0.07185	0.85933
TiO_2-2m	-0.098	-0.011	0.953	TiO_2-2m	0.41428	0.00688	0.8976
TiO_2/rGO-0.5m	-0.084	-0.02	0.66	TiO_2/rGO-0.5m	0.5731	0.03761	0.81955
TiO_2/rGO-1m	-0.75	-0.02	0.79	TiO_2/rGO-1m	0.8615	0.03209	0.92895
TiO_2/rGO-1.5m	-1.07	-0.035	0.819	TiO_2/rGO-1.5m	1.31106	0.09163	0.97396

Furthermore, the photocatalytic degradation of MB in the presence of green templated TiO_2/rGO green nanocatalysts were found to be fit with pseudo second order kinetics with rate constant of 0.974 min^{-1} for TiO_2/rGO-1.5m. The implication of fitting with first and second order kinetics, confirms the stability of the catalyst as well confirms that the rate of degradation of MB dye in the presence of those catalyst is both first and second order.

Figure 32 (a-c) showed the influence of pH of the solution on the degradation eff iciency of methylene blue using TiO_2/rGO nanophotocatalysts at pH 1, 7, and 13 (strong acid, neutral and strong base media), respectively. The change in the pH of the solution influences the surface of the nanocomposite-catalyst, thereby causing a change in adsorption and the reaction rate (Azeez *et al*., 2018). The point of zero charges of the TiO_2/rGO-1.5c was estimated to be at pH 7 and as a result the photocatalyst surface could possess negative charge at pH > 7, and positive charge at pH < 7.

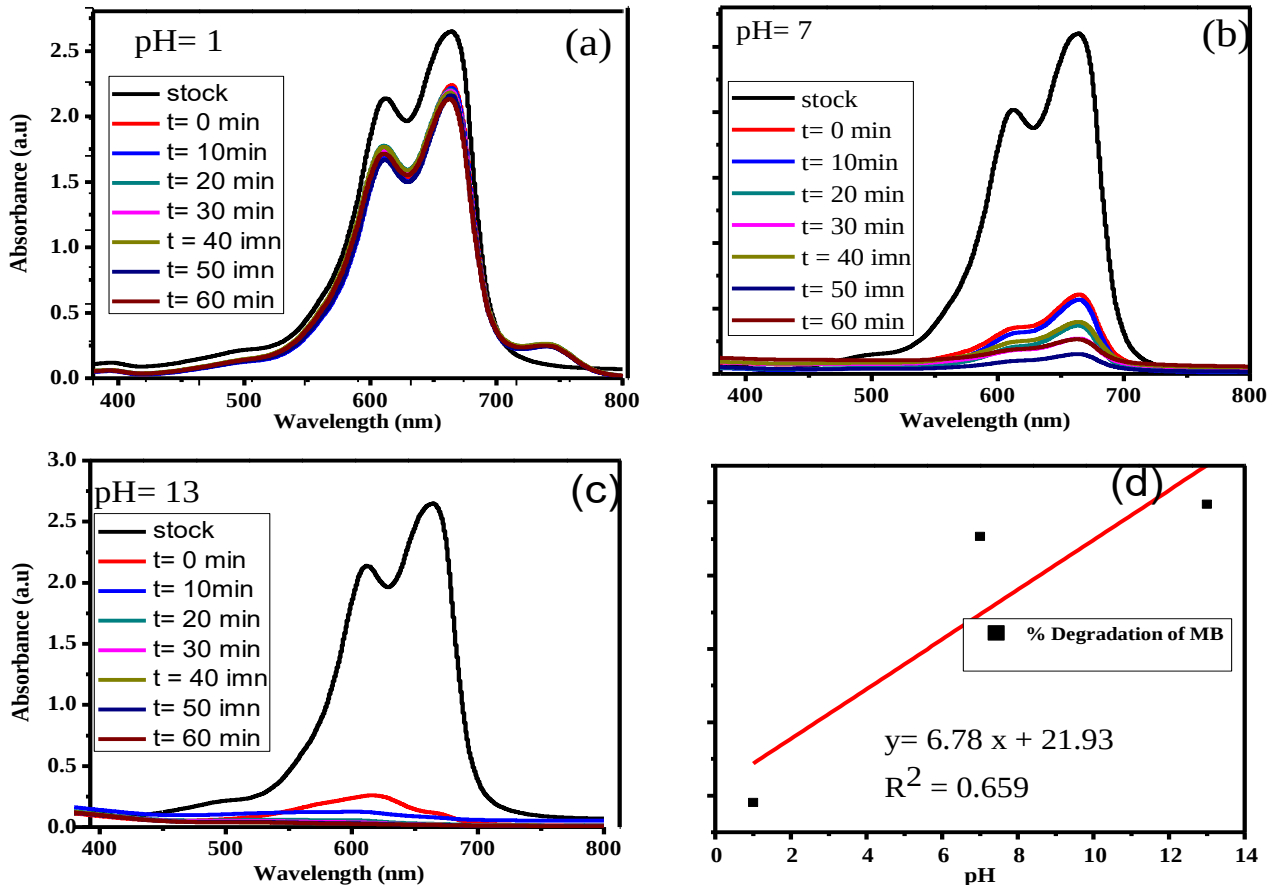

Figure 32: Effect of pH (a-c) and % of degradation (d) on the photocatalytic degradation of MB in the presence of TiO_2/rGO-1.5c NCs.

It was observed that, when the pH of solution changed from pH 1 to pH 7, the degradation efficiency of the NC increased from 18.1 to 90.7, respectively. The low degradation efficiency of MB in the presence of

TiO_2/rGO nanophotocatalysts at pH 1 could be due to the electrostatic repulsion between the positively charged green nanophotocatalysts surface and the cationic methylene blue, while no such repulsion occurs at pH 7. The photocatalytic degradation of MB dye in the presence of green templated synthesized TiO_2/rGO nanophotocatalysts was found to be dependent on the pH value. This pH dependence of photocatalyst activity of the NC might be due to its effect on the NC's surface charge, size, and valance and conductance bond positions (I. Khan *et al*., 2020). As could be depicted in Figure 32c, the highest degradation of MB dye was obtained at pH 13 with degradation efficiency of 99.4%. This indicates that alkaline pH favored the adsorption of the dye due to the electrostatic attraction between the negatively charged catalyst surface and cationic methylene blue dye. Furthermore, the neutral pH is known as the zero point of charge where the surface of CS mediated synthesized TiO_2/rGO NCs has no dye concentration (Zhang *et al*., 2010).

Figure 33 shows the effect of initial MB dye concentration in the presence of CS fruit peel extract templated synthesized TiO_2/rGO-1.5c NCs photocatalyst. The effect of initial MB dye concentrations on the photocatalytic efficiency of the TiO_2/rGO-1.5c was investigated by varying the concentration of MB dye (10, 20, and 30 ppm) while fixing the amount of the photocatalyst NC (30 mg/L) at pH of 7. It has been found that a significant decrease in the percentage of degradation was observed with an increase in the initial dye concentration of MB dye (Mahlake *et al*., 2019). This might be caused by the saturation of the surface of the green TiO_2/rGO nanocomposite catalysts. In addition, the decrease in photodegradation with increase in initial concentration of MB might also be caused by the interference for visible light to penetrate and reach the catalyst surface, thereby lowering the production of $^{\cdot}OH^-$ radicals. Furthermore, the reaction rates were found to be decreased with an increase in concentration of MB with rate constants of 0.04 min^{-1} for 10 mg/L, 0.03 min^{-1} for 20 mg/L and 0.02 min^{-1} for 30 mg/L (Figure 33d).

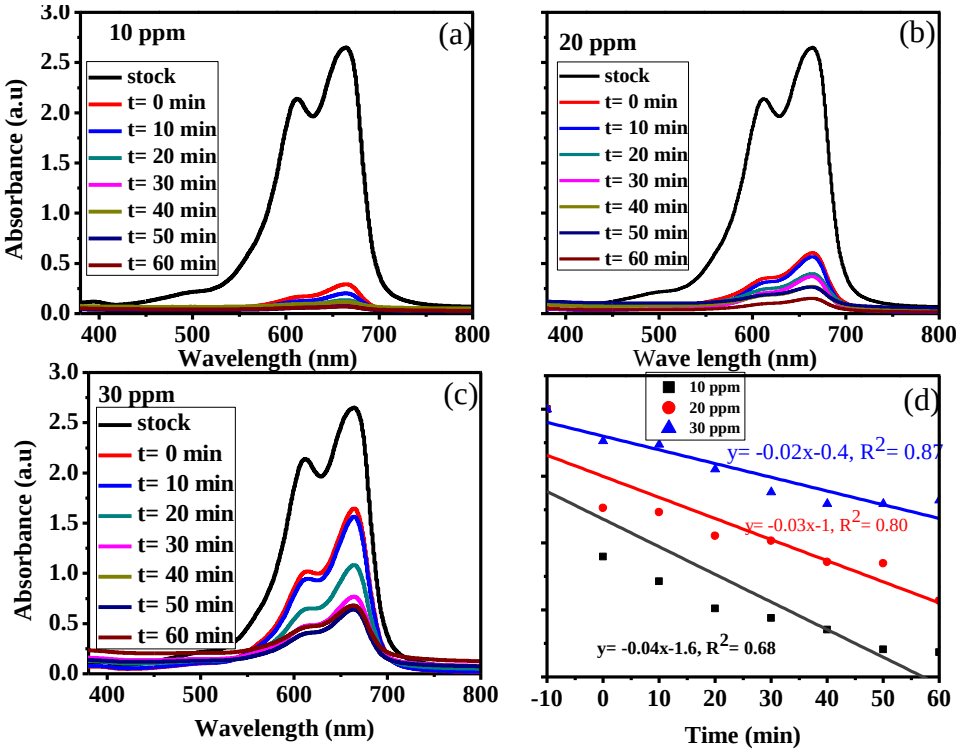

Figure 33: Effect of initial concentration of MB in the presence of synthesized TiO_2/rGO-1.5c NCs green catalyst.

In order to gain further information on the degradation removal of MB dye, the dosage of green templated TiO_2/rGO-1.5c nanocomposite photocatalyst was also altered in the range of 20 mg/L, 30, and 50 mg/L while keeping the pH and the dye concentration to be 7 and 10 mg/L, respectively.

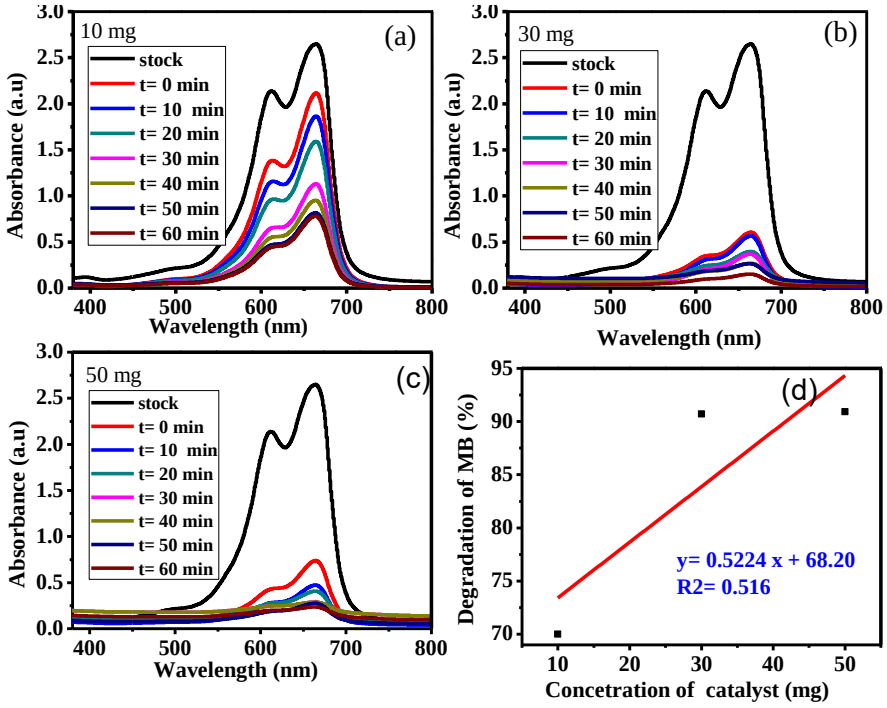

Figure 34: Effect of CS peel extract mediated synthesized TiO_2/rGO-1.5c NCs green catalyst dosage on the photocatalytic degradation of MB.

As it is depicted in Figure 34(a-c), maximum degradation efficiency of 90.92% and 90.70%) were obtained with 50 and 30 mg TiO_2/rGO-1.5c dosage, respectively, due to increase in the total number of active sites as the dosage of the photocatalyst is increased (Gnanaprakasam *et al*. 2015; Sathiyan *et al*. 2020).The effect of visible light illumination contact time from 0-60 min interval was carried out using 20 mg/L aqueous solution of MB dye at pH 7 in the presence of 30 mg TiO_2/rGO-1.5c are presented in Figure 35.

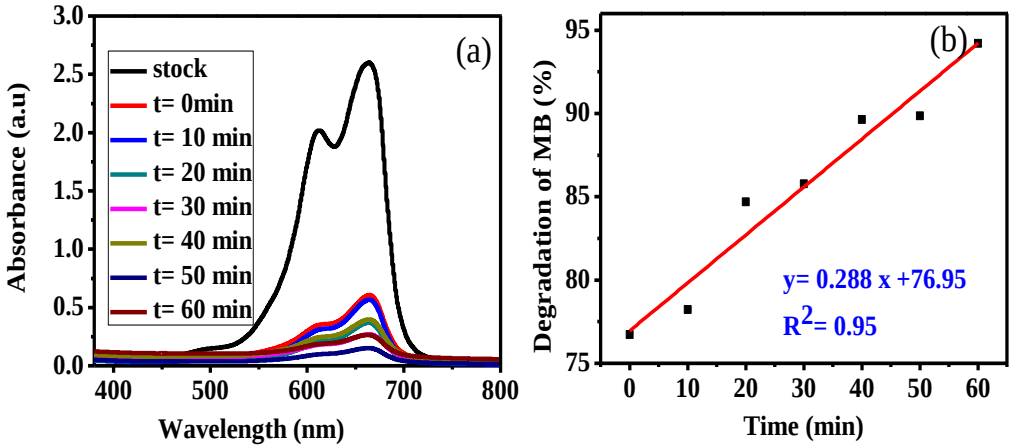

Figure 35: Effect of contact time (a) and % of degradation (b) on the degradation of MB using optimized CS peel extracts templated TiO_2/rGO-1.5c NCs green catalyst.

The reaction was started in dark condition for 10 minutes to attain sorption-desorption equilibrium between the catalytic surface and the dye. The result showed that a noticeable gradual increase of photocatalytic rate with increasing illumination time. After 60 min, the rate reached its optimum removal efficiency, 94.4% and a linear relationship between degradation of MB dye with increase in contact time was observed. This is because prolonging irradiation time allows light to fall on the catalyst surfaces and induce formation of photon excited species and enhances the photocatalytic activities (Li *et al*. 2019; Meng *et al*. 2011).

4.4.2. Photocatalytic Degradation of MBD by ZnO/CuO NCs

The photocatalytic activity of the green ZnO, CuO, and ZnO/CuO nanocatalysts were investigated for the decomposition of MB under visible light irradiation. Figures 36a and 36b illustrate the absorption spectra for the decomposition of MB dye solution under visible light in the presence of ZnO and CuO single green nanocatalyst, respectively. The single green ZnO nanocatalyst showed photocatalytic activity efficiency of 57%, which should be ascribed to the numerous oxygen vacancies on the green obtained ZnO catalyst surface, while the lower photocatalytic activity (50%) of CuO nano-catalyst could be as a result of rapid recombination of photo generated electrons and holes (U. Khan *et al*., 2022). However, all the ZnO/CuO

green NCs catalysts have showed better photocatalytic performance as presented in Figure 36 than pure ZnO and CuO green single oxide nanocatalysts. The higher photocatalytic activity of ZnO/CuO NCs could be associated with copper oxide, which acts as electron trap that inhibits e^-/h^+ recombination. Furthermore, the synergistic effect of ZnO and CuO green nanocatalysts could enhance the photocatalytic activity by forming heterojunction at the interface of the two semiconductors, which are effectively separated due to the band coupling between ZnO and CuO. In addition to this, the improvement in the photocatalytic performance of the CuO/ZnO NCs is that these NCs utilize visible light in addition to the UV light (Harish *et al.*, 2017).

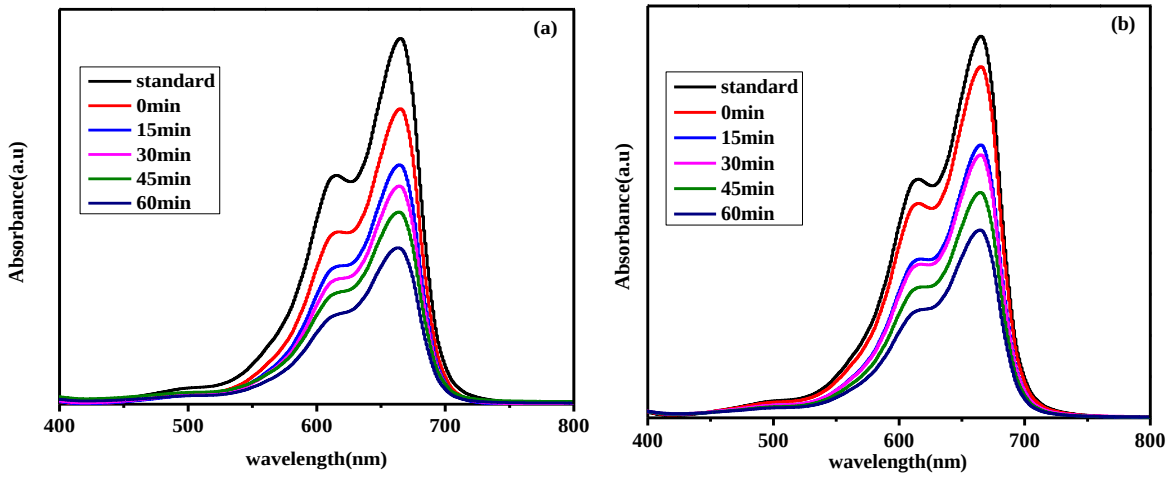

Figure 36: MB dye degradation under visible light irradiation in the presence of (a) ZnO and (b) CuO green nanocatalysts.

Many reports have suggested that there is an optimum CuO loading in CuO/ZnO NCs. Therefore, this study also attempted to investigate the optimum CuO loading in the ZC green catalyst. Figure 37**(**a-d**)** shows the reduction of MB dye solution under visible light by using green ZnO/CuO photocatalyst with different CuO loadings ranging from 10-25% into ZnO and the Figure illustrates the degradation rate of MB raise with the increasing of CuO loading.

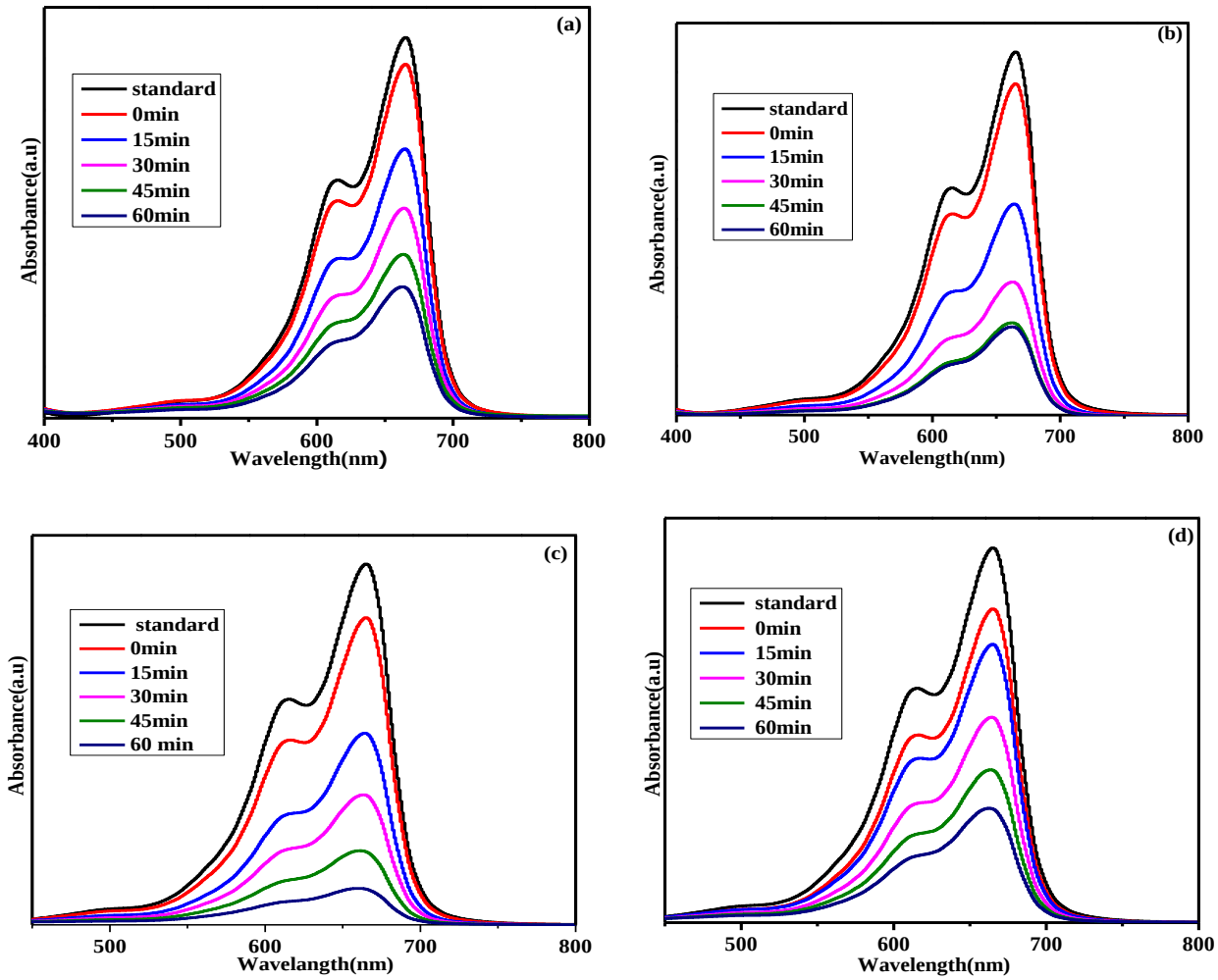

Figure 37: MB dye degradation under visible light irradiation in the presence of (a) ZC10, (b) ZC15, (c) ZC20 and (d) ZC25 green NCs catalyst.

Furthermore, Figure 37a also illustrate that the degradation efficiency is found to be increased with an increase with CuO loading up to 10% CuO content and decreased for further increase of CuO (25%). The variation of the photocatalytic efficiency should be mainly connected with the change of CuO crystallite size as observed in XRD analysis. When CuO crystallites gradually grow up, the crystalline quality is improved, which is favorable for photo generated electrons and holes to migrate to crystal surface. However, with the further grown-up of CuO crystallites, photo catalytic activity was declined. These could be related to two main reasons; firstly as CuO crystalline is grown, charge carriers need more time to migrate to crystal surface to participate in redox reactions, which increases the possibility of the recombination of photo generated electrons and holes inside the crystallites; secondly the over dose of CuO could blocked the active site of ZnO. Similar findings were also reported by Sherly *et al*., which supports the present work. It means that the ratio of CuO to ZnO in the CuO/ZnO NCs is very important for

the photocatalytic degradation of MB dye under visible light irradiation (Xu *et al*. 2017b; Tadesse *et al.* 2021).

The plot of $\ln(C/C_0)$ verses irradiation time gives the rate constant for the synthesized green nanocatalyst as shown in Figure 38(b and c). The rate constant for ZnO, CuO, ZC nanocatalysts were tabulated in Table (2). Among biosynthesized ZnO/CuO NCs catalysts, the ZC20 possess the highest degradation constant (0.035/min) which is about 5 times higher than that of ZnO (0.007/min).

Table 2: The rate constant and degradation efficiency of ZnO, CuO, and ZnO/CuO green nanocatalysts based MB dye under visible light irradiation.

Catalysts	K ($min^{-1)}$	Degradation efficiency (%)
ZnO	0.007	57
CuO	0.006	50
ZC10	0.015	60
ZC15	0.022	80
ZC20	0.035	90
ZC25	0.016	70

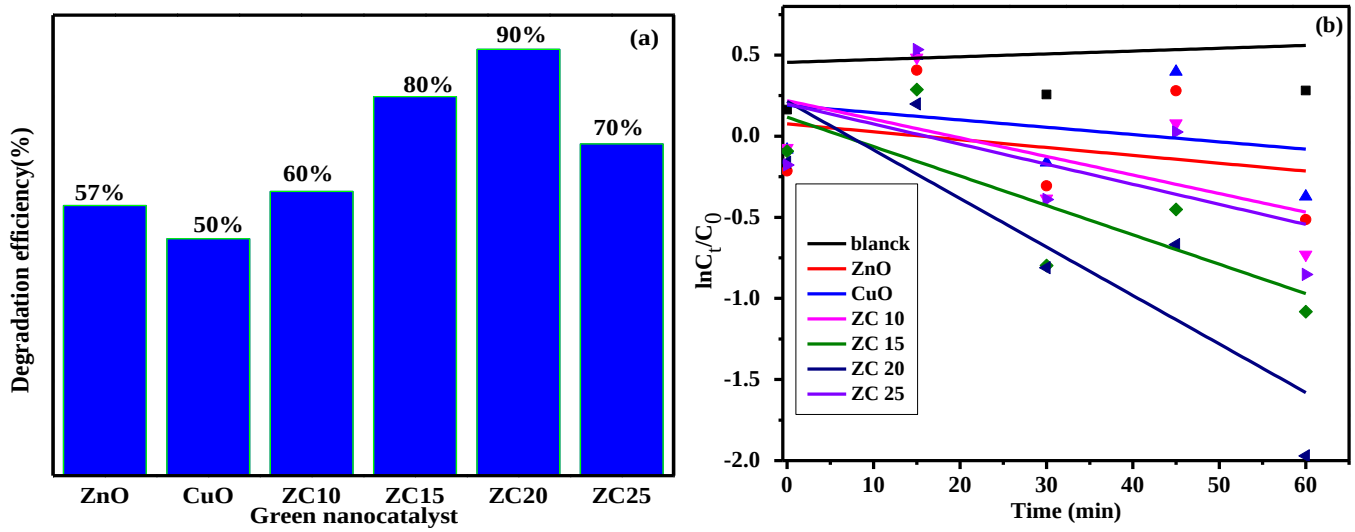

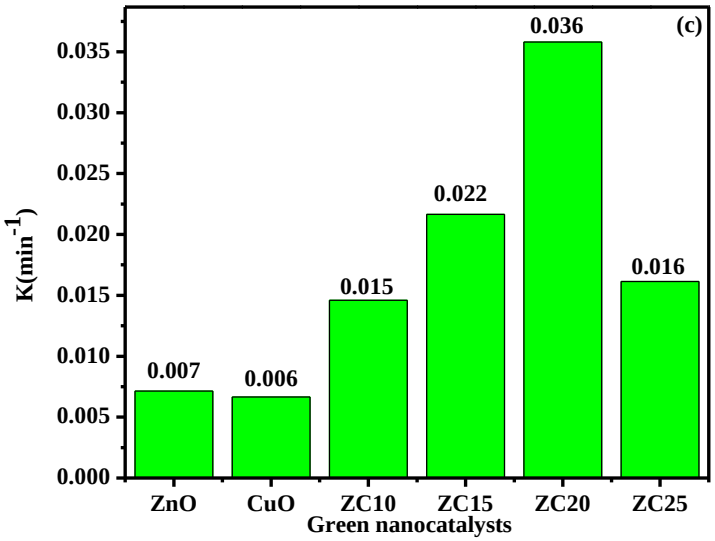

Figure 38: (a) MB dye degradation using green catalysts, (b) kinetics of MB dye degradation, and (c) rate constant of MB dye degradation.

Table 3: The calculated first order kinetic data model of ZnO/CuO nanocatalyst based MB dye degradation.

Catalyst	Intercept	Slope	R^2
Blank	0.45519	0.45519	-0.31738
ZnO	0.07566	-0.00484	-0.22031
CuO	0.19028	-0.0045	-0.22459
ZC10	0.21907	-0.01146	0.13062
ZC15	0.11727	-0.01813	0.49517
ZC20	0.21445	-0.02991	0.65169
ZC25	0.19891	-0.01238	0.1051

Previously, it is widely reported that due to varying interaction between catalyst and pollutant in different medium, dye solution pH plays a significant role in photodegradation reaction in the presence of effective green nanocatalysts (Mardikar *et al*., 2020). In this study, 35 mg of ZnO/CuO (20%) green NCs catalysts with MB concentration of 10 mg/L were exposed to visible light irradiation, as can be showed in Figures 39a and 39b. The photocatalytic activity was tested at pH 4, 7, and 10 in the presence of 1M NaOH and 1M HCl as pH adjustment.

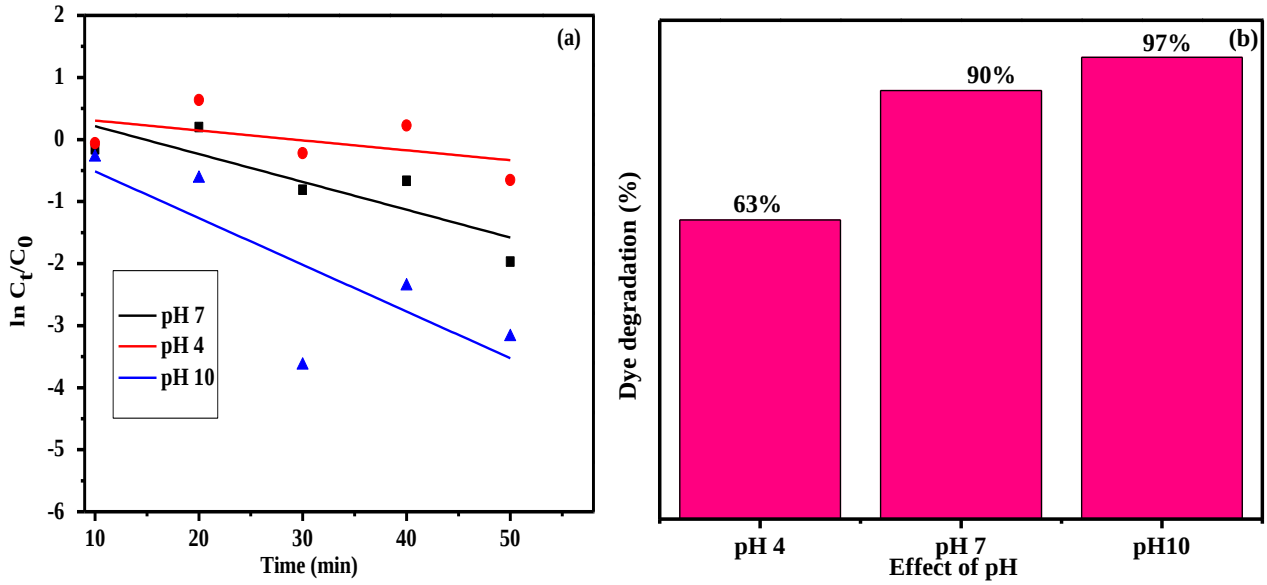

Figure 39: Photodegradation rate kinetics of MB dye at (a) different pH and (b) corresponding degradation efficiency.

Figures 39a and 39b demonstrate that under acidic conditions, the degradation efficiency of MB in the presence of the NCs green catalyst was found to be low. However, as the pH increases to neutral and alkaline values, the degradation ability of the samples gradually increases from 63% to 97% with K value of 0.0161, 0.031 and 0.050/min. This is based on the variation in electrostatic forces existing between MB molecules and catalyst surface at different pH. The surface of the nanocomposites is negatively charged in an alkaline medium and positively charged in acidic medium. Because MB is a cationic dye, its structure becomes positively charged when it is dissolved in water. Unsurprisingly, the degradation rate of MB is therefore higher in alkaline media due to an increase in opposite-charge interactions between the solution and the surface of the green nanocomposites catalyst.

The influence of the photocatalyst dosage on the degradation of MB using various ZnO/CuO nanocomposite catalysts was studied by adjusting the amount of photo catalyst as 10 mg, 25mg, 35 mg and 50 mg under neutral conditions with an initial MB concentration of 10 mg/L. The results are displayed in Figure 40a and 40b. As displayed on lnC/Co Figure 40a and dye degradation bar graphs Figure 40b, increasing the photo catalyst dosage from 10 mg to 35 mg resulted in an increase in the reaction rate and degradation efficiency of MB. However, at higher photocatalyst dosage (50 mg), the degradation efficiency tended to decrease. The reason generally advanced for this result is that increasing the amount of photo catalyst increases the available surface area or the number of active sites on the photo catalyst surface, which consequently increases the number of hydroxyl and superoxide radicals (Tolosana-Moranchel *et al*., 2021).

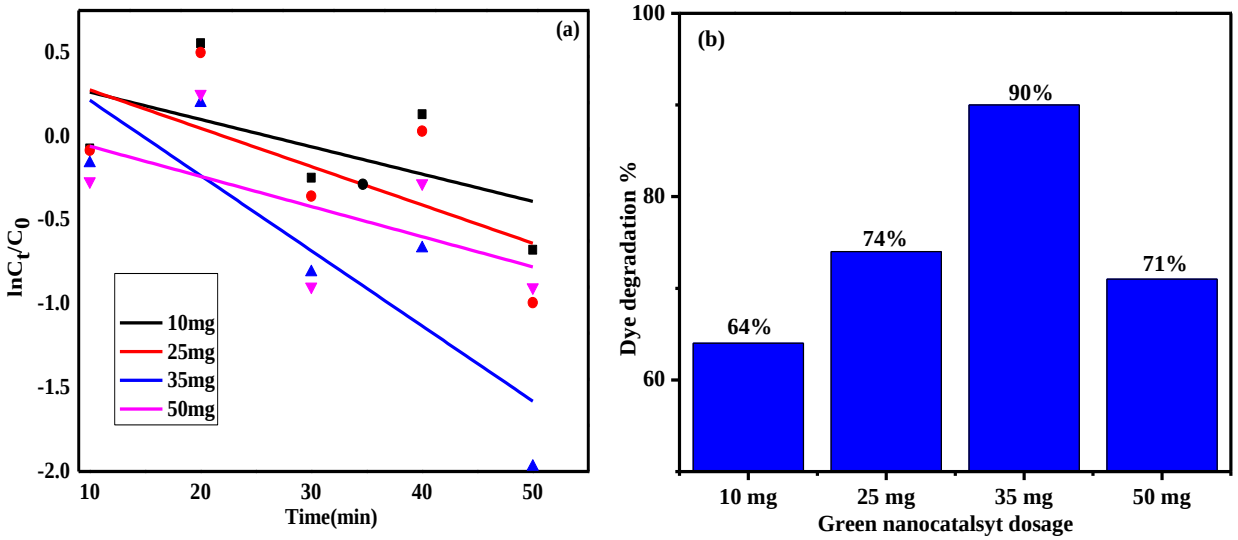

Figure 40: Photodegradation rate kinetics of MB in the presence of ZnO/CuO (20%) catalyst dosages and (b) corresponding degradation efficiency.

Furthermore, as the amount of solid catalyst increases, the transparency of the solution decreases and also the number of active sites decreases due aggregation/agglomeration. The scattering of light in the suspension prevents light from reaching some particles, and thus some of the photocatalyst surface becomes unavailable for light absorption. Therefore, above the optimum amount of catalyst, the degradation efficiency decreases due to the increased opacity of the suspension. The other factor that alters the degradation efficiency of dyes is their initial concentration, depicted in Figure 41b. The effect of initial MB concentration was investigated by using 5 mg/L, 10 mg/L, and 20 mg/L of MB concentration in the presence of 35 mg ZC green formed photocatalyst under neutral condition. The results showed that the degradation efficiency is very high at low concentrations of MB dye and gradually decreases as the dye concentration increases from 5-20 mg.

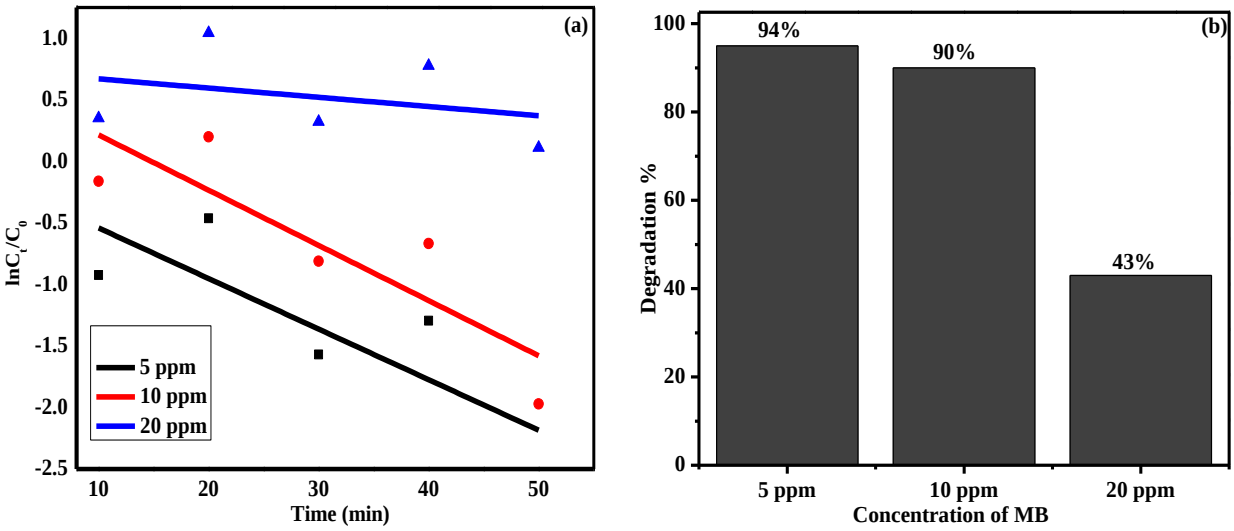

Figure 41: (a) Photodegradation rate kinetics of MB using ZC catalyst with various initial dye concentrations and (b) corresponding degradation efficiency.

Figure 42 displays the possible photocatalytic mechanism of methylene blue in the presence of ZnO/CuO NCs.

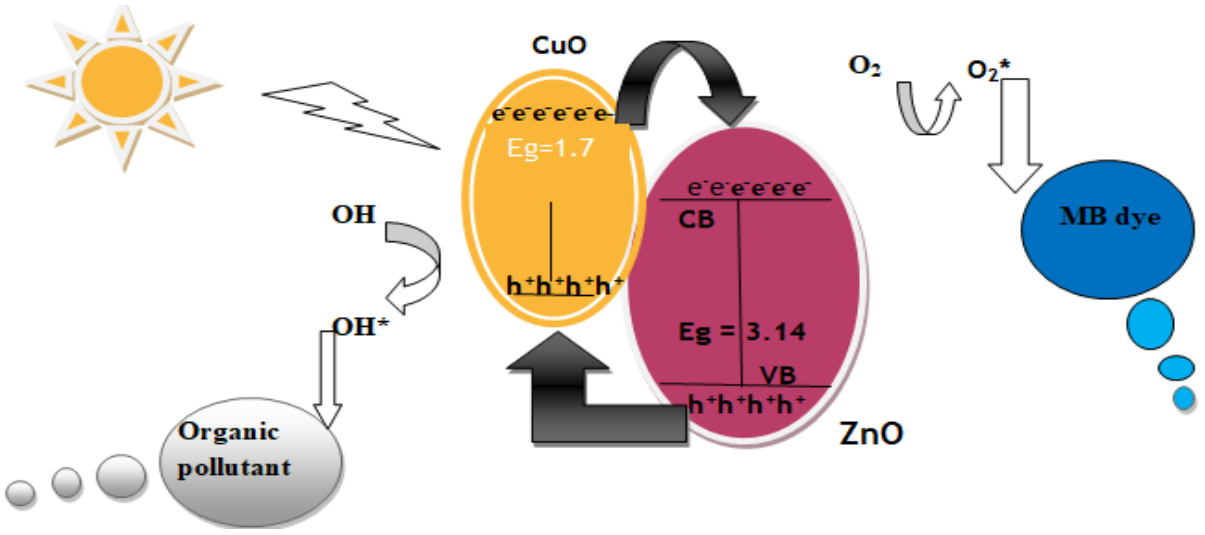

Figure 42: Schematic diagram for photodegradation mechanism of MB dye by ZC green nanocatalysts

Since the rate of degradation is proportional to the number of hydroxyl radicals and superoxide ions (*OH/O^-) formed at the photocatalysts surface, increasing dye molecules could block more active sites available for light absorption and reduce the interaction of light with these sites for *OH generation. Another possible explanation for this result is the effect of light irradiation in the MB dyes. At a high MB dye concentration, a significant amount of light can be absorbed by the dye molecules rather than by the photocatalysts, this results in the decreases in the formation of hydroxyl radicals (*OH) and superoxide ions ($^*O^-$) and in the photocatalytic activity (Khang, 2017).

4.5. Antimicrobial Activity of ZnO/CuO NCs and Co_3O_4 NPs

4.5.1. Antibacterial Activity of ZnO/CuO NCs

The antibacterial activity of the synthesized ZnO (1:1, 1:2, 1:3), CuO, and ZnO/CuO nanomaterials were investigated towards *E.Coli, S. Typhi, B. Subtilis and S.Aureus* at 50, 75, and 100 mg/mL concentration. As can be presented in Figures 42(a-c) and Table 4, the synthesized ZnO NPs formed within 1:1, 1:2, and 1:3 volume ratios showed promised antibacterial activity. The biosynthesized ZnO NPs showed antibacterial effect on all the tested bacterial strains. Moreover, the antibacterial activity of ZnO increased with an increase concentration. In addition to this, the bactericidal effect of green ZnO NPs was found higher for

Gram-positive bacteria than Gram-negative bacteria strains and this difference might was attributed based on the difference in the structural composition of Gram-positive and Gram-negative bacteria (cell membrane is double layered). Among the various volume ratios of ZnO NPs, ZnO (1:3) found to be effective (20 mm zone of inhibition) against *S. Aureus* as compared to the remaining two volume ratios of ZnO NPs. This is due to the fact that the 1:3 volume ratios contains excess amount of MA peel extract compared to 1:1 and 1:2 volume ratios (Samuel *et al*., 2020). This again results in the production of more free radical species (ROS), which cause for the death of more *S.Aureus* cell. Next to the 1:3 volume ratios, 1:2 volume ratios showed 12 mm zone of inhibition against *E.coli* (Saka *et al*. 2022; Droepenu *et al*. 2021).

The antibacterial activity performance of CuO NPs is presented in Figure 42d and Table 4. The antibacterial activity of MA mediated synthesized CuO NPs was checked using *E.coli, S. Typhi, B. Subtilis and S.Aureus* at 50, 75, and 100 mg/mL concentration in the presence of Erythromycin as positive control. The antibacterial activity of green CuO NPs was found higher for Gram-negative bacteria than Gram-positive bacteria and was based on the difference in the structural composition of Gram-positive and Gram-negative bacteria. Green CuO NPs showed more enhanced (21 mm zone of inhibition) activity against *E.coli* strain. As can be supported with the previously reported work, one factor that can alter the antibacterial activity of nanomaterials is the morphological similarity between the bacterial cell and the synthesized drug (Andualem *et al*., 2020). The antibacterial activity of ZnO/CuO (10, 15, 20 and 25 NCs are depicted in Figures 42 (e-h) and Table 4. The formed NCs showed antibacterial performance towards *E.Coli, S. Typhi, B. Subtilis and S.Aureus*.

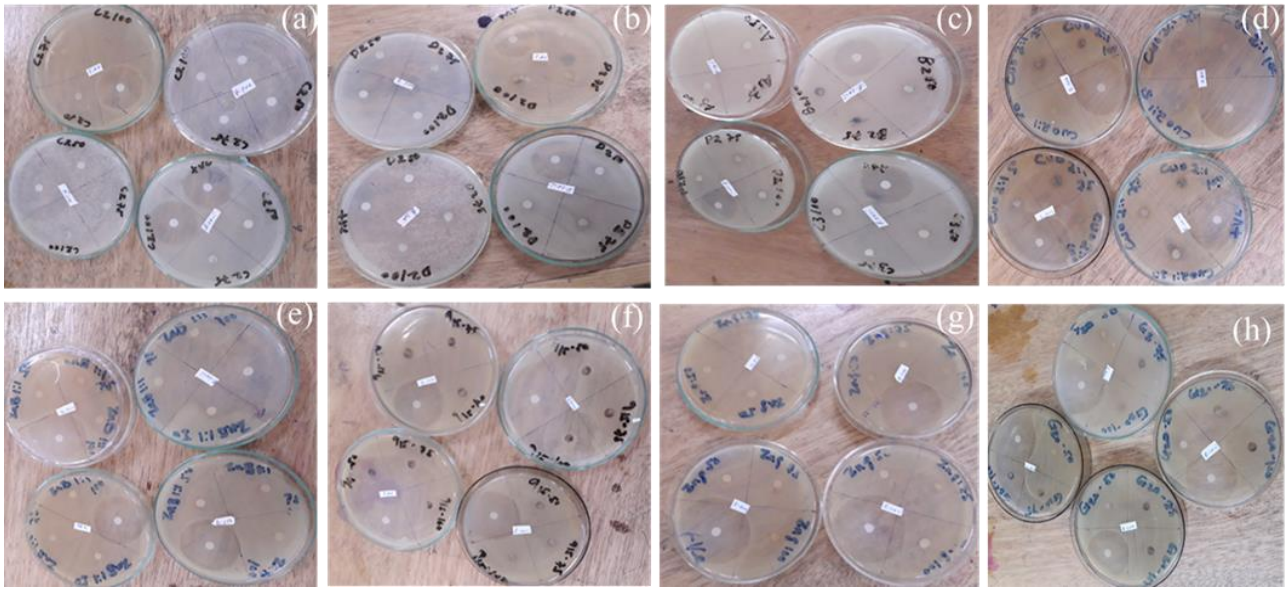

Figure 43*:* Antibacteria activity of green synthesized (a) ZnO (1:1), (b) ZnO (1:2), (c) ZnO (1:3), (d) CuO, (e) ZnO/CuO (10), (f) ZnO/CuO (15), (g) ZnO/CuO (20) and (h) ZnO/CuO (25%).

The result proves that the antibacterial activity of ZnO/CuO NCs dependent on the amount of Cu loaded onto ZnO. Furthermore, the ability of resistance of those pathogenic bacteria in the presence of the ZnO/CuO (20%) nanocomposite was significantly reduced by increasing the CuO content. However, continuous addition of Cu into ZnO leads decreasing the antibacterial performance. This intern significantly indicates that the optimized NCs for the proposed bacteria pathogens are the ZnO/CuO (20%) composition.

Table 4: The antibacterial activity of ZnO NPs, CuO NPs, and ZnO/CuO NCs.

		Zone of inhibition (mm)			
		Gram negative spp.		Gram positive spp.	
NPs	Conc.(mg/mL)	*E.coli*	*S. typhi*	*B. subtilis*	*S.aureus*
ZnO(1:1)	50, 75, and 100	6,6,6	6,8.6	0,7,10	6,6,6
ZnO (1:2)	50, 75, and 100	6,6,12	6,6,6	6,6,11	6,6,10
ZnO (1:3)	50, 75, and 100	6,6,6	6,6,6	6,6,6	6.6,20
CuO	50, 75, and 100	6,6,21	8,6,9	6,6.9	6,6,6
ZnO/CuO (10)	50, 75, and 100	6,6,7	6,6,6	6,6,6	6,6,6
ZnO/CuO (15)	50, 75, and 100	6,6,6	6,6,6	6,6,6	6,6,9
ZnO/CuO(20)	50, 75, and 100	8,10,22	6,8,9	6,6,6	9,7,6
ZnO/CuO(25)	50, 75, and 100	6,6,6	6,6,6	6,6,6	6,6,6
Erythromycin	+ve control	28	28	24	24

On the other hand, resistance ability of those bacteria strains decreased with increasing concentration of the drug, as can be confirmed from Table 4 and Figure 42. The green NCs exhibited less antibacterial activity towards both Gram-negative and Gram-positive strains. This might be contributed due to the fewer amounts of extract used and as well the un-fit of the shape of the pathogens and the NCs (Mohammadi-Aloucheh *et al*., 2018).

In general the antibacterial activity mechanism of green ZnO NPs, CuO NPs and ZnO/CuO NCs might be attributed to the penetration and disintegration of the cell membrane by NPs, which lead to cell lysis. The release of H_2O_2 from the surface of the small sized green synthesized NPs and NCs also reported as the possible mechanism for bactericidal activity. The generation of H_2O_2 is found to highly dependent on the surface area of green ZnO NPs and this intern results in the penetration of cell membrane of the bacteria by the released H_2O_2 and cause damage to kill the bacteria. Furthermore, the presence of various bioactive molecules such saturated and unsaturated alkanes and alkenes, alkaloids, terpenoids, flavonoids, tannins, carbohydrates, sterols, saponins, proteins and amino acids within the peel extract of MA showed potential

bacterial activity against the tested bacteria (Kalia *et al*. 2021; G.K. *et al*. 2015).

4.5.2. Antibacterial Activity of Co_3O_4 NPs

The antibacterial activity of the biogenic synthesized Co_3O_4 NPs using three volume ratios of 1:1, 1:2, and 2:1 has also been tested. It has been found that, as the concentration of Co_3O_4 NPs increased, their antibacterial performance also improved. As can be depicted in Figure 43 supported with Table 5, almost all of the volume ratios of Co_3O_4 NPs showed enhanced antibacterial performance towards *K. pneumonia* strains. This might be due to their structural morphology, which fits with the bacterial cell and this intern enables the nano-drug to kill more bacterial cell wall.

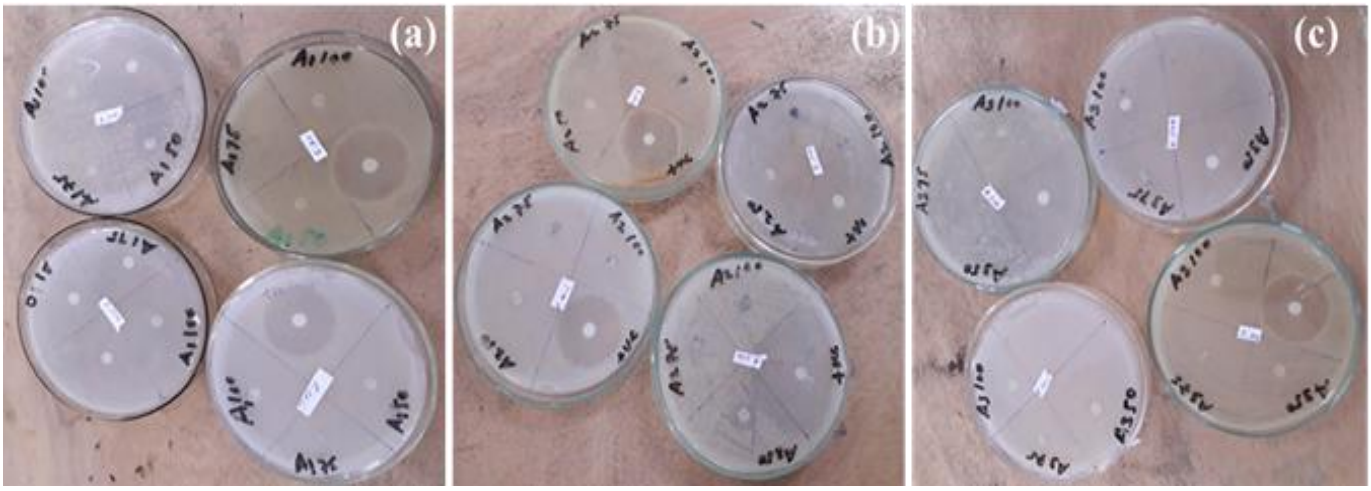

Figure 44: Antibacterial activity of Co_3O_4 NPs biosynthesized in (a) 1:1, (b) 1:2, and (c) 2:1.

Moreover, the antibacterial activity for the three volume ratios was found to be enhanced with an increasing amount of the peel waste extract of the template. The 1:2 volume ratios of Co_3O_4 NPs showed the highest zone of inhibition (27 nm) towards *K. pneumonia*, as compared to the counter parts volume ratios. This might be due to the fact that as the amount of peel extract used during the synthesis process is high, the more reduced oxygen species radicals to be produced. This implies that as the ROS production is high, there is a possibility to react (kill) the bacterial cell; since as literature supports most of the bacteria cell are positively charged and so their reaction with ROS is high (Bekele *et al*. 2022; Adino *et al*. 2021).

Furthermore, Table 5 showed that the 1:1 ratio showed 25 mm zone of inhibition against *K. pneumonia*, next to the 1:2 ratio. The result has been found to fit with the previously published works. Since the 1:1 volume ratio contains high amount of extract as compared to the 2:1 ratios and so it contains high amount of ROS relative to the 2:1 volume ratios (Hafeez *et al*., 2020: Bekele *et al*., 2022).

Figure 45, presents the possible antibacterial mechanism in the presence of Co_3O_4, ZnO, CuO, and ZnO/CuO NCs.

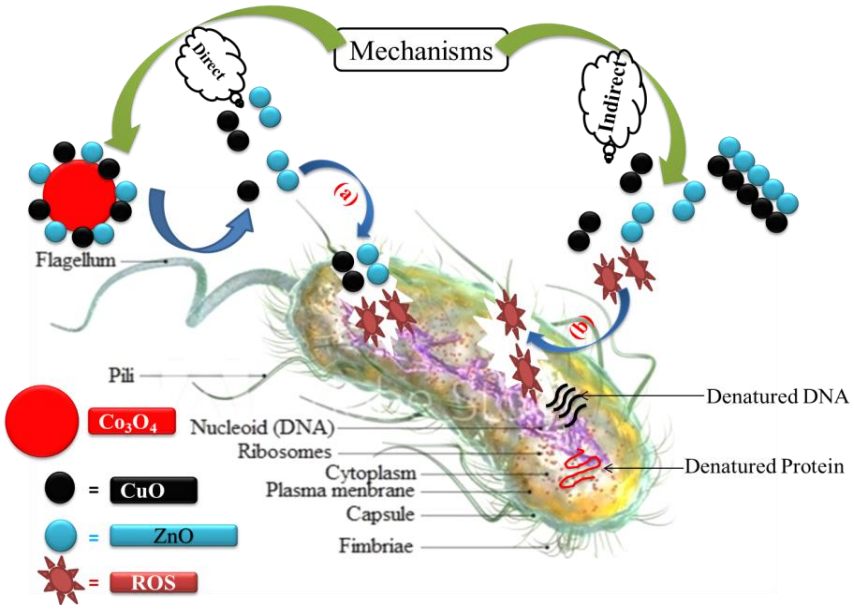

Figure 45: The possible antibacterial activity mechanism in the presence of Co_3O_4, ZnO, CuO and ZnO/CuO NCs.

Table 5: The zone of inhibition of green formed Co_3O_4 NPs against the selected bacteria strains.

		Zone of inhibition (mm)			
		Gram negative spp.		Gram positive spp.	
NPs	Conc.(mg/mL)	*E.coli*	*K. pneumoniae*	*B. subtilis*	*S.Aureus*
Co_3O_4(1:1)	50, 75, and 100	6,6,6	6, 20, 25	7,6,6	6,6,6
Co_3O_4(1:2)	50, 75, and 100	6,6,6	6, 22, 27	7,6,6	6,6,6
Co_3O_4(2:1)	50, 75, and 100	6,12,6	6,16, 24	6,6,6	6,6,6
Erythromycin(+ve) control		28	28	24	24

In general the antibacterial activity of nanoparticles towards both Gram negative and Gram positive strains depends on various factories such as shape/structural geometry relationship between the bacteria and nanoparticles, average crystalline size of the nanoparticles, the concentration of nanoparticles and the nature/strain of bacteria (weather Gram negative/Gram positive) (Thatikayala & Min, 2021).

4.5.3. Antifungal Activity of ZnO/CuO NCs and Co_3O_4 NPs

The peel of MA templated ZnO/CuO NCs was evaluated against *Fusarium oxysporum*, isolated from wilt pepper and *Alternaria Solani*, isolated from tomato fruit. It has been found that the synthesized NCs showed a promised antifungal activity against both *Fusarium oxysporum* and *Alternaria Solani*. Moreover,

the synthesized ZnO and CuO NPs also found to have antifungal activity against the proposed fungal strains. As can be supported in Figures 46a and 46c, those fungal species highly affects pepper and tomato and as a result searching cost effective and environmentally friendly drugs against those fungal species are at a high alarming rate. As proved in Table 6, all of the biotemplated synthesized NPs and NCs showed enhanced antifungal activity. Biotemplated synthesized ZnO NPs showed 2.53 and 1.00 cm mycelia growth of inhibition (MGI) against *Fusarium oxysporum* and *Alternaria Solani* fungal strains, respectively. This directly confirms that the biotemplated synthesized ZnO NPs found to be very effective in preventing and slow down the growth of *Alternaria Solani* of tomato as compared to *Fusarium oxysporum* of pepper (Figure 47a(I) and Figure 48a(I). Bio-formed CuO NPs showed 3.00 and 2.98 cm MGI against *Alternaria Solani* and, *Fusarium oxysporum* (Figure 47a (II) and Figure 48a (II), respectively (Phiwdang et al., 2013). From this, CuO NPs is found to be promised potential candidate and effective in preventing the growth of *Fusarium oxysporum* strains. The variation in the antifungal activity of green ZnO NPs and CuO NPs might be due to the amount of ROS production as well their physico-chemical properties. Similar results related to the present findings were also reported by (Amin *et al*., 2021). Both ZnO NPs and CuO NPs inhibited growth of *Fusarium oxysporum* and *Alternaria Solani* fungal by affecting cellular functions, which results in distortion in fungal hyphae followed by preventing the expansion of conidia and conidiophores and finally leads to cell death. In addition, previous report supports that nutrients' availability within potato dextrose agar plays fundamental role for the capacity of the fungi to recover from the antagonistic effect of nanoparticles (He *et al*., 2011).

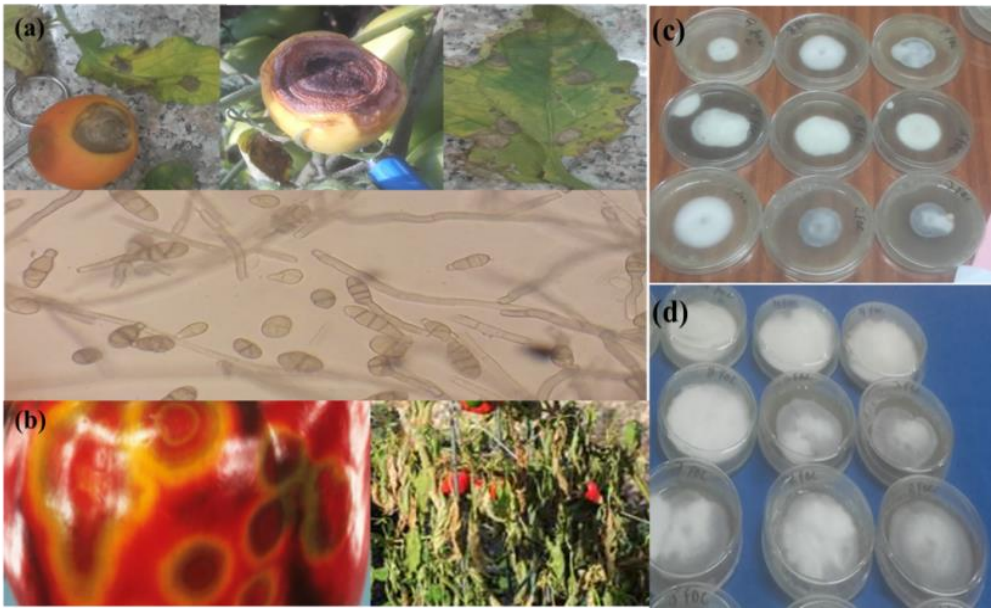

Figure 46*:* (a) Blight symptom on tomato caused by *Alternaria solani*, (b) blight symptom on hot pepper caused by *Fusarium oxysporum*, (c) *Alternaria solani* culture grown on potato dextrose agar and (d) *Fusarium oxysporum* culture grown on potato dextrose agar.

The ZnO/CuO NCs synthesized within 10, 15, and 20% showed enhanced antifungal activity against *Fusarium oxysporum* and *Alternaria solani* of pepper and tomato, respectively. The green synthesized ZnO/CuO (10%) NCs, ZnO/CuO (15%) NCs and ZnO/CuO (20%) NCs showed MGI of 2.53, 3.00, and 1.80 cm against *Fusarium oxysporum* fungi, respectively (Figure 47b).

Table 6: Summery of antifungal activity of ZnO/CuO NCs and Co3O4 NPs.

Fusarium oxysporum (MGI in cm) after 10 days post incubation		*Alternaria Solani* (MGI in cm) after 18 days post incubation	
Treatments	MGI (cm)	Treatments	MGI (cm)
ZnO	2.53	ZnO	1.00
CuO	2.98	CuO	3.00
ZnO/CuO (10%)	2.53	ZnO/CuO (10%)	1.00
ZnO/CuO (15%)	3.00	ZnO/CuO (15%)	1.10
ZnO/CuO (20%)	1.80	ZnO/CuO (20%)	0.40
Co_3O_4 (1:2)	3.15	Co_3O_4 (1:2)	0.00
Co_3O_4 (1:1)	3.00	Co_3O_4 (1:1)	0.00
Co_3O_4 (2:1)	2.98	Co_3O_4 (2:1)	1.40
Mock	3.30	Mock	3.20

Moreover, ZnO/CuO (10%) NCs, ZnO/CuO (15%) NCs and ZnO/CuO (20%) NCs showed a promised MGI of 1.00, 1.10, and 0.40 cm towards *Alternaria solani* of tomato, respectively (Figure 48b). All of the synthesized ZnO/CuO NCs showed enhanced and promised antifungal activity in protecting pepper and tomato fruits. As can be supported with Table 6, the green synthesized ZnO/CuO (20%) NCs showed enhanced antifungal activity as compared to the counterpart NCs. This in turn confirms that, the ZnO/CuO (20%) NCs are the most optimized nanomaterial to the phytopathogenic fungi. This again confirms that the existence of ZnO within the CuO matrix results in enhance the antifungal properties of CuO within the NCs (Sardella et al., 2018). This might be due to the greater and better in charge transfer between CuO and ZnO can enhance the fungi inhibition functionality of CuO. Electron transition within CuO still occurs, but pure ZnO by itself cannot be activated due to its broad E_g (3.37 eV) and exciton binding energy (60 meV), that could be allude of the antifungal activity of the NCs (Mohamed et al., 2021).

In in addition to this, functional groups of nanomaterials also the other factor, which is responsible to initiate the cell membrane damage of the fungal. Figure 47, presents the MGI of synthesized ZnO and CuO NPs in the presence of Mock as a standard, against the growth of *Alternaria solani.*

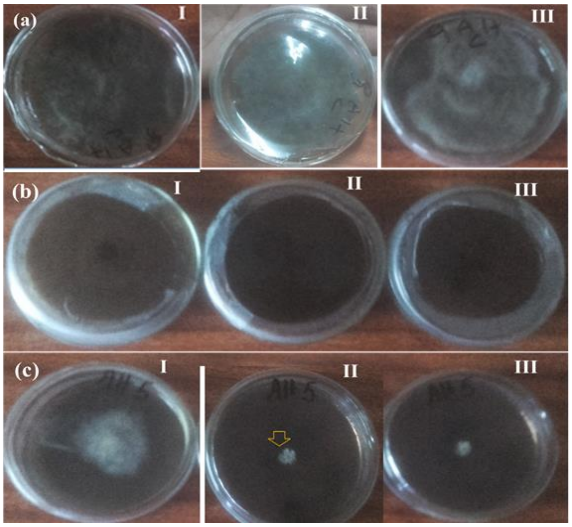

Figure 47: MGI against *Alternaria solani* in the presence of (a) ZnO and CuO NPs and Mock, (b) Co_3O_4 NPs (2:1, 1:1, and 1:2), (c) ZnO/CuO (10%, 15% and 20%). Where I, II, and III in (a) stands for ZnO, CuO, and Mock MGI while I, II, and III in (b) stands for Co_3O_4 NPs synthesized within 2:1, 1:1, and 1:2 volume ratio, respectively and I, II, and IIII in (c) represents ZnO/CuO NPs synthesized within 10, 15, and 20% composition, respectively.

The antifungal activity of ZnO/CuO NCs proves that the growth of *Fusarium oxysporum* of pepper and *Alternaria solani* of tomato were inhibited at a concentration of 10 mg/mL of (Phiwdang *et al*., 2013). Antifungal activity of green synthesized Co_3O_4 NPs also carried out against *Fusarium oxysporum* and *Alternaria Solani* using optimized concentration (10 mg/mL) via the food poisoning method in vitro condition (Figure 47c and 48c).

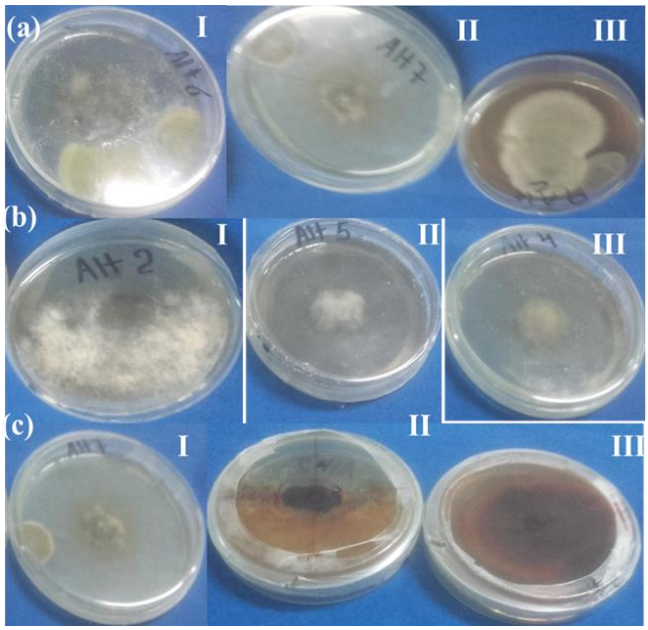

Figure 48: MGI against *Fusarium oxysporum* in the presence of (a) ZnO and CuO NPs and Mock, (b) ZnO/CuO (10, 15, and 20%), and (c) Co_3O_4 (1:2, 1:1, and 2:1) NPs, respectively. Where I, II, and III in (a) stands for ZnO, CuO, and Mock MGI while I, II, and III in (b) stands for Co_3O_4 NPs synthesized within 1:2:1, 1:1, and 2:1 volume ratio, respectively and I, II, and IIII in (c) represents ZnO/CuO NPs synthesized within 10, 15, and 20% composition, respectively. In Figure 47 and 48 (AltC control; Alt: treatment).

As depicted in Table 6, Co_3O_4 NPs synthesized within volume ratio of 1:2, 1:1, and 2:1 NPs showed highly enhanced activity in preventing the growth of *Fusarium oxysporum* of pepper with MGI of 3.15, 3.00, and 2.98 cm, respectively. Of the various cobalt oxide NPs, Co_3O_4 (2:1) NPs possessed enhanced activity in preventing the growth of *Fusarium oxysporum*, compared to the counterpart volume ratios. This might be contributed due to its relatively homogenized morphology, as can be confirmed from its SEM-TEM analysis. Moreover, the enhanced antifungal activity of Co_3O_4 (2:1) NPs might be achieved due to its enhanced optical properties as compared to the counter parts. Since as the optical property is improved, oxidation of nanoparticles also enhanced; this in turn oxidation of nanoparticles occurs due to electromagnetic attractions between the fungal cell membrane and NPs and ended in preventing of fungal growth and killing the cell (Anuradha and Raji 2021). Furthermore, the growth of *Alternaria solani* of tomato after 18 day of post-incubation were checked and its growth were evaluated by the biotemplated synthesized Co_3O_4 (1:2, 1:1, and 2:1) NPs. The measured MGI value proved that Co_3O_4 NPs synthesized within a volume ratio of 1:2, 1:1, and 2:1 showed 0.00, 0.00, and 1.40 cm, respectively. Comparatively, Co_3O_4 NPs has been found the most promised nano-drug in preventing the growth of *Alternaria solani* strain, which affects tomato productivity. Specifically, the 1:2 and 1:1 volume ratio prevent the growth of *Alternaria solani* 100%. So, instead of using commercially and too costy antifungal drugs, the present

findings proves a promised way in the fabrication of green nano-drug materials followed by scaling-up and directly applying to the various agricultural products. As compared to the previous works reported by (Waris *et al*. 2021), the present study has been found to show enhanced activity towards the pathogenic species.

5. Conclusions and Recommendations

5.1. Conclusions

In the present findings, TiO_2/rGO NCs were synthesized within various compositions in the presence of peel waste extract of *Citrus sinensis* and *Musa acuminata*. In addition, ZnO/CuO NCs were also synthesized using peel waste extract of *Musa acuminata*. Moreover, Co_3O_4 NPs were also effectively synthesized within various volume ratios using extract of *Solanum tuberosum* peel extract. The synthesized NPs and NCs were followed by characterization using TGA/DTA, XRD, SEM, EDS, TEM, HRTEM, SAED, UV-DRS and FTIR techniques. The synthesized TiO_2/rGO and ZnO/CuO NCs were used as a green alternative green catalyst for the degradation of methylene blue dye in the presence of visible light irradiation as a source. Furthermore, the synthesized ZnO/CuO NCs and Co_3O_4 NPs were investigated as antibacterial and antifungal agent.

TGA/DTA analysis confirms as TiO_2 NPs were found to be stable above 550℃ having average crystalline size in the range of 7-27nm and 13-22nm for the CS and MA, respectively. The band gap energy was calculated to be in the range of 3.17-3.29 eV and 3.10-3.38 eV for the CS and MA mediated synthesized TiO_2 NPs, respectively. The average crystalline sizes of TiO_2/rGO NCs were found to be in the range of 7-15and 11-12nm for CS and MA, respectively. While Eg of TiO_2/rGO NCs were found in the range of 2.85-3.11 eV and 3.07-3.11 eV for the CS and MA, respectively. SEM analysis proved that TiO_2 NPs and TiO_2/rGO NCs were spherical in shape. TEM, HRTEM, and SAED confirmed that NPs and NCs nanocatalysts were spherical and crystalline. ZnO NPs, CuO NPs, and ZnO/CuO NCs were found to be stable above 450℃. The average crystalline size of ZnO NPs were found to be 25, 28, and 28nm for 1:1, 1:2, and 1:3 volume ratios, respectively and 17.0 nm for CuO NPs. The average crystalline sizes of ZnO/CuO NCs were 23, 23, 23 and 23 nm for 10%, 15%, 20% and 25%, respectively. SEM and TEM part analysis confirms that ZnO, CuO, and ZnO/CuO NCs were found to be spherical shape. E_g of ZnO NPs were calculated as 3.24, 3.25 and 3.24 eV for the 1:1, 1:2, and 1:3, respectively. E_g of CuO NPs were estimated as 1.7 eV and while for ZnO/CuO NCs decreased from 3.24-3.05eV. FTIR study confirms presence of amines, carboxylic acids, alcohols, phenols, proteins, flavonoids and enzymes. It was observed that Co_3O_4 NPs were stable above 400℃, and were spherical in shape, and had the average crystalline size of 18.8, 13.5, 19.45) nm, and band gap energy of 3.25, 3.33, and 3.37 eV for the 1:2, 1:1 and 2:1volume ratios, respectively. SEM-EDS, TEM, HRTEM and SAED confirm that the NPs were spherical in shape

and too crystalline. 94.28%, 94.25%, and 90% of MB degradation were achieved in the presence of TiO_2/rGO-1.5c, TiO_2/rGO-1.5m, and ZnO/CuO NCs catalysts, respectively. The antibacterial activities were found to be increased with increasing concentration of the nano-drug. The antibacterial activity of the synthesized ZnO/CuO (20%) NCs showed 22 mm zone of inhibition and found to be very effective as compared to the counterpart ratios. Moreover, synthesized Co_3O_4 (1:2) NPs were effective towards *K. pneumoniae* strain. ZnO NPs showed 2.53 and 1.00 cm MGI against *Fusarium oxysporum* and *Alternaria solani*, respectively. While CuO NPs showed 2.98 and 3.00 cm MGI *Fusarium oxysporum* and *Alternaria solani*, respectively. Co_3O_4 (2:1) NPs showed 2.98 MGI against *Fusarium oxysporum*. While Co_3O_4 (1:2 and 1:1) NPs showed 0.00 cm MGI against *Alternaria solani*. ZnO/CuO (20%) NCs showed 1.80 cm and 0.40 cm MGI against *Fusarium oxysporum* and *Alternaria solani*, respectively.

5.2. Recommendations

The present findings provides a promising approach for the development, design and scaling up of various nano-based materials, which can play a great role in environmental remediation and as well for the treatment of nano-based bioacid drugs. Moreover, as can be confirmed from the present study, the efficiency of nanomaterials as cost effective environmental remediation to eradicate any pollutants of water, numerous factors should be considered. So, the following possible suggestions should be considered. To be effective in wastewater removal, instead of binary nano-composites, developing of ternary core-shell, doped and nanocomposites could improve the surface area and so the number of active sites of the catalyst. This inter could enhance the degradation efficiency. Furthermore, the various factors such as effect of concentration, synthesis temperature, calcination temperature, pH, concentration of the crude and related parameters should be considered. In addition to this, to improve the biomedical applications of nanomaterials, synthesis affecting factors should be under taken. In order to write the exact reaction mechanism between the extract and precursor salt, the natural products of the extract should be purified followed by NMR characterization. Finally, in order to carry out a comparative study, experimentally and computationally method should be applied for environmental remediation as well as antimicrobial activity.

References

Abass, A. A., Abdulridha, W. A. M., Alaarage, W. K., Abdulrudha, N. H., & Haider, J. (2021). Evaluating the antibacterial effect of cobalt nanoparticles against multi-drug resistant pathogens. Journal of Medicine and Life, 14(6), 823–833. https://doi.org/10.25122/jml-2021-0270

Abebe, B., & Murthy, H. C. A. (2022). Insights into ZnO-based doped porous nanocrystal frameworks. RSC Advances, 12(10), 5816–5833. https://doi.org/10.1039/d1ra09152b

Abraham, N., Rufus, A., Unni, C., & Philip, D. (2018). Dye sensitized solar cells using catalytically active CuO-ZnO nanocomposite synthesized by single step method. Spectrochimica Acta - Part A: Molecular and Biomolecular Spectroscopy, 200(2017), 116–126. https://doi.org/10.1016/j.saa.2018.04.015

Adino, A. T., Edosa, G. D., Gonfa, B. A., Bekele, E. T., & Sabir, F. K. (2021). Synthesis of Cobalt Oxide Nanoparticles Through Chemical and Biological Pathways for Antibacterial Activity. Journal of Nanostructures, 11(3), 577–587. https://doi.org/10.22052/JNS.2021.03.015

Ahamed, M., Alhadlaq, H. A., Khan, M. A. M., Karuppiah, P., & Al-Dhabi, N. A. (2014). Synthesis, characterization, and antimicrobial activity of copper oxide nanoparticles. Journal of Nanomaterials, 2014(Mic). https://doi.org/10.1155/2014/637858

Ait Ahmed, N., Hammache, H., Eyraud, M., Chassigneux, C., Vacandio, F., Knauth, P., Makhloufi, L., & Gabouze, N. eddine. (2019). Voltammetric determination of ascorbic acid with zinc oxide modified glassy carbon electrode. Journal of the Iranian Chemical Society, 16(9), 1957–1963. https://doi.org/10.1007/s13738-019-01668-5

Ajayan, A. S., & Hebsur, N. S. (2021). Green Synthesis of Zinc Oxide Nanoparticles Using Tea (Camellia Sinesis) and Datura (Datura Stramonium) Leaf Extract and Their Characterization. 10(38), 150–157.

Aldalbahi, A., Alterary, S., Ali Abdullrahman Almoghim, R., Awad, M. A., Aldosari, N. S., Fahad Alghannam, S., Nasser Alabdan, A., Alharbi, S., Ali Mohammed Alateeq, B., Abdulrahman Al Mohsen, A., Alkathiri, M. A., & Abdulrahman Alrashed, R. (2020). Greener Synthesis of Zinc Oxide Nanoparticles: Characterization and Multifaceted Applications. Molecules, 25(18), 1–14. https://doi.org/10.3390/molecules25184198

Ali, M. H. H., Al-Afify, A. D., & Goher, M. E. (2018). Preparation and characterization of graphene – TiO2 nanocomposite for enhanced photodegradation of Rhodamine-B dye. Egyptian Journal of Aquatic Research, 44(4), 263–270. https://doi.org/10.1016/j.ejar.2018.11.009

AlShammari, A. S., Halim, M. M., Yam, F. K., & Kaus, N. H. M. (2020). Synthesis of Titanium Dioxide (TiO2)/Reduced Graphene Oxide (rGO) thin film composite by spray pyrolysis technique and its physical properties. Materials Science in Semiconductor Processing, 116(December 2019), 105140. https://doi.org/10.1016/j.mssp.2020.105140

Amin, F., Fozia, Khattak, B., Alotaibi, A., Qasim, M., Ahmad, I., Ullah, R., Bourhia, M., Gul, A., Zahoor, S., & Ahmad, R. (2021). Green Synthesis of Copper Oxide Nanoparticles Using Aerva javanica Leaf Extract and Their Characterization and Investigation of in Vitro Antimicrobial Potential and Cytotoxic Activities. Evidence-Based Complementary and Alternative Medicine, 2021(Mic). https://doi.org/10.1155/2021/5589703

Amir Faiz, M. S., Che Azurahanim, C. A., Yazid, Y., Suriani, A. B., & Siti Nurul Ain, M. J. (2020). Preparation and characterization of graphene oxide from tea waste and it's photocatalytic application of TiO2/graphene nanocomposite. Materials Research Express, 7(1). https://doi.org/10.1088/2053-1591/ab689d

Ananda Murthy, H. C., Zeleke, T. D., Tan, K. B., Ghotekar, S., Alam, M. W., Balachandran, R., Chan, K. Y., Sanaulla, P. F., Anil Kumar, M. R., & Ravikumar, C. R. (2021). Enhanced multifunctionality of CuO nanoparticles synthesized using aqueous leaf extract of Vernonia amygdalina plant. Results in Chemistry, 3(May), 100141. https://doi.org/10.1016/j.rechem.2021.100141

Andualem, W. W., Sabir, F. K., Mohammed, E. T., Belay, H. H., & Gonfa, B. A. (2020). Synthesis of copper oxide nanoparticles using plant leaf extract of catha edulis and its antibacterial activity. Journal of Nanotechnology, 2020. https://doi.org/10.1155/2020/2932434

Anuradha, C. T., & Raji, P. (2021). Citrus limon fruit juice-assisted biomimetic synthesis, characterization and antimicrobial activity of cobalt oxide (Co3O4) nanoparticles. Applied Physics A: Materials Science and Processing, 127(1), 1–9. https://doi.org/10.1007/s00339-020-04209-7

Asamoah, R. B., Annan, E., Mensah, B., Nbelayim, P., Apalangya, V., Onwona-Agyeman, B., & Yaya, A. (2020). A Comparative Study of Antibacterial Activity of CuO/Ag and ZnO/Ag Nanocomposites. Advances in Materials Science and Engineering, 2020. https://doi.org/10.1155/2020/7814324

Asemani, M., & Anarjan, N. (2019). Green synthesis of copper oxide nanoparticles using Juglans regia leaf extract and assessment of their physico-chemical and biological properties. Green Processing and Synthesis, 8(1), 557–567. https://doi.org/10.1515/gps-2019-0025

Azeez, F., Al-Hetlani, E., Arafa, M., Abdelmonem, Y., Nazeer, A. A., Amin, M. O., & Madkour, M. (2018). The effect of surface charge on photocatalytic degradation of methylene blue dye using chargeable titania nanoparticles. Scientific Reports, 8(1), 1–9. https://doi.org/10.1038/s41598-018-25673-5

Bayrami, A., Parvinroo, S., Habibi-Yangjeh, A., & Rahim Pouran, S. (2018). Bio-extract-mediated ZnO nanoparticles: microwave-assisted synthesis, characterization and antidiabetic activity evaluation. Artificial Cells, Nanomedicine and Biotechnology, 46(4), 730–739. https://doi.org/10.1080/21691401.2017.1337025

Bekele, E. T., Gonfa, B. A., Zelekew, O. A., Belay, H. H., & Sabir, F. K. (2020). Synthesis of Titanium Oxide Nanoparticles Using Root Extract of Kniphofia foliosa as a Template, Characterization, and Its Application on Drug Resistance Bacteria. Journal of Nanomaterials, 2020, 1–10. https://doi.org/10.1155/2020/2817037

Bekele, E. T., Murthy, H. C. A., Muniswamy, D., Lemenh, Y. A., Shume, M. S., Tadesse Ayanie, G., Kumar, A. P., Ravikumar, C. R., Balachandran, R., & Roy, A. (2022). Solanum tuberosum Leaf Extract Templated Synthesis of Co3O4 Nanoparticles for Electrochemical Sensor and Antibacterial Applications. Bioinorganic Chemistry and Applications, 2022(16 mm), 1–15. https://doi.org/10.1155/2022/8440756

Bekele, E. T., Zereffa, E. A., Gultom, N. S., Kuo, D. H., Gonfa, B. A., & Sabir, F. K. (2021). Biotemplated Synthesis of Titanium Oxide Nanoparticles in the Presence of Root Extract of Kniphofia schemperi and Its Application for Dye Sensitized Solar Cells. International Journal of Photoenergy, 2021, 1–12. https://doi.org/10.1155/2021/6648325

Bloom, D. E., & Cadarette, D. (2019). Infectious disease threats in the twenty-first century: Strengthening the global response. Frontiers in Immunology, 10(MAR). https://doi.org/10.3389/fimmu.2019.00549

Cahino, A. M., Loureiro, R. G., Dantas, J., Madeira, V. S., & Ribeiro Fernandes, P. C. (2019). Characterization and evaluation of ZnO/CuO catalyst in the degradation of methylene blue using solar radiation. Ceramics International, 45(11), 13628–13636. https://doi.org/10.1016/j.ceramint.2019.03.239

Cao, Y. C., Fu, Z., Wei, W., Zou, L., Mi, T., He, D., Yan, C., Liu, X., Zhu, Y., Chen, L., & Sun, Y. (2015). Reduced graphene oxide supported titanium dioxide nanomaterials for the photocatalysis with long cycling life. Applied Surface Science, 355, 1289–1294. https://doi.org/10.1016/j.apsusc.2015.08.036

Cao, Y., Dhahad, H. A., El-Shorbagy, M. A., Alijani, H. Q., Zakeri, M., Heydari, A., Bahonar, E., Slouf, M., Khatami, M., Naderifar, M., Iravani, S., Khatami, S., & Dehkordi, F. F. (2021). Green synthesis of bimetallic ZnO–CuO nanoparticles and their cytotoxicity properties. Scientific Reports, 11(1), 1–8. https://doi.org/10.1038/s41598-021-02937-1

Chen, Q., Tan, X., Liu, Y., Liu, S., Li, M., Gu, Y., Zhang, P., Ye, S., Yang, Z., & Yang, Y. (2020). Biomass-derived porous graphitic carbon materials for energy and environmental applications. Journal of Materials Chemistry A, 8(12), 5773–5811. https://doi.org/10.1039/c9ta11618d

Chong, S. W., Lai, C. W., & Abdul Hamid, S. B. (2015). Green preparation of reduced graphene oxide using a natural reducing agent. Ceramics International, 41(8), 9505–9513. https://doi.org/10.1016/j.ceramint.2015.04.008

Dananjaya, S. H. S., Kumar, R. S., Yang, M., Nikapitiya, C., Lee, J., & De Zoysa, M. (2018). Synthesis,

characterization of ZnO-chitosan nanocomposites and evaluation of its antifungal activity against pathogenic Candida albicans. International Journal of Biological Macromolecules, 108, 1281–1288. https://doi.org/10.1016/j.ijbiomac.2017.11.046

Demissie, M. G., Sabir, F. K., Edossa, G. D., & Gonfa, B. A. (2020). Synthesis of Zinc Oxide Nanoparticles Using Leaf Extract of Lippia adoensis (Koseret) and Evaluation of Its Antibacterial Activity. Journal of Chemistry, 2020. https://doi.org/10.1155/2020/7459042

Dewi, N. O. M., Yulizar, Y., & Bagus Apriandanu, D. O. (2019). Green synthesis of Co3O4 nanoparticles using Euphorbia heterophylla L. leaves extract: Characterization and photocatalytic activity. IOP Conference Series: Materials Science and Engineering, 509(1). https://doi.org/10.1088/1757-899X/509/1/012105

Droepenu, E. K., Asare, E. A., Wee, B. S., Wahi, R. B., Ayertey, F., & Kyene, M. O. (2021). Biosynthesis, characterization, and antibacterial activity of ZnO nanoaggregates using aqueous extract from Anacardium occidentale leaf: comparative study of different precursors. Beni-Suef University Journal of Basic and Applied Sciences, 10(1), 1–10. https://doi.org/10.1186/s43088-020-00091-7

Elumalai, K., & Velmurugan, S. (2015). Green synthesis, characterization and antimicrobial activities of zinc oxide nanoparticles from the leaf extract of Azadirachta indica (L.). Applied Surface Science, 345, 329–336. https://doi.org/10.1016/j.apsusc.2015.03.176

Ertaş, A., Gören, A. C., Haşimi, N., Tolan, V., & Kolak, U. (2015). Evaluation of antioxidant, cholinesterase inhibitory and antimicrobial properties of Mentha longifolia subsp. noeana and Its secondary metabolites. Records of Natural Products, 9(1), 105–115.

Fagier, M. A. (2021). Plant-Mediated Biosynthesis and Photocatalysis Activities of Zinc Oxide Nanoparticles: A Prospect towards Dyes Mineralization. Journal of Nanotechnology, 2021. https://doi.org/10.1155/2021/6629180

Fan, Y., & Fang, C. (2020). A comprehensive insight into water pollution and driving forces in Western China—case study of Qinghai. Journal of Cleaner Production, 274, 123950. https://doi.org/10.1016/j.jclepro.2020.123950

Farooq, U., Ahmed, F., Pervez, S. A., Rehman, S., Pope, M. A., Fichtner, M., & Roberts, E. P. L. (2020). A stable TiO2-graphene nanocomposite anode with high rate capability for lithium-ion batteries. RSC Advances, 10(50), 29975–29982. https://doi.org/10.1039/d0ra05300g

Fathima, N. N., Aravindhan, R., Rao, J. R., & Nair, B. U. (2008). Dye house wastewater treatment through advanced oxidation process using Cu-exchanged Y zeolite: A heterogeneous catalytic approach. Chemosphere, 70(6), 1146–1151. https://doi.org/10.1016/j.chemosphere.2007.07.033

Fazil, A. A., Narayanan, S., Begum, M. S., Manikandan, G., & Yuvashree, M. (2021). Green synthesis

strategy for producing doped and undoped ZnO nanoparticles: their photocatalytic studies for industrial dye degradation. Water Science and Technology, 84(10–11), 2958–2967. https://doi.org/10.2166/wst.2021.308

G.K., P., P.A., P., Bora, U., Gadewar, M., B.M., N., S., A., G.M., K., & H.M., S. (2015). In vitro antibacterial and cytotoxicity studies of ZnO nanopowders prepared by combustion assisted facile green synthesis. Karbala International Journal of Modern Science, 1(2), 67–77. https://doi.org/10.1016/j.kijoms.2015.10.007

Gabrekiristos, E. (2020). A Newly Emerging Disease of Papaya in Ethiopia: Black Spot (Asperisporium caricae) Disease and Management Options. Journal of Plant Pathology & Microbiology, 11(2), 1–5. https://doi.org/10.35248/2157-7471.20.11.488

Gawade, V. V., Gavade, N. L., Shinde, H. M., Babar, S. B., Kadam, A. N., & Garadkar, K. M. (2017). Green synthesis of ZnO nanoparticles by using Calotropis procera leaves for the photodegradation of methyl orange. Journal of Materials Science: Materials in Electronics, 28(18), 14033–14039. https://doi.org/10.1007/s10854-017-7254-2

Gnanaprakasam, A., Sivakumar, V. M., & Thirumarimurugan, M. (2015). Influencing Parameters in the Photocatalytic Degradation of Organic Effluent via Nanometal Oxide Catalyst: A Review. Indian Journal of Materials Science, 2015, 1–16. https://doi.org/10.1155/2015/601827

Govindasamy, G. A., Mydin, R. B. S. M. N., Sreekantan, S., & Harun, N. H. (2021). Compositions and antimicrobial properties of binary ZnO–CuO nanocomposites encapsulated calcium and carbon from Calotropis gigantea targeted for skin pathogens. Scientific Reports, 11(1), 1–14. https://doi.org/10.1038/s41598-020-79547-w

Habte, A. T., Ayele, D. W., & Hu, M. (2019). Synthesis and Characterization of Reduced Graphene Oxide (rGO) Started from Graphene Oxide (GO) Using the Tour Method with Different Parameters. Advances in Materials Science and Engineering, 2019(Vc). https://doi.org/10.1155/2019/5058163

Hafeez, M., Shaheen, R., Akram, B., Zain-Ul-Abdin, Haq, S., Mahsud, S., Ali, S., & Khan, R. T. (2020). Green synthesis of cobalt oxide nanoparticles for potential biological applications. Materials Research Express, 7(2). https://doi.org/10.1088/2053-1591/ab70dd

Harish, S., Archana, J., Sabarinathan, M., Navaneethan, M., Nisha, K. D., Ponnusamy, S., Muthamizhchelvan, C., Ikeda, H., Aswal, D. K., & Hayakawa, Y. (2017). Controlled structural and compositional characteristic of visible light active ZnO/CuO photocatalyst for the degradation of organic pollutant. Applied Surface Science, 418, 103–112. https://doi.org/10.1016/j.apsusc.2016.12.082

He, L., Liu, Y., Mustapha, A., & Lin, M. (2011). Antifungal activity of zinc oxide nanoparticles against

Botrytis cinerea and Penicillium expansum. Microbiological Research, 166(3), 207–215. https://doi.org/10.1016/j.micres.2010.03.003

Heo, U. S., Kim, D. W., Kim, K. S., & Park, D. W. (2019). A facile synthesis of anatase TiO2-Graphene nanocomposites using plasma and heat treatment. Applied Surface Science, 474, 118–126. https://doi.org/10.1016/j.apsusc.2018.04.083

Huang, X., Cai, H., Zhou, H., Li, T., Jin, H., Evans, C. E., Cai, J., & Pi, J. (2021). Cobalt oxide nanoparticle-synergized protein degradation and phototherapy for enhanced anticancer therapeutics. Acta Biomaterialia, 121, 605–620. https://doi.org/10.1016/j.actbio.2020.11.036

Igwe, O. U., & Ekebo, E. S. (2018). Biofabrication of cobalt Nanoparticle odorata and their potential. Res J Chem, 8(1), 11–17.

Jamdagni, P., Khatri, P., & Rana, J. S. (2018). Green synthesis of zinc oxide nanoparticles using flower extract of Nyctanthes arbor-tristis and their antifungal activity. Journal of King Saud University - Science, 30(2), 168–175. https://doi.org/10.1016/j.jksus.2016.10.002

Jokar, M., Mirghaffari, N., Soleimani, M., & Jabbari, M. (2019). Preparation and characterization of novel bio ion exchanger from medicinal herb waste (chicory) for the removal of Pb2+ and Cd2+ from aqueous solutions. Journal of Water Process Engineering, 28(November 2018), 88–99. https://doi.org/10.1016/j.jwpe.2019.01.007

Joshi, N. C., Congthak, R., & Gururani, P. (2020). Synthesis, adsorptive performances and photo-catalytic activity of graphene oxide/TiO2 (GO/TiO2) nanocomposite-based adsorbent. Nanotechnology for Environmental Engineering, 5(3), 1–13. https://doi.org/10.1007/s41204-020-00085-x

Kalia, A., Kaur, M., Shami, A., Jawandha, S. K., Alghuthaymi, M. A., Thakur, A., & Abd-Elsalam, K. A. (2021). Nettle-leaf extract derived zno/cuo nanoparticle-biopolymer-based antioxidant and antimicrobial nanocomposite packaging films and their impact on extending the post-harvest shelf life of guava fruit. Biomolecules, 11(2), 1–24. https://doi.org/10.3390/biom11020224

Khan, I., Saeed, K., Ali, N., Khan, I., Zhang, B., & Sadiq, M. (2020). Heterogeneous photodegradation of industrial dyes: An insight to different mechanisms and rate affecting parameters. Journal of Environmental Chemical Engineering, 8(5). https://doi.org/10.1016/j.jece.2020.104364

Khan, U., Jan, F. A., Ullah, R., Wajidullah, Ullah, N., & Salman. (2022). Comparative photocatalytic performance and therapeutic applications of zinc oxide (ZnO) and neodymium-doped zinc oxide (Nd–ZnO) nanocatalysts against Acid Yellow-3 dye: kinetic and thermodynamic study of the reaction and effect of various parameters. Journal of Materials Science: Materials in Electronics, 33(5), 2781–2800. https://doi.org/10.1007/s10854-021-07483-0

Khang, N. C. (2017). Further Investigation and Analysis on the Origin of the Optical Properties of Visible

Hetero-photocatalyst TiO2/CuO. Journal of Electronic Materials, 46(10), 5497–5502. https://doi.org/10.1007/s11664-017-5598-2

Khannam, M., Sharma, S., Dolui, S., & Dolui, S. K. (2016). A graphene oxide incorporated TiO2 photoanode for high efficiency quasi solid state dye sensitized solar cells based on a poly-vinyl alcohol gel electrolyte. RSC Advances, 6(60), 55406–55414. https://doi.org/10.1039/c6ra07577k

Kiflom Gebremedhn, Mebrahtu Hagos Kahsay, & Muluken Aklilu. (2019). Green Synthesis of CuO Nanoparticles Using Leaf Extract of Catha edulis and Its Antibacterial Activity. Journal of Pharmacy and Pharmacology, 7(6), 327–342. https://doi.org/10.17265/2328-2150/2019.06.007

Kombaiah, K., Vijaya, J. J., Kennedy, L. J., Kaviyarasu, K., Ramalingam, R. J., & Al-Lohedan, H. A. (2018). Green Synthesis of Co 3 O 4 Nanorods for Highly Efficient Catalytic, Photocatalytic, and Antibacterial Activities . Journal of Nanoscience and Nanotechnology, 19(5), 2590–2598. https://doi.org/10.1166/jnn.2019.15826

Kong, D., Zhao, M., Li, S., Huang, F., Song, J., Yuan, Y., Shen, Y., & Xie, A. (2016). Synthesis of TiO2/rGO Nanocomposites with Enhanced Photoelectrochemical Performance and Photocatalytic Activity. Nano, 11(1), 1–9. https://doi.org/10.1142/S1793292016500077

Kusiak-Nejman, E., & Morawski, A. W. (2019). TiO2/graphene-based nanocomposites for water treatment: A brief overview of charge carrier transfer, antimicrobial and photocatalytic performance. Applied Catalysis B: Environmental, 253, 179–186. https://doi.org/10.1016/j.apcatb.2019.04.055

León, A., Reuquen, P., Garín, C., Segura, R., Vargas, P., Zapata, P., & Orihuela, P. A. (2017). FTIR and raman characterization of TiO2 nanoparticles coated with polyethylene glycol as carrier for 2-methoxyestradiol. Applied Sciences (Switzerland), 7(1), 1–9. https://doi.org/10.3390/app7010049

Li, L., Yu, L., Lin, Z., & Yang, G. (2016). Reduced TiO2-Graphene Oxide Heterostructure As Broad Spectrum-Driven Efficient Water-Splitting Photocatalysts. ACS Applied Materials and Interfaces, 8(13), 8536–8545. https://doi.org/10.1021/acsami.6b00966

Li, W., Yang, X., Fu, H., An, X., & Zhao, H. (2019). Synthesis of TiO 2 -Reduced Graphene Oxide Nanocomposites Offering Highly Enhanced Photocatalytic Activity . Journal of Nanoscience and Nanotechnology, 19(11), 7089–7096. https://doi.org/10.1166/jnn.2019.16624

Li, X., Wang, Q., Zhao, Y., Wu, W., Chen, J., & Meng, H. (2013). Green synthesis and photo-catalytic performances for ZnO-reduced graphene oxide nanocomposites. Journal of Colloid and Interface Science, 411, 69–75. https://doi.org/10.1016/j.jcis.2013.08.050

Luc, W., Fu, X., Shi, J., Lv, J. J., Jouny, M., Ko, B. H., Xu, Y., Tu, Q., Hu, X., Wu, J., Yue, Q., Liu, Y., Jiao, F., & Kang, Y. (2019). Two-dimensional copper nanosheets for electrochemical reduction of carbon monoxide to acetate. Nature Catalysis, 2(5), 423–430. https://doi.org/10.1038/s41929-019-

0269-8

Luo, J., Wu, J., Liu, Z., Li, Z., & Deng, L. (2019). Controlled Synthesis of Porous Co3O4 Nanostructures for Efficient Electrochemical Sensing of Glucose. Journal of Nanomaterials, 2019. https://doi.org/10.1155/2019/8346251

Luque-Morales, P. A., López-Peraza, A., Nava-Olivas, O. J., Amaya-Parra, G., Báez-López, Y. A., Orozco-Carmona, V. M., Garrafa-Gálvez, H. E., & Chinchillas-Chinchillas, M. de J. (2021). Zno semiconductor nanoparticles and their application in photocatalytic degradation of various organic dyes. Materials, 14(24). https://doi.org/10.3390/ma14247537

Lv, Y., Liu, J., Zhang, Z., Zhang, W., Wang, A., Tian, F., Zhao, W., & Yan, J. (2021). Green synthesis of CuO nanoparticles-loaded ZnO nanowires arrays with enhanced photocatalytic activity. Materials Chemistry and Physics, 267(May), 124703. https://doi.org/10.1016/j.matchemphys.2021.124703

Magdalane, C. M., Kaviyarasu, K., Arularasu, M. V., Kanimozhi, K., & Ramalingam, G. (2019). Structural and morphological properties of Co3O4 nanostructures: Investigation of low temperature oxidation for photocatalytic application for waste water treatment. Surfaces and Interfaces, 17(August), 100369. https://doi.org/10.1016/j.surfin.2019.100369

Mahlake, T., Tichapondwa, S. M., Tshuto, T. T., & Chirwa, E. M. N. (2019). The effect of crystalline phase on the simultaneous degradation of phenol and reduction of chromium (VI) using UV/TiO2 photocatalysis. Chemical Engineering Transactions, 76(Vi), 1279–1284. https://doi.org/10.3303/CET1976214

Mardikar, S. P., Kulkarni, S., & Adhyapak, P. V. (2020). Sunlight driven highly efficient degradation of methylene blue by CuO-ZnO nanoflowers. Journal of Environmental Chemical Engineering, 8(2). https://doi.org/10.1016/j.jece.2018.11.033

Meng, X., Geng, D., Liu, J., Li, R., & Sun, X. (2011). Controllable synthesis of graphene-based titanium dioxide nanocomposites by atomic layer deposition. Nanotechnology, 22(16). https://doi.org/10.1088/0957-4484/22/16/165602

Mittal, A. K., Chisti, Y., & Banerjee, U. C. (2013). Synthesis of metallic nanoparticles using plant extracts. Biotechnology Advances, 31(2), 346–356. https://doi.org/10.1016/j.biotechadv.2013.01.003

Mobeen Amanulla, A., & Sundaram, R. (2019). Green synthesis of TiO2 nanoparticles using orange peel extract for antibacterial, cytotoxicity and humidity sensor applications. Materials Today: Proceedings, 8, 323–331. https://doi.org/10.1016/j.matpr.2019.02.118

Mohamed, A. A., Abu-Elghait, M., Ahmed, N. E., & Salem, S. S. (2021). Eco-friendly Mycogenic Synthesis of ZnO and CuO Nanoparticles for In Vitro Antibacterial, Antibiofilm, and Antifungal Applications. Biological Trace Element Research, 199(7), 2788–2799. https://doi.org/10.1007/s12011-

020-02369-4

Mohammadi-Aloucheh, R., Habibi-Yangjeh, A., Bayrami, A., Latifi-Navid, S., & Asadi, A. (2018). Green synthesis of ZnO and ZnO/CuO nanocomposites in Mentha longifolia leaf extract: characterization and their application as anti-bacterial agents. Journal of Materials Science: Materials in Electronics, 29(16), 13596–13605. https://doi.org/10.1007/s10854-018-9487-0

Mohammadi, S. Z., Lashkari, B., & Khosravan, A. (2021). Green synthesis of Co3O4 nanoparticles by using walnut green skin extract as a reducing agent by using response surface methodology. Surfaces and Interfaces, 23(January), 100970. https://doi.org/10.1016/j.surfin.2021.100970

Multiple, T., & Perspectives, P. (2022). Natural Extracts-mediated Biosynthesis of Zinc Oxide Nanoparticles and Their Multiple Pharmacotherapeutic Perspectives. Jordan Journal of Physics, 15(1), 67–79. https://doi.org/10.47011/15.1.10

Muniandy, S. S., Mohd Kaus, N. H., Jiang, Z. T., Altarawneh, M., & Lee, H. L. (2017). Green synthesis of mesoporous anatase TiO2 nanoparticles and their photocatalytic activities. RSC Advances, 7(76), 48083–48094. https://doi.org/10.1039/c7ra08187a

Nainani, R. K., & Thakur, P. (2016). Facile synthesis of TiO2-RGO composite with enhanced performance for the photocatalytic mineralization of organic pollutants. Water Science and Technology, 73(8), 1927–1936. https://doi.org/10.2166/wst.2016.039

Nasrollahzadeh, M., Momeni, S. S., & Sajadi, S. M. (2017). Green synthesis of copper nanoparticles using Plantago asiatica leaf extract and their application for the cyanation of aldehydes using K 4 Fe(CN) 6. Journal of Colloid and Interface Science, 506, 471–477. https://doi.org/10.1016/j.jcis.2017.07.072

Nur, A., Rofi'uddien, J., Basir, M. A., Nazriati, N., & Fajaroh, F. (2018). Synthesis of ZnO/CuO Composite by The Electrochemical Method in The Acetat Acid Solution. Equilibrium Journal of Chemical Engineering, 2(2), 59. https://doi.org/10.20961/equilibrium.v2i2.40436

Okwunodulu, F. U., Chukwuemeka-Okorie, H. O., & Okorie, F. C. (2019). Biological Synthesis of Cobalt Nanoparticles from Mangifera indica Leaf Extract and Application by Detection of Manganese (II) Ions Present in Industrial Wastewater. Chemical Science International Journal, 27(1), 1–8. https://doi.org/10.9734/csji/2019/v27i130106

Pal, S., Mondal, S., Maity, J., & Mukherjee, R. (2018). Synthesis and characterization of zno nanoparticles using Moringa Oleifera leaf extract: Investigation of photocatalytic and antibacterial activity. International Journal of Nanoscience and Nanotechnology, 14(2), 111–119.

Pan, S., Goudoulas, T. B., Jeevanandam, J., Tan, K. X., Chowdhury, S., & Danquah, M. K. (2021). Therapeutic Applications of Metal and Metal-Oxide Nanoparticles: Dermato-Cosmetic Perspectives. Frontiers in Bioengineering and Biotechnology, 9(August), 1–9.

https://doi.org/10.3389/fbioe.2021.724499

Pavan Kumar, M. A., Suresh, D., Nagabhushana, H., & Sharma, S. C. (2015). Beta vulgaris aided green synthesis of ZnO nanoparticles and their luminescence, photocatalytic and antioxidant properties. European Physical Journal Plus, 130(6). https://doi.org/10.1140/epjp/i2015-15109-2

Phiwdang, K., Phensaijai, M., & Pecharapa, W. (2013). Study of antifungal activities of CuO/ZnO nanocomposites synthesized by co-precipitation method. Advanced Materials Research, 802, 89–93. https://doi.org/10.4028/www.scientific.net/AMR.802.89

Prajapati, A. K., & Mondal, M. K. (2021). Novel green strategy for CuO–ZnO–C nanocomposites fabrication using marigold (Tagetes spp.) flower petals extract with and without CTAB treatment for adsorption of Cr(VI) and Congo red dye. Journal of Environmental Management, 290(April), 112615. https://doi.org/10.1016/j.jenvman.2021.112615

Rajith Kumar, C. R., Betageri, V. S., Nagaraju, G., Pujar, G. H., H S, O., & M S, L. (2020). One-pot green synthesis of ZnO-CuO nanocomposite and their enhanced photocatalytic and antibacterial activity. Advances in Natural Sciences: Nanoscience and Nanotechnology, 11(1). https://doi.org/10.1088/2043-6254/ab6c60

Rambabu, K., Bharath, G., Banat, F., & Show, P. L. (2021). Green synthesis of zinc oxide nanoparticles using Phoenix dactylifera waste as bioreductant for effective dye degradation and antibacterial performance in wastewater treatment. Journal of Hazardous Materials, 402(July), 123560. https://doi.org/10.1016/j.jhazmat.2020.123560

Ramos, D. K. C., González, M. V., Muñóz, R. A. E., Cruz, J. S., De Moure-Flores, F. J., & Mayén-Hernández, S. A. (2020). Obtaining and Characterization of TiO2-GO Composites for Photocatalytic Applications. International Journal of Photoenergy, 2020. https://doi.org/10.1155/2020/3489218

Ren, G., Hu, D., Cheng, E. W. C., Vargas-Reus, M. A., Reip, P., & Allaker, R. P. (2009). Characterisation of copper oxide nanoparticles for antimicrobial applications. International Journal of Antimicrobial Agents, 33(6), 587–590. https://doi.org/10.1016/j.ijantimicag.2008.12.004

Ruan, S., Huang, W., Zhao, M., Song, H., & Gao, Z. (2020). A Z-scheme mechanism of the novel ZnO/CuO n-n heterojunction for photocatalytic degradation of Acid Orange 7. Materials Science in Semiconductor Processing, 107(November 2019), 104835. https://doi.org/10.1016/j.mssp.2019.104835

Sabir, S., Zahoor, M. A., Waseem, M., Siddique, M. H., Shafique, M., Imran, M., Hayat, S., Malik, I. R., & Muzammil, S. (2020). Biosynthesis of ZnO Nanoparticles Using Bacillus Subtilis: Characterization and Nutritive Significance for Promoting Plant Growth in Zea mays L. Dose-Response, 18(3), 1–9. https://doi.org/10.1177/1559325820958911

Saka, A., Tesfaye, J. L., Gudata, L., Shanmugam, R., Dwarampudi, L. P., Nagaprasad, N., Krishnaraj, R., & Rajeshkumar, S. (2022). Synthesis, Characterization, and Antibacterial Activity of ZnO Nanoparticles from Fresh Leaf Extracts of Apocynaceae, Carissa spinarum L. (Hagamsa). Journal of Nanomaterials, 2022. https://doi.org/10.1155/2022/6230298

Samuel, M. S., Selvarajan, E., Mathimani, T., Santhanam, N., Phuong, T. N., Brindhadevi, K., & Pugazhendhi, A. (2020). Green synthesis of cobalt-oxide nanoparticle using jumbo Muscadine (Vitis rotundifolia): Characterization and photo-catalytic activity of acid Blue-74. Journal of Photochemistry and Photobiology B: Biology, 211(July), 112011. https://doi.org/10.1016/j.jphotobiol.2020.112011

Saranya, S. K. S. K. S., Padil, V. V. T., Senan, C., Pilankatta, R., Saranya, S. K. K., George, B., Wacławek, S., & Černík, M. (2018). Green synthesis of high temperature stable anatase titanium dioxide nanoparticles using gum kondagogu: Characterization and solar driven photocatalytic degradation of organic dye. Nanomaterials, 8(12). https://doi.org/10.3390/nano8121002

Saravanakkumar, D., Sivaranjani, S., Kaviyarasu, K., Ayeshamariam, A., Ravikumar, B., Pandiarajan, S., Veeralakshmi, C., Jayachandran, M., & Maaza, M. (2018). Synthesis and characterization of ZnO-CuO nanocomposites powder by modified perfume spray pyrolysis method and its antimicrobial investigation. Journal of Semiconductors, 39(3). https://doi.org/10.1088/1674-4926/39/3/033001

Sardella, D., Gatt, R., & Valdramidis, V. P. (2018). Assessing the efficacy of zinc oxide nanoparticles against Penicillium expansum by automated turbidimetric analysis. Mycology, 9(1), 43–48. https://doi.org/10.1080/21501203.2017.1369187

Sathappan, S., Kirubakaran, N., Gunasekaran, D., Gupta, P. K., Verma, R. S., & Sundaram, J. (2021). Green Synthesis of Zinc Oxide Nanoparticles (ZnO NPs) Using Cissus quadrangularis: Characterization, Antimicrobial and Anticancer Studies. Proceedings of the National Academy of Sciences India Section B - Biological Sciences, 91(2), 289–296. https://doi.org/10.1007/s40011-020-01215-w

Sathiyan, K., Bar-Ziv, R., Mendelson, O., & Zidki, T. (2020). Controllable synthesis of TiO2 nanoparticles and their photocatalytic activity in dye degradation. Materials Research Bulletin, 126(February), 110842. https://doi.org/10.1016/j.materresbull.2020.110842

Sawai, J. (2003). Quantitative evaluation of antibacterial activities of metallic oxide powders (ZnO, MgO and CaO) by conductimetric assay. Journal of Microbiological Methods, 54(2), 177–182. https://doi.org/10.1016/S0167-7012(03)00037-X

Seventer, J. M. Van, Health, P., Fook, C., Ng, S., Seposo, X. T., Ling, M., Abdul, M., Ahmad, B., Madaniyazi, L., Sahani, M., Nikolai, L. A., Meyer, C. G., Kremsner, P. G., Velavan, T. P., Fook, C., Ng, S., Seposo, X. T., Ling, M., Abdul, M., … Velavan, T. P. (2020). Since January 2020 Elsevier has

created a COVID-19 resource centre with free information in English and Mandarin on the novel coronavirus COVID- 19 . The COVID-19 resource centre is hosted on Elsevier Connect , the company ' s public news and information . January, 19–21.

Sherly, E. D., Judith Vijaya, J., & John Kennedy, L. (2015). Visible-light-induced photocatalytic performances of ZnO-CuO nanocomposites for degradation of 2,4-dichlorophenol. Cuihua Xuebao/Chinese Journal of Catalysis, 36(8), 1263–1272. https://doi.org/10.1016/S1872-2067(15)60886-5

Shimi, A. K., Ahmed, H. M., Wahab, M., Katheria, S., Wabaidur, S. M., Eldesoky, G. E., Islam, M. A., & Rane, K. P. (2022). Synthesis and Applications of Green Synthesized TiO2Nanoparticles for Photocatalytic Dye Degradation and Antibacterial Activity. Journal of Nanomaterials, 2022. https://doi.org/10.1155/2022/7060388

Shinde, R. S., Khairnar, S. D., Patil, M. R., Adole, V. A., Koli, P. B., Deshmane, V. V., Halwar, D. K., Shinde, R. A., Pawar, T. B., Jagdale, B. S., & Patil, A. V. (2022). Synthesis and Characterization of ZnO/CuO Nanocomposites as an Effective Photocatalyst and Gas Sensor for Environmental Remediation. Journal of Inorganic and Organometallic Polymers and Materials, 32(3), 1045–1066. https://doi.org/10.1007/s10904-021-02178-9

Siddeeg, S. M. (2020). A novel synthesis of TiO2/GO nanocomposite for the uptake of Pb2+ and Cd2+ from wastewater. Materials Research Express, 7(2). https://doi.org/10.1088/2053-1591/ab7407

Singh, J., Dutta, T., Kim, K. H., Rawat, M., Samddar, P., & Kumar, P. (2018). "Green" synthesis of metals and their oxide nanoparticles: Applications for environmental remediation. Journal of Nanobiotechnology, 16(1), 1–24. https://doi.org/10.1186/s12951-018-0408-4

Singh, J., Kumar, S., Alok, A., Upadhyay, S. K., Rawat, M., Tsang, D. C. W., Bolan, N., & Kim, K. H. (2019). The potential of green synthesized zinc oxide nanoparticles as nutrient source for plant growth. Journal of Cleaner Production, 214, 1061–1070. https://doi.org/10.1016/j.jclepro.2019.01.018

Sivachidambaram, M., Vijaya, J. J., Kaviyarasu, K., Kennedy, L. J., Al-Lohedan, H. A., & Jothi Ramalingam, R. (2017a). A novel synthesis protocol for Co3O4 nanocatalysts and their catalytic applications. RSC Advances, 7(62), 38861–38870. https://doi.org/10.1039/c7ra06996k

Sivachidambaram, M., Vijaya, J. J., Kaviyarasu, K., Kennedy, L. J., Al-Lohedan, H. A., & Jothi Ramalingam, R. (2017b). A novel synthesis protocol for Co3O4 nanocatalysts and their catalytic applications. RSC Advances, 7(62), 38861–38870. https://doi.org/10.1039/c7ra06996k

Soni, I., Kumar, P., Sharma, S., & Kudur Jayaprakash, G. (2021). A Short Review on Electrochemical Sensing of Commercial Dyes in Real Samples Using Carbon Paste Electrodes. Electrochem, 2(2), 274–294. https://doi.org/10.3390/electrochem2020020

Štengl, V., Bakardjieva, S., Grygar, T. M., Bludská, J., & Kormunda, M. (2013). TiO2-graphene oxide nanocomposite as advanced photocatalytic materials. Chemistry Central Journal, 7(1), 1–12. https://doi.org/10.1186/1752-153X-7-41

Tadesse, A., Hagos, M., Belachew, N., Murthy, H. C. A., & Basavaiah, K. (2021). Enhanced photocatalytic degradation of Rhodamine B, antibacterial and antioxidant activities of green synthesised ZnO/N doped carbon quantum dot nanocomposites. New Journal of Chemistry, 45(46), 21852–21862. https://doi.org/10.1039/d1nj04036g

Taghavi Fardood, S., Ramazani, A., Moradi, S., & Azimzadeh Asiabi, P. (2017). Green synthesis of zinc oxide nanoparticles using arabic gum and photocatalytic degradation of direct blue 129 dye under visible light. Journal of Materials Science: Materials in Electronics, 28(18), 13596–13601. https://doi.org/10.1007/s10854-017-7199-5

Thatikayala, D., & Min, B. (2021). Ginkgo leaves extract-assisted synthesis of ZnO/CuO nanocrystals for efficient UV-induced photodegradation of organic dyes and antibacterial activity. Journal of Materials Science: Materials in Electronics, 32(13), 17154–17169. https://doi.org/10.1007/s10854-021-06169-x

Tilahun Bekele, E., Gonfa, B. A., & Sabir, F. K. (2021). Use of Different Natural Products to Control Growth of Titanium Oxide Nanoparticles in Green Solvent Emulsion, Characterization, and Their Photocatalytic Application. Bioinorganic Chemistry and Applications, 2021, 1–17. https://doi.org/10.1155/2021/6626313

Tilahun, E., Yilkal, B., Sintayehu, D., Murthy, H. C. A., & Shegaw, M. (2022). Synthesis of ZnO nanoparticles mediated by natural products of Acanthus sennii leaf extract for electrochemical sensing and photocatalytic applications : a comparative study of volume ratios. Chemical Papers, 0123456789. https://doi.org/10.1007/s11696-022-02301-1

Tolosana-Moranchel, A., Pecharromán, C., Faraldos, M., & Bahamonde, A. (2021). Strong effect of light scattering by distribution of TiO2 particle aggregates on photocatalytic efficiency in aqueous suspensions. Chemical Engineering Journal, 403(June 2020). https://doi.org/10.1016/j.cej.2020.126186

Truong, T. T., Pham, T. T., Truong, T. T. T., & Pham, T. D. (2022). Synthesis, characterization of novel ZnO/CuO nanoparticles, and the applications in photocatalytic performance for rhodamine B dye degradation. Environmental Science and Pollution Research, 29(15), 22576–22588. https://doi.org/10.1007/s11356-021-17106-0

Umekar, M. S., Chaudhary, R. G., Bhusari, G. S., Mondal, A., Potbhare, A. K., & Mahmood, S. (2020). Phytoreduced graphene oxide-titanium dioxide nanocomposites using Moringa oleifera stick extract. Materials Today: Proceedings, 29(xxxx), 709–714. https://doi.org/10.1016/j.matpr.2020.04.169

Urabe, A. A., & Aziz, W. J. (2019). Biosynthesis of cobalt oxide (Co3O4) nanoparticles using plant extract of Camellia sinensis (L .) Kuntze and Apium graveolens L . as the antibacterial application. 24(April), 357–365.

Uyen, V. N. L., P. Anh, N., T.T. Van, N., Tri, N., V. Minh, N., N. Huy, N., V. Linh, T., K.P. Ha, H., & Gaspillo, P.-A. (2020). Characteristics and antifungal activity of CuO-ZnO nanocomposites synthesised by the sol-gel technique. Vietnam Journal of Science, Technology and Engineering, 62(1), 17–22. https://doi.org/10.31276/vjste.62(1).17-22

Wang, P., Wang, J., Wang, X., Yu, H., Yu, J., Lei, M., & Wang, Y. (2013). One-step synthesis of easy-recycling TiO2-rGO nanocomposite photocatalysts with enhanced photocatalytic activity. Applied Catalysis B: Environmental, 132–133, 452–459. https://doi.org/10.1016/j.apcatb.2012.12.009

Waris, A., Din, M., Ali, A., Afridi, S., Baset, A., Khan, A. U., & Ali, M. (2021). Green fabrication of Co and Co3O4nanoparticles and their biomedical applications: A review. Open Life Sciences, 16(1), 14–30. https://doi.org/10.1515/biol-2021-0003

Xing, B., Shi, C., Zhang, C., Yi, G., Chen, L., Guo, H., Huang, G., & Cao, J. (2016). Preparation of TiO2/Activated Carbon Composites for Photocatalytic Degradation of RhB under UV Light Irradiation. Journal of Nanomaterials, 2016. https://doi.org/10.1155/2016/8393648

Xu, K., Wu, J., Tan, C. F., Ho, G. W., Wei, A., & Hong, M. (2017). Ag-CuO-ZnO metal-semiconductor multiconcentric nanotubes for achieving superior and perdurable photodegradation. Nanoscale, 9(32), 11574–11583. https://doi.org/10.1039/c7nr03279j

Xu, L., Zhou, Y., Wu, Z., Zheng, G., He, J., & Zhou, Y. (2017). Improved photocatalytic activity of nanocrystalline ZnO by coupling with CuO. Journal of Physics and Chemistry of Solids, 106(February), 29–36. https://doi.org/10.1016/j.jpcs.2017.03.001

Yin, J., Zhan, F., Jiao, T., Wang, W., Zhang, G., Jiao, J., Jiang, G., Zhang, Q., Gu, J., & Peng, Q. (2020). Facile preparation of self-assembled MXene@Au@CdS nanocomposite with enhanced photocatalytic hydrogen production activity. Science China Materials, 63(11), 2228–2238. https://doi.org/10.1007/s40843-020-1299-4

Yu, M., Yu, T., Chen, S., Guo, Z., & Seok, I. (2020). A Facile Synthesis of Ag/TiO_2/rGO Nanocomposites with Enhanced Visible Light Photocatalytic Activity. ES Materials & Manufacturing, 64–69. https://doi.org/10.30919/esmm5f712

Yulizar, Y., Bakri, R., Apriandanu, D. O. B., & Hidayat, T. (2018). ZnO/CuO nanocomposite prepared in one-pot green synthesis using seed bark extract of Theobroma cacao. Nano-Structures and Nano-Objects, 16, 300–305. https://doi.org/10.1016/j.nanoso.2018.09.003

Zelekew, O. A., Aragaw, S. G., Sabir, F. K., Andoshe, D. M., Duma, A. D., Kuo, D. H., Chen, X., Desissa,

T. D., Tesfamariam, B. B., Feyisa, G. B., Abdullah, H., Bekele, E. T., & Aga, F. G. (2021). Green synthesis of Co-doped ZnO via the accumulation of cobalt ion onto Eichhornia crassipes plant tissue and the photocatalytic degradation efficiency under visible light. Materials Research Express, 8(2). https://doi.org/10.1088/2053-1591/abe2d6

Zhang, Y., Tang, Z. R., Fu, X., & Xu, Y. J. (2010). TiO_2-graphene nanocomposites for gas-phase photocatalytic degradation of volatile aromatic pollutant: Is TiO_2-graphene truly different from other TiO2-carbon composite materials? ACS Nano, 4(12), 7303–7314. https://doi.org/10.1021/nn1024219

Zhu, L., Li, H., Liu, Z., Xia, P., Xie, Y., & Xiong, D. (2018). Synthesis of the 0D/3D CuO/ZnO Heterojunction with Enhanced Photocatalytic Activity. Journal of Physical Chemistry C, 122(17), 9531–9539. https://doi.org/10.1021/acs.jpcc.8b01933

Name	Signature	Date
Principal Investigator: Bedasa Abdisa (PhD)	_____	_____
Co- Investigator: Eneyew Tilahun (M.Sc)	_____	_____
Co- Investigator: Fedlu Kedir (PhD)	_____	_____

Approval of Reviewers

I hereby confirm that (PI) **Dr. Bedasa Abdisa** has accomplished his work as per the approved proposal and incorporated all the comments given by the reviewers in his terminal report of the project entitled "**Biomediated synthesis of Nano Metal Oxides and Nanocomposite Metal Oxides for Photocatalytic and Antimicrobial Applications"** and hence the report qualifies for submission as standard research output.

Name	Signature	Date
Reviewer 1. _____	_____	_____
Reviewer 2. _____	_____	_____

Approval: School Ethical Review Board (School Scientific Committee)

Name	Signature	Date
1. _____	_____	_____
2. _____	_____	_____
3. _____	_____	_____
4. _____	_____	_____
5. _____	_____	_____
6. _____	_____	_____